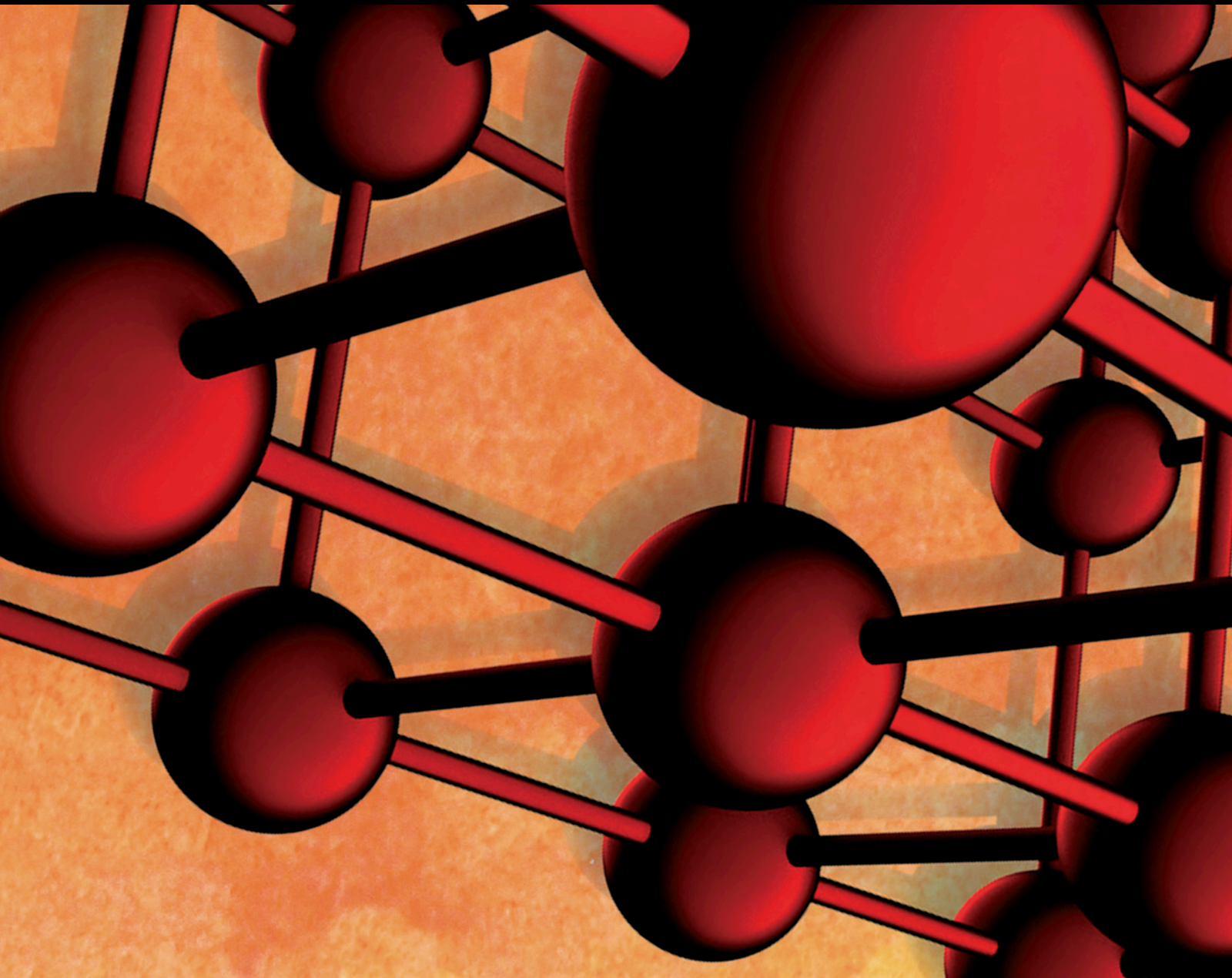


Advances in Materials Science and Engineering

Plastic Deformation, Microstructure, and Residual Stress in Metal Joining for Light Weighting

Lead Guest Editor: Rezwanul Haque

Guest Editors: Ayodele Olofinjana and Benjamin I. Imasogie





**Plastic Deformation, Microstructure, and
Residual Stress in Metal Joining for Light
Weighting**

Advances in Materials Science and Engineering

**Plastic Deformation, Microstructure,
and Residual Stress in Metal Joining for
Light Weighting**

Lead Guest Editor: Rezwanul Haque

Guest Editors: Ayodele Olofinjana and Benjamin I.
Imasogie



Copyright © 2020 Hindawi Limited. All rights reserved.

This is a special issue published in “Advances in Materials Science and Engineering.” All articles are open access articles distributed under the Creative Commons Attribution License, which permits unrestricted use, distribution, and reproduction in any medium, provided the original work is properly cited.

Chief Editor

Amit Bandyopadhyay, USA

Editorial Board

Antonio Abate, Germany
H.P.S Abdul Khalil, Malaysia
Michael Aizenshtein, Israel
Hamed Akhavan, Portugal
Jarir Aktaa, Germany
Amelia Almeida, Portugal
Rajan Ambat, Denmark
Konstantinos G. Anthymidis, Greece
Santiago Aparicio, Spain
Raul Arenal, Spain
Alicia E. Ares, Argentina
Farhad Aslani, Australia
Apostolos Avgeropoulos, Greece
Renal Backov, France
Markus Bambach, Germany
Massimiliano Barletta, Italy
Stefano Bellucci, Italy
Avi Bendavid, Australia
Brahim Benmokrane, Canada
Jamal Berakdar, Germany
Jean-Michel Berghéau, France
Guillaume Bernard-Granger, France
Giovanni Berselli, Italy
Patrice Berthod, France
Michele Bianchi, Italy
Hugo C. Biscaia, Portugal
Antonio Boccaccio, Italy
Susmita Bose, USA
Heinz-Günter Brokmeier, Germany
Steve Bull, United Kingdom
Gianlorenzo Bussetti, Italy
Jose M. Cabrera, Spain
Antonio Caggiano, Germany
Veronica Calado, Brazil
Marco Cannas, Italy
Gianfranco Carotenuto, Italy
Paolo Andrea Carraro, Italy
Victor M. Castaño, Mexico
Michelina Catauro, Italy
Robert Černý, Czech Republic
Jose Cesar de Sa, Portugal
Wensu Chen, Australia
Daolun Chen, Canada
Francisco Chinesta, France

Er-Yuan Chuang, Taiwan
Gianluca Cicala, Italy
Francesco Colangelo, Italy
Marco Consales, Italy
María Criado, Spain
Gabriel Cuello, France
Lucas da Silva, Portugal
Narendra B. Dahotre, USA
J. Paulo Davim, Portugal
Angela De Bonis, Italy
Abílio De Jesus, Portugal
José António Fonseca de Oliveira Correia, Portugal
Luca De Stefano, Italy
Francesco Delogu, Italy
Luigi Di Benedetto, Italy
Aldo Di Carlo, Italy
Maria Laura Di Lorenzo, Italy
Marisa Di Sabatino, Norway
Luigi Di Sarno, Italy
Ana María Díez-Pascual, Spain
Guru P. Dinda, USA
Nadka Tzankova Dintcheva, Italy
Mingdong Dong, Denmark
Hongbiao Dong, China
Frederic Dumur, France
Stanislaw Dymek, Poland
Kaveh Edalati, Japan
Philip Eisenlohr, USA
Claude Estournès, France
Luis Evangelista, Norway
Michele Fedel, Italy
Francisco Javier Fernández Fernández, Spain
Isabel J. Ferrer, Spain
Paolo Ferro, Italy
Dora Foti, Italy
Massimo Fresta, Italy
Pasquale Gallo, Finland
Germà Garcia-Belmonte, Spain
Santiago Garcia-Granda, Spain
Carlos Garcia-Mateo, Spain
Georgios I. Giannopoulos, Greece
Ivan Giorgio, Italy

Antonio Gloria, Italy
Vincenzo Guarino, Italy
Daniel Guay, Canada
Gianluca Gubbiotti, Italy
Jenő Gubicza, Hungary
Xuchun Gui, China
Benoit Guiffard, France
Ivan Gutierrez-Urrutia, Japan
Hiroki Habazaki, Japan
Simo-Pekka Hannula, Finland
Akbar Heidarzadeh, Iran
David Holec, Austria
Satoshi Horikoshi, Japan
David Houivet, France
Rui Huang, USA
Yi Huang, United Kingdom
Michele Iafisco, Italy
Erdin Ibraim, United Kingdom
Saliha Ilican, Turkey
Md Mainul Islam, Australia
Ilia Ivanov, USA
Hom Kandel, USA
kenji Kaneko, Japan
Fuat Kara, Turkey
Katsuyuki Kida, Japan
Akihiko Kimura, Japan
Soshu Kirihara, Japan
Paweł Kłosowski, Poland
Jan Koci, Czech Republic
Ling B. Kong, Singapore
Lingxue Kong, Australia
Fantao Kong, China
Pramod Koshy, Australia
Hongchao Kou, China
Alexander Kromka, Czech Republic
Ravi Keshwar Kumar, India
Luciano Lamberti, Italy
Andrea Lamberti, Italy
Fulvio Lavecchia, Italy
Marino Lavorgna, Italy
Laurent Lebrun, France
Joon-Hyung Lee, Republic of Korea
Pavel Lejcek, Czech Republic
Cristina Leonelli, Italy
Ying Li, USA
Yuanshi Li, Canada
Yuning Li, Canada

Guang-xing Liang, China
Barbara Liguori, Italy
Shaomin Liu, Australia
Yunqi Liu, China
Jun Liu, China
Meilin Liu, Georgia
Zhiping Luo, USA
Fernando Lusquiños, Spain
Peter Majewski, Australia
Georgios Maliaris, Greece
Muhamamd A. Malik, United Kingdom
Dimitrios E. Manolakos, Greece
Necmettin Maraşlı, Turkey
Enzo Martinelli, Italy
Alessandro Martucci, Italy
Yoshitake Masuda, Japan
Bobby Kannan Mathan, Australia
Roshan Mayadunne, Australia
Mamoun Medraj, Canada
Shazim A. Memon, Kazakhstan
Philippe Miele, France
Andrey E. Miroshnichenko, Australia
Hossein Moayedi, Vietnam
Sakar Mohan, India
Jose M. Monzo, Spain
Michele Muccini, Italy
Alfonso Muñoz, Spain
Roger Narayan, USA
Rufino M. Navarro, Spain
Miguel Navarro-Cia, United Kingdom
Ali Nazari, Australia
Behzad Nematollahi, Australia
Luigi Nicolais, Italy
Peter Niemz, Switzerland
Hiroshi Noguchi, Japan
Chérif Nouar, France
Olanrewaju Ojo, Canada
Dariusz Oleszak, Poland
Laurent Orgéas, France
Togay Ozbakkaloglu, United Kingdom
Nezih Pala, USA
Marián Palcut, Slovakia
Davide Palumbo, Italy
Gianfranco Palumbo, Italy
Zbyšek Pavlík, Czech Republic
Matthew Peel, United Kingdom
Alessandro Pegoretti, Italy

Gianluca Percoco, Italy
Claudio Pettinari, Italy
Giorgio Pia, Italy
Silvia M. Pietralunga, Italy
Daniela Pilone, Italy
Teresa M. Piqué, Argentina
Candido Fabrizio Pirri, Italy
Marinos Pitsikalis, Greece
Alain Portavoce, France
Simon C. Potter, Canada
Ulrich Prah, Germany
Viviana F. Rahhal, Argentina
Carlos R. Rambo, Brazil
Shahed Rasekh, Portugal
Manijeh Razeghi, USA
Paulo Reis, Portugal
Yuri Ribakov, Israel
Aniello Riccio, Italy
Anna Richelli, Italy
Antonio Riveiro, Spain
Marco Rossi, Italy
Sylvie Rossignol, France
Pascal Roussel, France
Fernando Rubio-Marcos, Spain
Francesco Ruffino, Italy
Mark H. Rummeli, China
Pietro Russo, Italy
Antti Salminen, Finland
F.H. Samuel, Canada
Maria Gabriella Santonicola, Italy
Hélder A. Santos, Finland
Carlo Santulli, Italy
Fabrizio Sarasini, Italy
Michael J. Schu#tze, Germany
Raffaele Sepe, Italy
Kenichi Shimizu, USA
Fridon Shubitidze, USA
Mercedes Solla, Spain
Donato Sorgente, Italy
Charles C. Sorrell, Australia
Andres Sotelo, Spain
Costas M. Soukoulis, USA
Damien Soulat, France
Adolfo Speghini, Italy
Antonino Squillace, Italy
Koichi Sugimoto, Japan
Baozhong Sun, China

Sam-Shajing Sun, USA
Youhong Tang, Australia
Shengwen Tang, China
Kohji Tashiro, Japan
Miguel Angel Torres, Spain
Laszlo Toth, France
Achim Trampert, Germany
Tomasz Trzepieciński, Poland
Matjaz Valant, Slovenia
Luca Valentini, Italy
Ashkan Vaziri, USA
Lijing Wang, Australia
Zhongchang Wang, Portugal
Rui Wang, China
Lu Wei, China
Jörg M. K. Wiezorek, USA
Jiang Wu, China
Guoqiang Xie, China
Jinyang Xu, China
Dongmin Yang, United Kingdom
Zhonghua Yao, China
Hemmige S. Yathirajan, India
Yee-wen Yen, Taiwan
Wenbin Yi, China
Ling Yin, Australia
Tetsu Yonezawa, Japan
Hiroshi Yoshihara, Japan
Belal F. Yousif, Australia
Lenka Zaji#c#kova#, Czech Republic
Zhigang Zang, China
Michele Zappalorto, Italy
Jinghuai Zhang, China
Li Zhang, China
Gang Zhang, Singapore
Mikhail Zheludkevich, Germany
Wei Zhou, China
You Zhou, Japan
Hongtao Zhu, Australia

Contents

Plastic Deformation, Microstructure, and Residual Stress in Metal Joining for Light Weighting

Rezwanul Haque , Ayodele Olofinjana, and Benjamin Imasogie

Editorial (2 pages), Article ID 1250154, Volume 2020 (2020)

Study on Properties of Cold-Sprayed Al-Zn Coating on S135 Drill Pipe Steel

Dongli Lv , Tao Zhang , and Feiyang Gong

Research Article (10 pages), Article ID 9209465, Volume 2020 (2020)

Analysis of Strength Factors of Steel Cord Conveyor Belt Splices Based on the FEM

Xianguo Li , Xinyu Long, Zhenqian Shen , and Changyun Miao

Research Article (9 pages), Article ID 6926413, Volume 2019 (2019)

Hot Deformation Behavior and Microstructural Evolution of Twin-Roll-Casting Mg Alloy during High-Temperature Compression

Qingshan Yang , Jiahong Dai, Sensen Chai, Daliang Yu, Bin Jiang, and Fusheng Pan

Research Article (7 pages), Article ID 1820671, Volume 2019 (2019)

Brazeability, Microstructure, and Joint Characteristics of ZrO₂/Ti-6Al-4V Brazed by Ag-Cu-Ti Filler Reinforced with Cerium Oxide Nanoparticles

Ashutosh Sharma , and Byungmin Ahn 

Research Article (11 pages), Article ID 8602632, Volume 2019 (2019)

Precision Forming Technology for Crimping of Large Straight Welded Pipes

Li-feng Fan , Pei Liang, Ge Wang, Ying Gao , and Benguo Zhang

Research Article (9 pages), Article ID 1376164, Volume 2019 (2019)

Dynamic Behavior of Self-Piercing Riveted and Mechanical Clinched Joints of Dissimilar Materials: An Experimental Comparative Investigation

Yulong Ge , and Yong Xia 

Research Article (12 pages), Article ID 6463576, Volume 2019 (2019)

Microstructural Characterization and Mechanical Properties of Ti-6Al-4V Alloy Subjected to Dynamic Plastic Deformation Achieved by Multipass Hammer Forging with Different Forging Temperatures

Xiurong Fang , Jiang Wu, Xue Ou, and Fuqiang Yang 

Research Article (12 pages), Article ID 6410238, Volume 2019 (2019)

Editorial

Plastic Deformation, Microstructure, and Residual Stress in Metal Joining for Light Weighting

Rezwanul Haque ¹, Ayodele Olofinjana,¹ and Benjamin Imasogie²

¹University of the Sunshine Coast, Sunshine Coast, Australia

²Obafemi Awolowo University, Ife, Nigeria

Correspondence should be addressed to Rezwanul Haque; rhaque@usc.edu.au

Received 22 April 2020; Accepted 22 April 2020; Published 5 May 2020

Copyright © 2020 Rezwanul Haque et al. This is an open access article distributed under the Creative Commons Attribution License, which permits unrestricted use, distribution, and reproduction in any medium, provided the original work is properly cited.

Manufacturing industries throughout the world are constantly facing the pressure to reduce carbon emissions. The aerospace and automobile industries strategy for reducing carbon emissions is inherently centred around selection of designs and materials aimed at reducing the overall weight. Most common approaches to light-weighting have been based on clever selection of materials that suggests using engineered light alloys: titanium, magnesium, and aluminium and hybrid materials such as fibre-reinforced composites with high strength-to-weight ratios.

Since by design, engineering devices are multicomponent, and combining materials in design to achieve light-weight requires the need to understand how well new and different materials can fit to meet the functional (especially structural) properties. Joining of materials in lightweight designs has, therefore, become a topical issue [1]. There is still a lot of research to be performed to address the challenges that come with methods for joining because of the rapid introduction of new lightweight alloys in designs of components. The issues facing the joining of dissimilar materials, such as ceramics to metals [2], composite to metal [3, 4], two dissimilar metals [5, 6], constantly need to be addressed. Many joining techniques that are fusion-based [1, 7] and mechanical fastenings [3] that have been proposed are promising, but the accompanying severe plastic deformation and the microstructural modifications that typically attend joints for both fusion and mechanical joining processes can potentially cause problems and need to be addressed. Consequently, the mechanical condition of the joint-affected zone needs to be studied well especially the

propensity for the development of residual stresses. A continuous development of innovations is required to achieve the goal of efficient joining methods for newly developed lightweight materials that covers the commonly used candidates: Ti-Al-V [2], Mg-Zn [6], and Al- alloys [7] and fibre-reinforced plastics (FRP) [3, 4].

The objective of this special issue is to collate manuscripts addressing significant developments and innovations in research and overview of technology for joining and combination of dissimilar materials in engineering components to achieve improved performance and lightweight. In this special issue, the published papers addressed several issues relating to light-weighting that included (1) joining of dissimilar materials, (2) microstructure-property relationships in deformation processing, (3) combination of materials to achieve optimum engineering functions, and (4) application of computational methods in manufacturing.

Magnesium (Mg) alloys because of its low specific gravity, are currently attracting attention for light-weighting designs especially in transport machines where the target is to reduce energy consumption. Mg-AZ alloy series [8] were originally designed to be shaped by casting, but as new alloys are being introduced, the need for deformation shaping has increased. Q. Yang et al. studied the deformation behaviour of an Mg alloy during high temperature compression. They reported the effects of processing parameters on the hot forming of Mg AZ31. Their work indicated the importance of flow stress and its relationship with forming temperature. They provided evidence of grain growth that resulted from dynamic recrystallization at 500°C.

Ti-6Al-4V alloys are the prime candidate material in many lightweight designs because of their very high specific stiffness (modulus-to-density ratio). Their microstructures depend so much on processing and structure-processing relationship, which is a topical issue. X. Fang et al. studied the microstructural behaviour of Ti-6Al-4V alloy due to severe plastic deformation. Their study provides insight into the effects of forging temperature on the microstructure of Ti-6Al-4V alloys. It was highlighted that the microstructural homogeneity is enhanced by the dynamic plastic deformation. The problem of joining Ti-6Al-4V to other components is important in the lightweight research. A. Sharma and B. Ahn addressed the topical issue of metal ceramic fusion bonding with the study of braze joining of Ti-6Al-4V with zirconia (ZrO_2) by developing a new filler material based on Ag-Cu-Ti ternary alloy. Improved wettability of the filler material leading to stronger joints was achieved by the addition of specific amount of nanosized ceria (0.05 wt.% CeO_2) particles.

L. Fan et al. studied the effect of precision forming on the quality of submerged arc-welded pipes. They developed an analytical method to predict the spring-back in real time in order to develop precision forming by crimping. D. Lv et al. also studied the issue of a drill pipe joint which provides connection, transformation, and transmission of torque for high-speed drilling in the petroleum industry. The effects of Al-Zn coatings on the adhesive strength, morphology of microstructure, and corrosion resistance were studied.

X. Li et al. analysed different strength factors of a conveyor belt where a joint between the steel rope and rubber was obtained by an adhesive layer. They employed computational methods to analyse the integrity of the conveyor belt splices.

Aluminium is another candidate material often used for light weight. Its uses with other structural materials made joining a topical issue. Y. Ge and Y. Xia addressed the dynamic behaviour of dissimilar joints of aluminium and steel sheets for both self-piercing riveting and mechanical clinching process. Their study concluded that the joint strength can be significantly improved by prestraining through baking process.

The compilation of papers in this special issue covers a wide range of issues relating to innovations and research development in the use of lightweight and addressing processing issues. It is hoped that they will generate more interest that will spring more discussions on this and other related issues.

Conflicts of Interest

The guest editors declare that there are no conflicts of interest involved in this special issue.

Acknowledgments

The editors would like to thank the authors for their excellent contributions. The editors also want to express their gratitude to the reviewers for their support during the review

process by providing constructive criticism to improve the quality of the papers in a timely manner.

Rezwanul Haque
Ayodele Olofinjana
Benjamin Imasogie

References

- [1] J. Chen, E. Salvati, F. Uzun et al., "An experimental and numerical analysis of residual stresses in a TIG weldment of a single crystal nickel-base superalloy," *Journal of Manufacturing Processes*, vol. 53, pp. 190–200, 2020.
- [2] Y. Gao, L. J. Huang, Y. Bao et al., "Joints of TiBw/Ti6Al4V composites- Inconel 718 alloys dissimilar joining using Nb and Cu interlayers," *Journal of Alloys and Compounds*, vol. 822, 2020.
- [3] N. Z. Borba, J. Korbelen, B. Fiedler, J. F. dos Santos, and S. T. Amancio-Filho, "Low-velocity impact response of friction riveted joints for aircraft application," *Materials & Design*, vol. 186, 2020.
- [4] E. Petersen, J. Koord, O. Volkerink, D. Stefaniak, and C. Huhne, "Experimental and numerical investigation of the transition zone of locally steel-reinforced joining areas under combined tension-bending loading," *Journal of Composite Materials*, 2019, In press.
- [5] H. Vemanaboina, G. Edison, and S. Akella, "Validation of residual stress distributions in multipass dissimilar joints for GTAW process," *Journal of Engineering Science and Technology*, vol. 14, no. 5, pp. 2964–2978, 2019.
- [6] X. Y. Gu, C. L. Sui, J. Liu, D. L. Li, Z. Y. Meng, and K. X. Zhu, "Microstructure and mechanical properties of Mg/Al joints welded by ultrasonic spot welding with Zn interlayer," *Materials & Design*, vol. 181, 2019.
- [7] P. H. Shah and V. J. Badheka, "Friction stir welding of aluminium alloys: an overview of experimental findings-process, variables, development and applications," *Proceedings of the Institution of Mechanical Engineers, Part L: Journal of Materials: Design and Applications*, vol. 233, no. 6, pp. 1191–1226, 2019.
- [8] S. J. Chen, X. Wang, T. Yuan, and X. X. Li, "Research on prediction method of liquation cracking susceptibility to magnesium alloy welds," *Acta Metallurgica Sinica*, vol. 54, no. 12, pp. 1735–1744, 2018.

Research Article

Study on Properties of Cold-Sprayed Al-Zn Coating on S135 Drill Pipe Steel

Dongli Lv ^{1,2}, Tao Zhang ², and Feiyang Gong¹

¹School of Material Science and Engineering, Southwest Petroleum University, Chengdu 610500, China

²School of Oil and Natural Gas Engineering, Southwest Petroleum University, Chengdu 610500, China

Correspondence should be addressed to Dongli Lv; lvl393@163.com

Received 20 November 2019; Revised 6 January 2020; Accepted 17 January 2020; Published 12 February 2020

Guest Editor: Ayodele Olofinjana

Copyright © 2020 Dongli Lv et al. This is an open access article distributed under the Creative Commons Attribution License, which permits unrestricted use, distribution, and reproduction in any medium, provided the original work is properly cited.

With the gradual depletion of shallow resources, the petroleum industry is developing toward ultradeep wells and high-speed drillings, and the problems of corrosion and erosion failure of drill pipe materials are becoming more and more serious. On the basis of not destroying the excellent mechanical properties of S135 drill pipe steel, three kinds of coatings, 20% Al-80% Zn, 30% Al-70% Zn, and 40% Al-60% Zn, are cold sprayed on S135 steel. The morphology of the coating is observed, and the bonding strength, porosity, hardness, and corrosion resistance of the coating are tested. Results show that the bonding mechanism between the powder particles and the substrate of the three coatings is mainly mechanical occlusion. From the substrate to the coating surface, the hardness value decreases gradually. With the increase of Al powder content, coating bonding strength increases, coating becomes more compact, and porosity decreases. Corrosion test results show that three coatings can protect the substrate. The density of corrosion products on the coating surface increased with the increase of the Al content. Corrosion potential of the three coatings is lower than that of the substrate, and the corrosion rate of the three coatings is lower than that of the substrate.

1. Introduction

In recent years, with the gradual depletion of shallow resources, the petroleum industry is developing toward ultradeep wells and high-speed drilling. S135 steel is widely used as drill pipe material because of its excellent mechanical properties [1]. As an important part of the drill string system, the drill pipe is often used as the circulation channel of drilling fluid. The drill pipe joint is the most important part of the drilling string. It plays the role of connecting, transforming, and transmitting torque. It must have high strength, plasticity, and other comprehensive mechanical properties. In the process of service, it is often affected by the corrosive medium, which makes the joint usually have corrosion behavior, so more than 80% of drill pipe accidents occur at joints. In recent years, the incidence of drill pipe failure accidents is very high, and the losses caused by the drill pipe failure also increased significantly [2, 3]. It is necessary to find a surface treatment method to improve the surface properties of a material while retaining the excellent

mechanical properties of S135 drill pipe steel, which is very necessary for improving the life of drill pipe and drilling efficiency [4].

The coating preparation technology has been paid close attention by domestic and foreign research institutions in recent years. The protective coating with excellent corrosion resistance and wear resistance can be prepared by thermal spraying or enamel technology. It has been widely used and developed because of its mature technology, convenient preparation, and flexible application, but there are inevitably many defects [5–9]. Cold spraying technology is a technology in which metal particles hit the substrate surface at high speed and form a dense coating on the substrate surface [10]. Compared with thermal spraying, cold spraying accelerates powder particles by compressed gas, and particles impact the surface of the substrate by their kinetic energy. After collision, plastic deformation occurs, which binds to the substrate and deposits a coating. Cold spraying can not only obtain nonoxidized metal deposits in the atmosphere, but also avoid the thermal impact on the substrate, which

makes cold spraying technology have broad application prospects in corrosion protection and preparation of high conductivity coatings, repair of damaged metal components, and manufacture of metal additives.

Under the action of high-speed and high-pressure gas, the fully solidified high-speed particles collide with the substrate violently, and the particles deform plastically and deposit, forming a cold spray coating. Assadi et al. used the finite element method to simulate the stress field and temperature field distribution of particles bonded to the substrate. The results showed that there was microzone melting at the particle edge and proposed that metallurgical bonding might exist in the process of cold spraying [11, 12]. Al coating can provide good cathodic protection for steel surface, and the performance of protective coating is better than that of thermal spraying [13]. In terms of electrochemical protection, Zn has a better effect than Al. While in terms of electrochemical stability, Al has a better effect than Zn. At the same time, by comparison with the two elements, it can be found that zinc-aluminum composite coating is a more excellent coating material combining the excellent cathodic protection of Zn and the excellent chemical stability of Al [14, 15]. Al-Zn composite coating has lower porosity and better corrosion resistance than pure aluminum and zinc coatings [16–18]. The composite coating with the substrate and the internal powder of the coating can be well combined, and the Al-Zn alloy coating prepared by cold spraying has higher wear resistance [19].

In this paper, three proportions of Zn-Al coatings, 20% Al-80% Zn, 30% Al-70% Zn, and 40% Al-60% Zn, were sprayed on the surface of S135 steel which was commonly used in oil drilling engineering. Microstructure, morphology, porosity, hardness, bonding strength, and corrosion resistance of three coatings were observed and studied.

2. Experimental Process

2.1. Experimental Materials. The substrate material used in the experiment is S135 steel plate, and its chemical composition is shown in Table 1. The substrate thickness is 10 mm.

Figure 1 shows the micromorphology of Al and Zn powders. The particles of Zn powders were spherical and ranging from 5 to 14 μm in size. The particles of Al powders were not uniform, and most of them are strip or wormlike, ranging from 15 to 45 μm in size. The purity of the two kinds of metal powder was more than 99.9%.

2.2. Preparation of Spray Coating. In order to improve the mechanical occlusal effect between the coating and the metal substrate, acetone and alcohol were used for ultrasonic cleaning to remove stains and rust on the substrate surface before spraying. Sandblasting pretreatment with quartz sand was used to increase the roughness of the substrate surface, which was beneficial to the bonding between the coating material particles and the substrate. Metal powders of Al and Zn were mechanically mixed at the weight proportions of 20% Al-80% Zn, 30% Al-70% Zn, and 40% Al-60% Zn,

respectively. Low pressure cold spraying equipment (DYMET-413) was used for spraying. Figure 2 shows the working principle of the cold spraying system. The gas is pressurized by a compression device and then heated through a heater to expand at supersonic speeds at the nozzle outlet. Metal powder particles are accelerated to supersonic velocity by high pressure heating gas at the front of the spray gun and then rushed to the surface of the substrate to bond with it. The working gas was N_2 , the spray gas pressure was 0.8 MPa, and the powder feeding rate was 0.556 g/s~1.389 g/s. Spraying temperature was 500°C. The distance between the spray gun and the surface of the substrate was maintained at 15~30 mm, and the lateral movement was at the speed of 20~30 mm/s. The thickness of coating was measured with a vernier caliper. The thickness of the coating was obtained by subtracting the thickness of the substrate before spraying from the thickness of the test piece after spraying. Five measuring points were selected on the spraying test piece to obtain the average thickness. The thickness of 20% Al-80% Zn coating was 327 μm , 30% Al-70% Zn coating was 346 μm , and 40% Al-60% Zn coating was 367 μm .

3. Results and Discussions

3.1. Microstructure Observation of Coating. Figure 3 shows the micromorphology of coatings with three powder ratios observed by scanning electron microscopy. It can be seen from the figures that the surface of the three kinds of coatings is uneven, and there are some round particles with a diameter of about 5 μm . There is a critical deposition velocity determined by material properties in cold spraying. Only the powder beyond the critical velocity can be deposited on the substrate to form the coating [20, 21]. Most of the powder particles have severe plastic deformation, while a few of the small particles have not been fully deposited due to their impact velocity not reaching the critical velocity, so there are a few particle gaps or holes on the coating surface. With the increase of the relative content of aluminum powder particles, the roughness of the coating decreases, porosity of the coating surface decreases gradually, and the coating becomes more compact. Because the particle size of aluminum metal powder is larger than that of zinc metal powder and irregular, the kinetic energy of aluminum powder particles impacting on the substrate is larger in the gas-solid two-phase flow field during spraying process. After aluminum powder particles continuously impacting on the substrate, the crystal blocks are broken and refined, the deformation is obvious, and most of them are flat. Zinc powder particles are brittle at a certain temperature. It is easy to be broken into fine particles and deposited in the process of coating preparation, which makes the coating more compact and greatly reduces voids caused by overlapping particles, thus reducing the porosity and the roughness of the coating.

Figure 4 shows the microstructure photos of the three polished coating sections. It can be observed that the three coatings are even and flat, the micropores formed in the deposition of Al and Zn powders are less, and the combination is compact. In the coating, aluminum-zinc powder particles become soft due to continuous heating by heated

TABLE 1: Chemical composition of S135 steel (wt.%).

C	Si	Mn	S	P	Ni	Cr	Mo	Ti	Cu	Fe
0.28	0.25	0.64	0.004	0.008	0.29	0.98	0.42	0.009	0.02	96.876

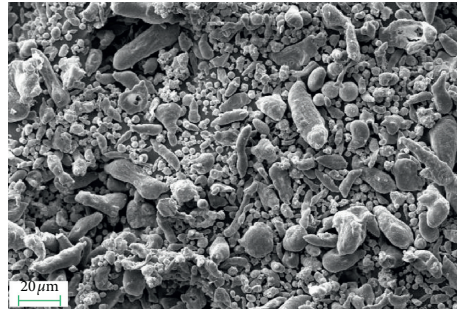


FIGURE 1: SEM image of mixed powder of Al and Zn (40% Al-60% Zn).

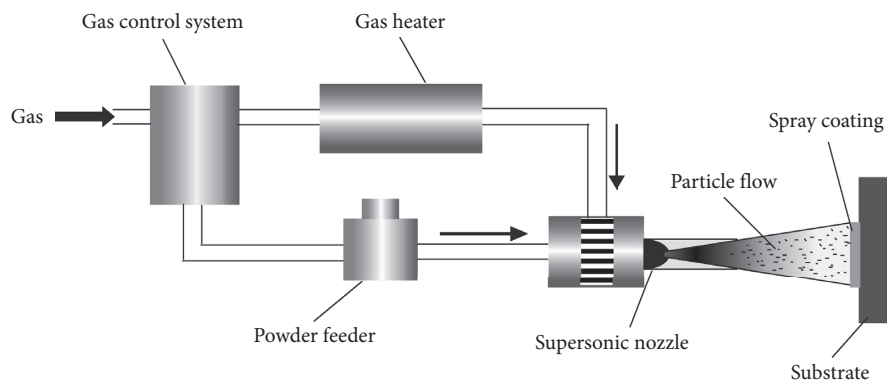


FIGURE 2: Principle diagram of cold spraying process.

gas and are continuously impacted by subsequent particles, resulting in obvious plastic deformation. The mutual squeezing between the particles causes the two powders to mechanically bond together, presenting a flat strip bonding form and piling up layer by layer to form a dense coating. With the increase of the content of aluminum powder, the plastic deformation degree of powder particles is increased, and the flat strip structure formed by the combination of the two powder particles is more compact.

Porosity directly affects the performance of coatings. When coatings are used for corrosion resistance, the value of porosity is a key index to measure the quality of coatings. When the porosity is high, the corrosion rate of the coating accelerates, and the corrosive medium can easily enter into the coating or intensifies the corrosion of the substrate interface, which leads to the decrease of the corrosion resistance of the coating. The porosity of coatings was calculated with the aid of image processing method [22]. By using M180-50120 metallographic examination software system, the porosity of the coating is evaluated automatically by “calculating the distribution and size of porosity.” The gray value of the metallographic photograph is analyzed by the gray value method in the metallographic inspection software system to capture the position and size of the pores

and determine the porosity of the coating. The porosity of the three coatings is shown in Figure 5. It can be seen from the figure that the porosity of the coating decreases gradually with the increase of aluminum powder content in the coating and the decrease of zinc powder content. When the metal powder particles impact S135 steel matrix during spraying, both of them have plastic deformation, which makes the surface of the matrix appear pits, and the coating powder is trapped in the pits to form mechanical bond. Within the coating, along the stacking direction of the coating, the plastic deformation of the powder particles decreases, the incomplete overlapping rate of the powder increases, the coating structure gradually becomes loose, and the pores gradually increase. With the increase of Al content in the powder, the large size of Al particles is easy to accelerate in the gas-solid two-phase flow field, the deposition efficiency of the whole coating increases, and the large kinetic energy is obtained to generate sufficient plastic deformation. In addition, the continuous impact of the powder particles makes the crystal block broken and refined, greatly reducing the incomplete overlap between the particles and reducing the porosity. The porosity of the three types of cold spraying coatings are all less than 1.6%, of which the 40% Al-60% Zn coating was only 0.62%, indicating that the porosity

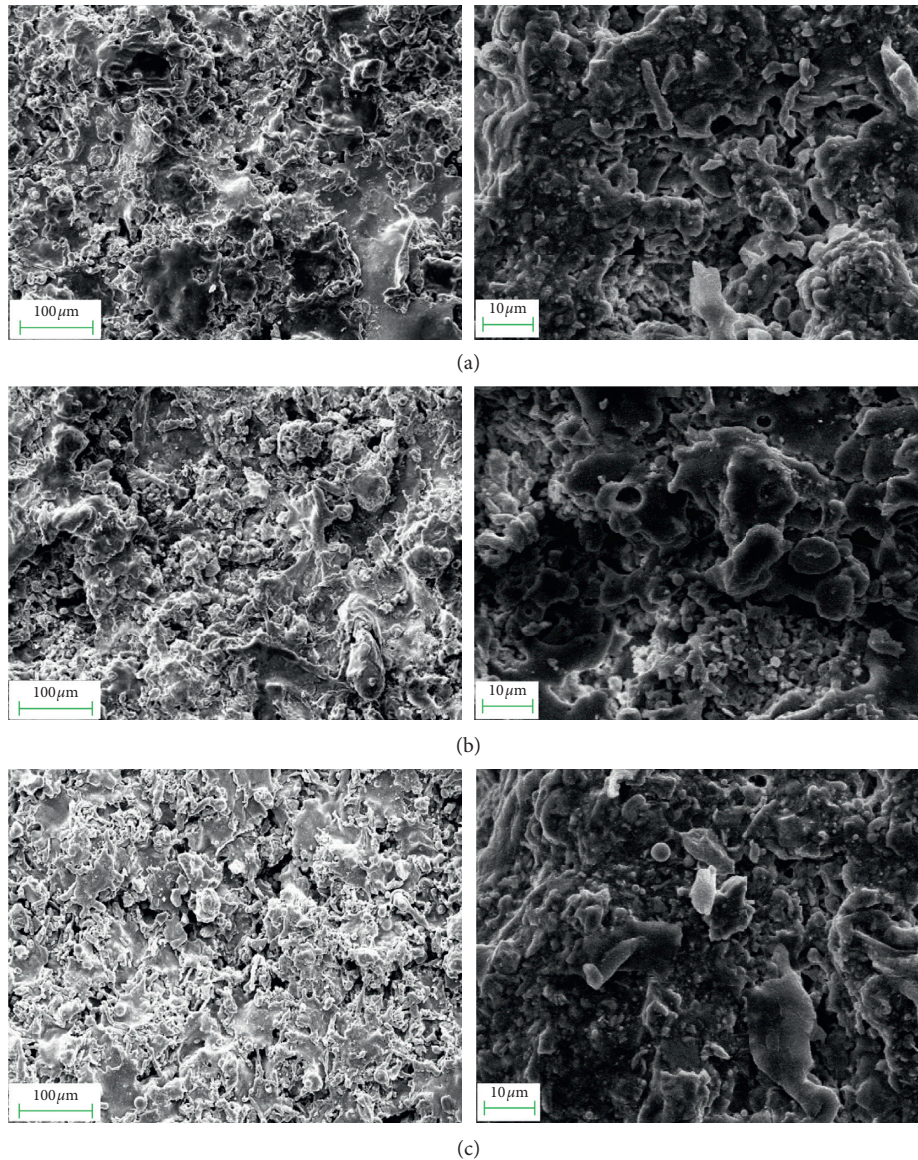


FIGURE 3: Surface micromorphology of different coatings: (a) 20% Al-80% Zn, (b) 30% Al-70% Zn, and (c) 40% Al-60% Zn.

of the three types of cold spraying coatings produced in this experiment is lower than that of the thermal spraying coating in which porosity is usually 5%–15%. [23, 24].

3.2. Hardness and Bonding Strength of Coatings. Coating hardness is a key index to evaluate the quality of coatings, and it can reflect the wear resistance of coatings. When the particle velocity reaches the critical velocity, severe plastic deformation will occur after the particle impacts the substrate and then the coating will be deposited. In addition, some particles whose velocity is less than critical velocity will produce shot peening strengthening effect on the deposited coatings, which will result in deformation hardening effect in the coatings.

Figure 6 is a schematic diagram of the hardness testing position. Five locations are taken from the substrate to the

coating along the thickness direction for hardness testing. Five points in the horizontal direction are taken for hardness testing at each location, and then the average value is taken as the hardness value of the position. The hardness result is shown in Figure 7. According to the figure, the hardness values of the three coatings decrease gradually from the substrate to the surface of the coatings. Because of the high hardness of the substrate, the spray particles impact the substrate at high speed and form the initial coating. The initial coating is greatly affected by the matrix hardness, so the hardness is higher. At the same time, the impact of subsequent particles also strengthens the deposited coating and obviously improves the hardness of the coating. The closer the coating surface is, the less and less the impact of subsequent particles on the coating is, and the weaker the hardness strengthening effect is. As the hardness of the zinc powder particle is much higher than that of aluminum

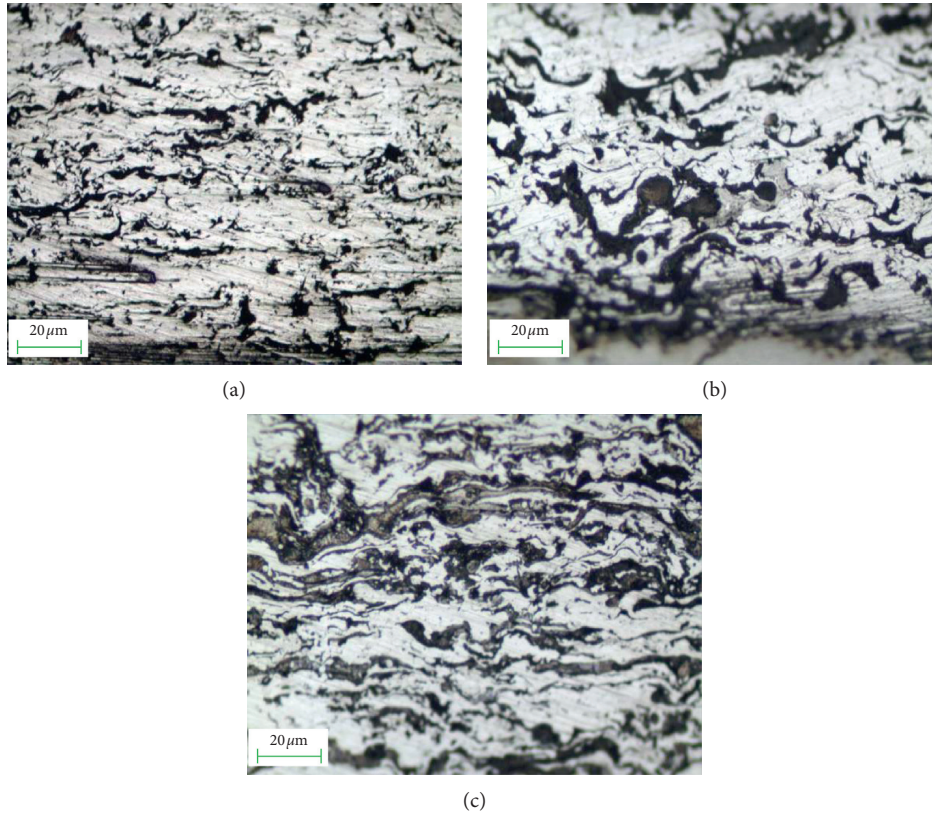


FIGURE 4: Metallographic photograph of the coating section: (a) 20% Al-80% Zn, (b) 30% Al-70% Zn, and (c) 40% Al-60% Zn.

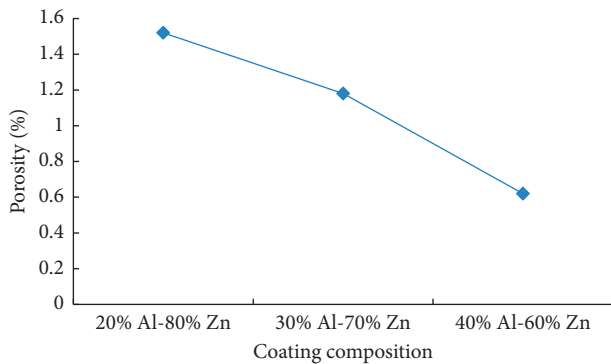


FIGURE 5: Porosity variation of the three coatings.

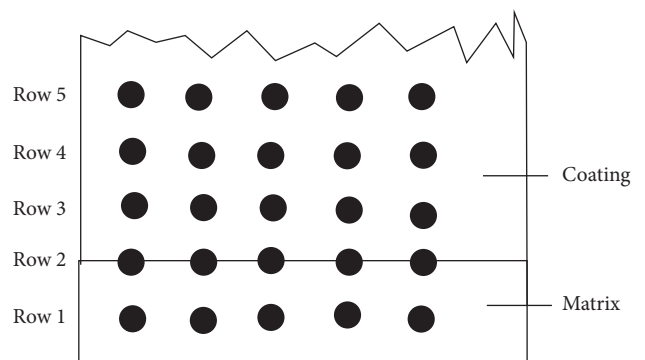


FIGURE 6: Schematic diagram of the hardness testing position.

powder particle, the hardness of coating increases with the increase of the content of zinc powder particles. Because the drill pipe joint is more prone to corrosion failure, the surface hardness requirement of drill pipe joint is not as high as that of corrosion resistance. In this paper, although the hardness of the coating obtained by cold spraying Al-Zn coating is lower than that of the substrate, we can try to improve the hardness in the follow-up study, in order to obtain a coating with better comprehensive performance.

As another important performance index of coating, bonding strength can reflect the bonding between coating and substrate or the adhesion inside coating, directly reflect the mechanical properties of coating, and affect the service life of coating. On the multifunctional material surface

performance testing machine, the scratch test was carried out on the coating surface with 120° natural diamond indenter. Under the condition of the preloading load of 15 N, loading speed of 100 N/min, and scratch length of 10 mm, the acoustic signal of scratch interface is collected by the acoustic signal receiver. The bonding strength between coating and S135 steel substrate is reflected by the magnitude of loading force when the acoustic signal changes abruptly. The scratches produced by the indenter on the substrate are shown in Figure 8. The craters can be clearly observed in scratch photographs which prove that the coating has been scratched to the substrate when the sound signal suddenly changes. There is no large area of coating falling off on both sides of the scratch, showing good bonding performance

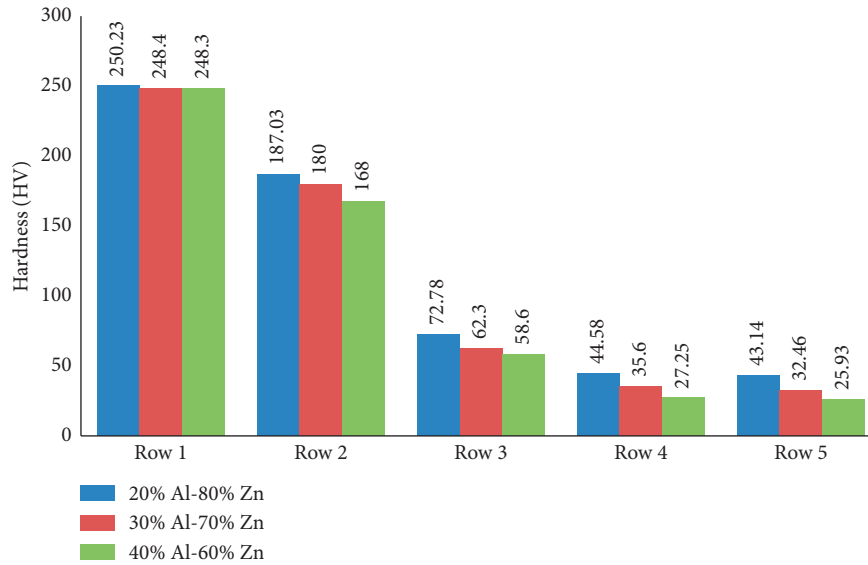


FIGURE 7: Hardness of the three coatings.

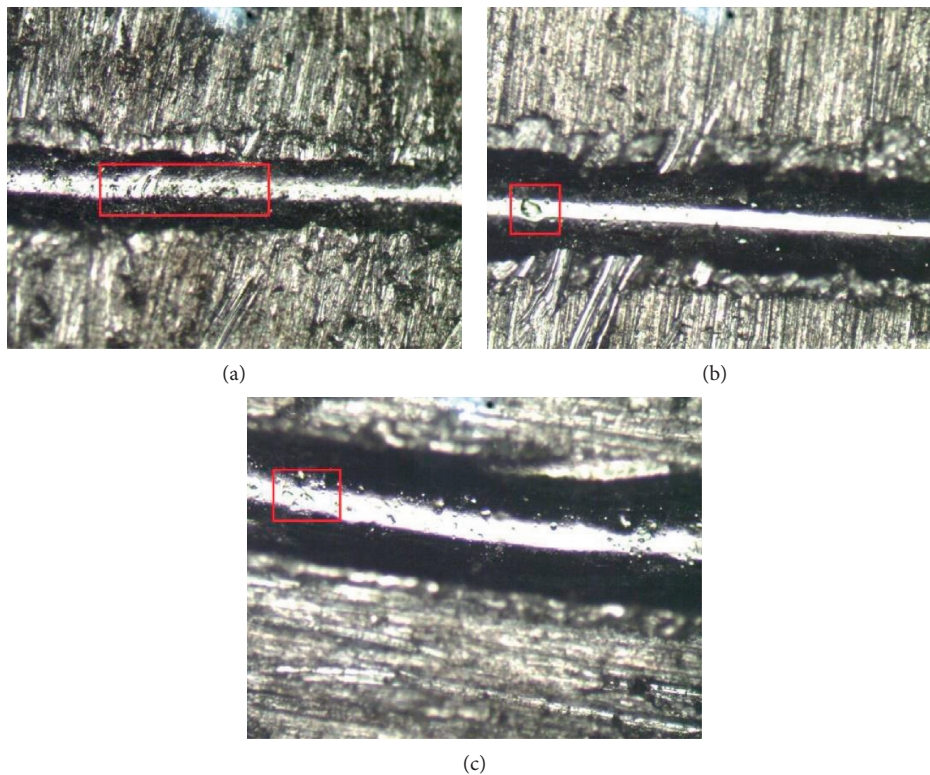


FIGURE 8: Scratch charts of three coatings: (a) 40% Al-60% Zn, (b) 30% Al-70% Zn, and (c) 20% Al-80% Zn.

with the substrate. The critical loading forces between the coating and the substrate are measured as shown in Table 2. It can be seen from the table that different loading forces are required to penetrate the binding interface of the three coatings and the substrate. The bonding strength of the coating increases with the increase of the Al content. Due to the large particle size of Al metal powder, it is easy to be accelerated in the gas-solid two-phase flow field during

spraying, and the kinetic energy obtained and the impact force generated when it collides with the matrix are large. At the same time, due to the large amount of plastic deformation caused by the irregular shape of Al particles, the bonding strength between powder particles and matrix is improved. The critical failure loads of the three coatings are not very large, which is mainly related to the hardness of the matrix material. Because, under the external load, the

TABLE 2: Critical loading force of three coatings.

Powder proportion	Critical loading force (N)
20% Al-80% Zn	41.73
30% Al-70% Zn	44.53
40% Al-60% Zn	48.95

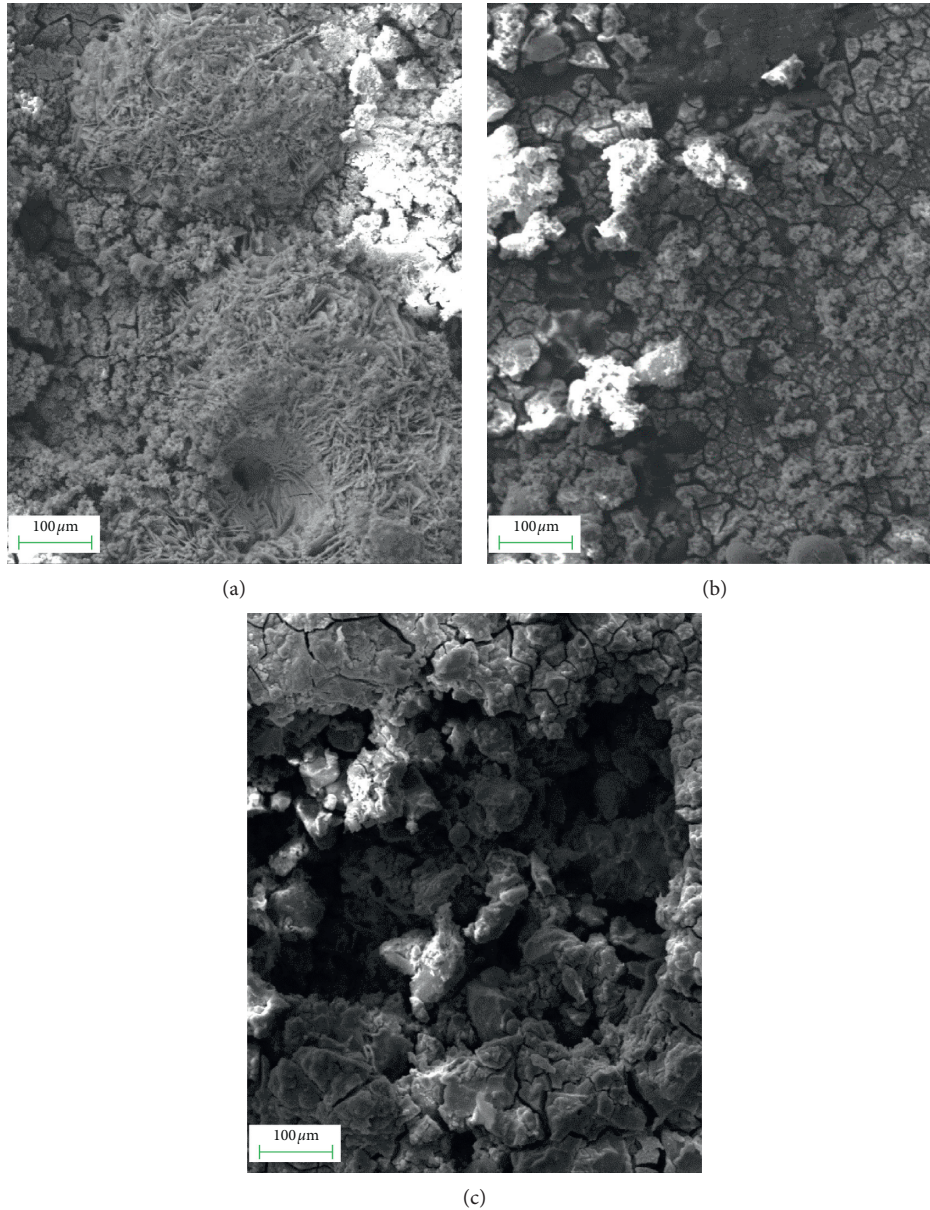


FIGURE 9: SEM diagram of surface morphology of coating after corrosion: (a) 40% Al-60% Zn, (b) 30% Al-70% Zn, and (c) 20% Al-80% Zn.

deformation of the coating and the substrate must be in a state of collaborative deformation, so that the film has the best bonding performance.

3.3. Corrosion Behavior of Coatings. As a kind of anode coating, Al coating not only has the function of isolating corrosion medium and making it unable to react with the

substrate but also is a kind of sacrificial anode material, which plays the role of cathodic protection. Zn coating is often used as sacrificial anode to protect steel. Al-Zn composite coating has both advantages. 10% NaCl solution was chosen as corrosion solution in the immersion corrosion experiment. The morphology of coating was observed after 480 hours. By observing the corrosion surface morphology of the three coatings after immersion corrosion, it was found

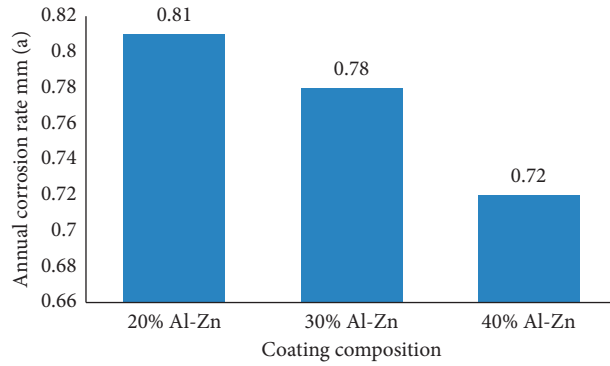


FIGURE 10: Corrosion rate of each coating.

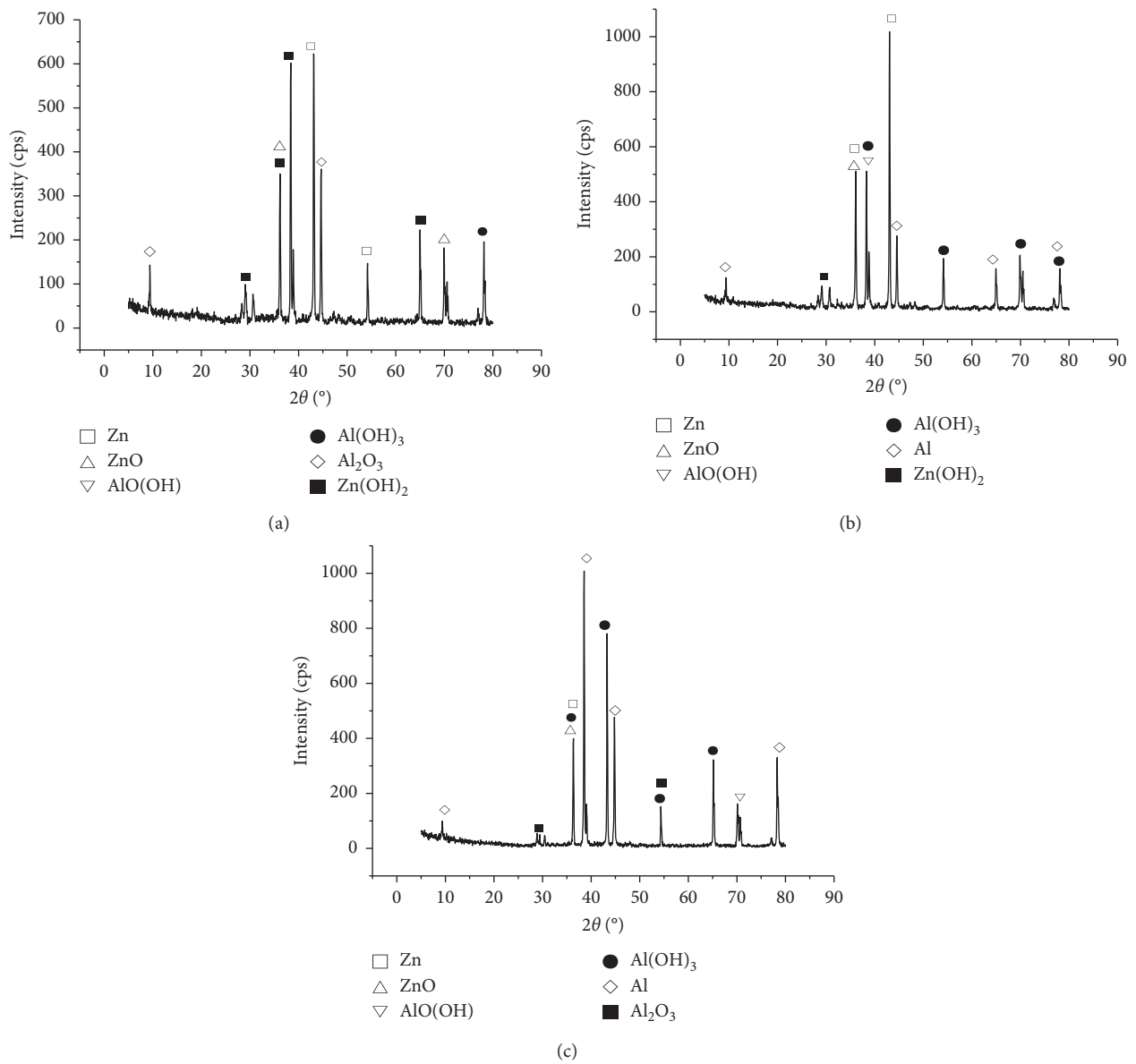


FIGURE 11: XRD diagrams of three coatings after corrosion: (a) 20% Al-80% Zn, (b) 30% Al-70% Zn, and (c) 40% Al-60% Zn.

that a layer of white dense corrosion products was deposited on the coating surface. The surface morphology of the coating after corrosion is shown in Figure 9. It can be seen that a few holes and island particles appeared on the surface of the coatings. The distribution of corrosion products is uneven, and there are obvious corrosion pits and agglomeration of corrosion products around the corrosion pits. The corrosion products of coating 40% Al-60% Zn are relatively dense, and most of the corrosion products are flocculent. The density of corrosion products on the coating surface increased with the increase of the Al content. When the content of Al is relatively low, Zn is relatively active and is first corroded, forming a cathodic protection effect on Al. From the overall corrosion morphology, with the increase of the Al content, the density of corrosion products on the coating surface increased. The denser the corrosion product, the more it can prevent the coating being corroded.

The samples were weighed before and after corrosion, and the average annual corrosion rate was calculated according to the corrosion weight loss of the measured samples. The calculation formula is as follows:

$$V_a = C \times \frac{W_0 - W}{\rho A t}, \quad (1)$$

where V_a is the annual corrosion rate; C is the conversion factor, and its value is 8.76×10^4 ; W_0 is the quality of samples before corrosion; W is the quality of the sample after corrosion; A is the surface area of the sample; ρ is the density of the coating surface; and t is corrosion time.

According to equation (1), the corrosion rate of each coating is shown in Figure 10. The annual corrosion rate of the coating is 20% Al-Zn, 30% Al-Zn, and 40% Al-60% Zn from large to small.

Figure 11 shows the XRD composition of three coatings after corrosion. From the diagram, the three coatings contain AlO(OH), Al(OH)₃, ZnO, and Al₂O₃. Passivation film is easily formed by oxidation of aluminum in aqueous solution. The anode first undergoes the anodic dissolution reaction of aluminum. With the corrosion reaction proceeding, the passive film on the coating surface is destroyed, and the corrosion reaction of the coating is intensified. In the subsequent corrosion process, because zinc is more active than the oxide film of aluminum, it can protect the oxide film of aluminum. With the continuous dissolution of zinc and the formation of ZnO·H₂O with the OH⁻ generated from the cathode, the product will cover the coating surface. These corrosion products can play a role of "self-sealing" plugging the pores, to some extent, blocking the penetration and diffusion of the medium into the coating [18].

The polarization curves of three coatings in 3.5% NaCl solution are shown in Figure 12. The corresponding polarization curve fitting results are also listed in Table 3. There is no obvious passivation zone in the polarization process of the three coatings. The corrosion potential of the three coatings is lower than that of the substrate. The corrosion rate of the three coatings in 3.5% NaCl solution is lower than that of the substrate. With the increase of the content of Al

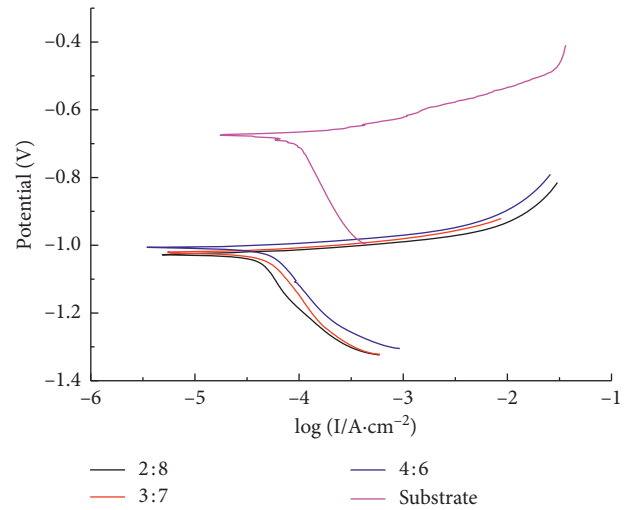


FIGURE 12: Polarization curves of three coatings in 3.5% NaCl solution.

TABLE 3: Fitting results of several polarization parameters.

Sample	$I_{\text{corr}} (\mu\text{A})$	$E_{\text{corr}} (\text{V})$
20% Al-Zn	52.40	-1.026
30% Al-Zn	47.80	-1.022
40% Al-Zn	42.10	-1.010
Substrate	63.70	-0.675

powder in the metal powder, the corrosion potential of the coating increases, and the corrosion rate of the coating decreases which is more conducive to the protection of the substrate.

4. Conclusion

- (1) Three kinds of coatings were prepared by cold spraying technology, and no obvious defects were observed in the coatings. With the increase of the relative content of Al powder particles, the roughness of the coating decreased, porosity of the coating surface decreased from 1.52% to 0.62%, and the coating became more compact. The denser the coating is, the more effective it is to protect the S135 drill pipe joint material from corrosion.
- (2) From the substrate to the coating surface, the hardness value decreases gradually. The hardness of coating increases with the increase of the content of zinc powder particles. The bonding mechanism between the powder particles and the substrate of the three coatings is mainly mechanical occlusion. With the increase of the metal Al powder content, coating bonding strength increased.
- (3) The potential of the three coatings is negative compared with the substrate. With the increase of the content of Al powder in the metal powder, the corrosion potential of the coating increased from -1.026 V to -1.01 V. The corrosion rate of the three coatings is lower than that of the substrate. In

immersion corrosion experiments, the distribution of corrosion products is uneven, and there are obvious corrosion pits and agglomeration of corrosion products around the corrosion pits. With the increase of the Al content, the density of corrosion products on the coating surface increased. Three coatings can provide effective corrosion protection for the substrate.

Data Availability

The data used to support the findings of this study are available from the corresponding author upon request.

Conflicts of Interest

The authors declare that they have no conflicts of interest.

Acknowledgments

The authors would like to acknowledge the funding support by the Chinese National Natural Science Foundation (grant no. 51974271) and the Open Fund of State Key Laboratory of Oil and Gas Reservoir Geology and Exploitation (Southwest Petroleum University) (grant no. PLN1520).

References

- [1] F.-p Li, L.-h Han, Y.-g Liu, and Y. Wang, "Investigation on toughness index of high grade steel drill pipe," *Journal of China University of Petroleum (Edition of Natural Science)*, vol. 35, no. 5, pp. 130–133, 2011.
- [2] J. Li and J. Zhu, "Study on fracture characteristics of S135 steel for drill pipes," *Foundry Technology*, vol. 36, no. 10, pp. 2477–2478, 2015.
- [3] K. A. Macdonald and J. V. Bjune, "Failure analysis of drill strings," *Engineering Failure Analysis*, vol. 14, no. 8, pp. 1641–1666, 2007.
- [4] S. Moradi and K. Ranjbar, "Experimental and computational failure analysis of drillstrings," *Engineering Failure Analysis*, vol. 16, no. 3, pp. 923–933, 2009.
- [5] R. M. H. Pombo Rodriguez, R. S. C. Paredes, S. H. Wido, A. Calixto, and H. Schreiner, "Comparison of aluminum coatings deposited by flame spray and by electric arc spray," *Surface and Coatings Technology*, vol. 202, no. 1, pp. 172–179, 2007.
- [6] L. Fan, F. Tang, G. Chen, S. T. Reis, and M. L. Koenigstein, "Corrosion resistances of steel pipe coated with two types of enamel by two coating processes," *Journal of Materials Engineering and Performance*, vol. 27, no. 10, pp. 5341–5349, 2018.
- [7] R. Nikbakht, S. H. Seyedein, S. Kheirandish, H. Assadi, and B. Jodoin, "The role of deposition sequence in cold spraying of dissimilar materials," *Surface and Coatings Technology*, vol. 367, pp. 75–85, 2019.
- [8] L. Fan, F. Tang, S. T. Reis, G. Chen, and M. L. Koenigstein, "Corrosion resistances of steel pipes internally coated with enamel," *Corrosion*, vol. 73, no. 11, pp. 1335–1345, 2017.
- [9] L. Fan, S. Reis, G. Chen, and M. Koenigstein, "Corrosion resistance of pipeline steel with damaged enamel coating and cathodic protection," *Coatings*, vol. 8, no. 5, p. 185, 2018.
- [10] China National Defense Science and Technology Information Center, *World Weapons and Equipment and Military Technology Annual Development Report 2014*, China National Defense Science and Technology Information Center, Beijing, China, 2015.
- [11] G.-f. Zhao, Y.-y. Wang, H.-l. Zhang, J.-l. Tang, and Y.-d. Chen, "Application of cold spraying equipment and cold spraying technology," *Surface Technology*, vol. 46, no. 11, pp. 198–205, 2017.
- [12] H. Assadi, H. Kreye, F. Gärtner, and T. Klassen, "Cold spraying—a materials perspective," *Acta Materialia*, vol. 116, pp. 382–407, 2016.
- [13] D. Persson, D. Thierry, and N. LeBozec, "Corrosion product formation on Zn55Al coated steel upon exposure in a marine atmosphere," *Corrosion Science*, vol. 53, no. 2, pp. 720–726, 2011.
- [14] C. Walde, D. Cote, V. Champagne, and R. Sisson, "Characterizing the effect of thermal processing on feedstock Al alloy powder for additive manufacturing applications," *Journal of Materials Engineering and Performance*, vol. 28, no. 2, pp. 601–610, 2019.
- [15] S. Ngai, T. Ngai, F. Vogel, W. Story, G. B. Thompson, and L. N. Brewer, "Saltwater corrosion behavior of cold sprayed AA7075 aluminum alloy coatings," *Corrosion Science*, vol. 130, pp. 231–240, 2018.
- [16] P. Nautiyal, C. Zhang, V. Champagne, B. Boesl, and A. Agarwal, "In-situ creep deformation of cold-sprayed aluminum splats at elevated temperatures," *Surface and Coatings Technology*, vol. 372, pp. 353–360, 2019.
- [17] Z.-c. Shi, X.-y. Zhang, H. Chen et al., "Properties of cold spray Al/Zn coatings on high-strength steel," *Journal of Materials Engineering*, vol. 43, no. 2, pp. 14–19, 2015.
- [18] C. Xie, H. Li, X. Zhou, and C. Sun, "Corrosion behavior of cold sprayed pure zinc coating on magnesium," *Surface and Coatings Technology*, vol. 374, pp. 797–806, 2019.
- [19] C. J. Huang, K. Yang, N. Li et al., "Microstructures and wear-corrosion performance of vacuum plasma sprayed and cold gas dynamic sprayed Muntz alloy coatings," *Surface and Coatings Technology*, vol. 371, pp. 172–184, 2019.
- [20] W.-Y. Li, H. Liao, C.-J. Li, G. Li, C. Coddet, and X. Wang, "On high velocity impact of micro-sized metallic particles in cold spraying," *Applied Surface Science*, vol. 253, no. 5, pp. 2852–2862, 2006.
- [21] F. Raletz, M. Vardelle, and G. Ezo'o, "Critical particle velocity under cold spray conditions," *Surface and Coatings Technology*, vol. 201, no. 5, pp. 1942–1947, 2006.
- [22] D. Lv, Z. Lian, and T. Zhang, "Study of cavitation and cavitation erosion quantitative method based on image processing technique," *Advances in Civil Engineering*, vol. 2018, Article ID 5317578, 10 pages, 2018.
- [23] A. G. Jo and C. C. Berndt, "Effects of standoff distance on porosity, phase distribution and mechanical properties of plasma sprayed Nd-Fe-B coatings," *Surface and Coatings Technology*, vol. 216, pp. 127–138, 2013.
- [24] G. A. Baglyuk, S. G. Pyatachuk, and A. A. Mamonova, "The structure and properties of boride coatings depending on the porosity of powder steel preforms," *Powder Metallurgy and Metal Ceramics*, vol. 53, no. 7–8, pp. 417–422, 2014.

Research Article

Analysis of Strength Factors of Steel Cord Conveyor Belt Splices Based on the FEM

Xianguo Li ^{1,2}, Xinyu Long^{1,3}, Zhenqian Shen ¹, and Changyun Miao¹

¹Tianjin Polytechnic University, Tianjin 300387, China

²Tianjin Key Laboratory of Optoelectronic Detection Technology and System, Tianjin 300387, China

³Nankai University, Tianjin 300350, China

Correspondence should be addressed to Xianguo Li; lixianguo@tjpu.edu.cn and Zhenqian Shen; shenzhenqian@tjpu.edu.cn

Received 29 August 2019; Accepted 7 December 2019; Published 24 December 2019

Guest Editor: Benjamin I. Imasogie

Copyright © 2019 Xianguo Li et al. This is an open access article distributed under the Creative Commons Attribution License, which permits unrestricted use, distribution, and reproduction in any medium, provided the original work is properly cited.

Conveyor belt is an important element of the conveyor. The strength of the steel cord conveyor belt largely determines the carrying capacity, and it also has a great impact on operational safety. In this paper, the effect of different factors on the strength of the steel cord conveyor belt splices was studied. The FEM was used for simulation analysis, and the corresponding tensile experiments were carried out to verify. Steel cords of different lengths were simulated, and the simulation results agree well with the experimental results. On this basis, the steel cord length, steel cord diameter, rubber thickness, and different number of steel cords were investigated to study the effect on the pullout force of the steel cord conveyor belt splice. The numerical simulation results show that different steel cord diameters have more significant effect on the strength of the conveyor belt splice compared to rubber. The steel cord length and steel cord diameter impact on the steel cord conveyor belt is approximately linear. For the different number of the steel cords, the increase in the number of steel cords does not mean that the tension will increase by the same multiple, and the increase in pullout force is less than the increase in the number of steel cords. It provides guidance for the production of steel cord conveyor belts.

1. Introduction

As a continuously moving transport facility, the conveyor has been widely used in fields such as mining, coal, port, electric power, chemical industry, metallurgy, architecture, and food [1, 2]. Figure 1 shows the structure of a conveyor belt and three application fields of the conveyors. A conveyor belt is an important element of the conveyor. Its properties greatly affect the functions of the conveyor system. Especially, the strength of the conveyor belt largely determines the carrying capacity, and it also has a great impact on operational safety. Therefore, the strength of the conveyor belt has always been the focus of researchers and users.

In order to increase the strength of the conveyor belt, the steel cords are arranged inside the rubber. First and foremost, the weakest region in the conveyor belt is the splice [3]. The belt broken accidents would occur due to decrease in splice strength. In previous studies and publications,

researchers were more focused on the conveyor construction and conveyor belt splice strength detection. But for the strength factors of the steel cord conveyor belt splice, they paid insufficient attention, although the strength significantly affects the whole transport facility and even the whole system on the durability and reliability [4].

There have been various methods for detecting splice strength. In 1979, Harrison first proposed a nondestructive testing method for a steel rope of a conveyor belt based on the principle of electromagnetic induction and developed a CBM steel core conveyor belt steel rope detection device [5]. Based on this principle, similar devices have been developed by German DMT Company and American Goodyear Company [6]. In 2005, German Phoenix Conveyor Belt System Co., Ltd., designed a steel cord conveyor belt detection system using X-ray detection technology [7]. Our team developed a nondestructive testing system for the steel cord conveyor belt based on X-ray, which realized accurate

and reliable detection of splice twitch and steel cord breakage [8]. In 2013, Fedorko et al. proposed an experimental method based on CT technology for measuring the internal structure and dynamic characteristic parameters of the steel cord conveyor belt [9]. In 2015, Mazurkiewicz put forward a method of joint elongation monitoring based on fuzzy logic, which can realize the prediction and early warning of joint elongation by using the data acquired by using the electromagnetic induction sensor [10]. The above nondestructive testing technologies are increasingly mature and have been used in actual production. However, for the strength determination of the conveyor belt splice, all of these methods have the defects of poor accuracy and reliability.

In 2018, Bajda and Hardygóra analyzed the influence of the natural ageing time on the strength parameters of steel cord conveyor belts using the universal stretching machine. The tests included adhesion of the steel cords to the belt's core rubber and the tensile strength of both the carry and the pulley covers [11]. But the strength performance analysis of the conveyor belt splice is not covered in this paper.

For the FEM (finite element method) as an effective numerical analysis method, more and more attention is being paid in many simulation studies. Quite a lot of researchers are using FEM for the study of conveyor belts [12, 13]. In 2014, Taraba modelled the influence of the dynamic force of the steel cord conveyor belt which under the stress and strain conditions [14]. In 2017, Du et al. simulated the steel cord stress and fatigue life of the steel cord conveyor belt. A valuable conclusion has been obtained, which fully reflects the feasibility of finite element analysis [15]. In 2018, our group has studied the steel cord pitch of the conveyor belt splice. It is concluded that the steel cord spacing has a certain influence on the splice strength. If the spacing is too large or too small, the strength of the conveyor splice will be reduced. This provided a theoretical basis for the selection of the overlap spacing of our splice steel cord [16–18].

In order to study the other factors those influence the strength of the conveyor belt and analyze the trends in the effects of each factor on the strength, in this paper, we will simulate and analyze the dynamic properties of the conveyor belt by using Abaqus. Four factors including the steel cord length, diameter, rubber thickness, and the number of steel cord will be mainly studied.

2. Finite Element Model Introduction

2.1. Finite Element Model Material. In the simulation of the conveyor the belt splice, the materialization of the model can be divided into two main parts: steel cord and rubber.

For the selection of the parameters of the steel cord material, we mainly refer to the correlation coefficient of the ST630 conveyor belt and the series of properties of the steel. We set the density $\rho = 7.85 \times 10^{-9}$ Ton/mm³, Poisson's ratio $\mu = 0.29$, and elastic modulus $E = 210$ GPa [16].

Rubber is a polymer material, and its properties are complex. Its properties are usually rather varied and depend on its composition and the contents of special ingredients.

The rubber used to make the conveyor belt is often not made of a rubber material. There are some other materials to change the hardness and strength of the conveyor belt rubber [19]. We set the rubber in the simulation model according to the parameters of the ST630 supplied by the conveyor belt manufacturer. In the many comparisons between simulation and experiment, we found the Mooney–Rivlin model is the best fit [16]. And we obtained the general strain energy function as follows:

$$W = \sum_{i+j=1}^N C_{ij} (I_1 - 3)^i (I_2 - 3)^j + \sum_{k=1}^N \frac{1}{d_k} (I_3 - 1)^{2k}, \quad (1)$$

where C_{ij} are the material constants, I_1 , I_2 , and I_3 are the invariants of the left Cauchy–Green strain tensor, and N is the natural number.

Binomial third-order expansion is

$$W = C_{10} (I_1 - 3) + C_{01} (I_2 - 3) + \frac{1}{D} (J - 1)^2, \quad (2)$$

where C_{01} and C_{02} are the material constants and the strain gradient tensor F determinants J , and D is the material constant related to the bulk modulus [16].

2.2. Failure Unit. In the actual conveyor joint, there is an adhesive layer between the rope and the rubber. The adhesive layer is also critical to the strength of the conveyor splice. In the finite element simulation, we placed a failure layer between the steel cord and the rubber to simulate the adhesive layer in the conveyor belt splice. From Figure 2, we can see the steel cord unit, rubber unit, and failure unit.

3. Numerical Simulation and Experimental Investigations

3.1. Finite Element Model and Experimental Samples. Figures 3(a)–3(d) are finite element models of single steel cord conveyor belt splices with lengths of 50.0, 70.0, 80.0, and 100.0 mm, respectively.

Figures 4(a)–4(d) are the splice samples of experimental single steel cord conveyor belt splices with lengths of 50.0, 70.0, 80.0, and 100.0 mm correspondingly. The coefficient of uniformity of the rubber and steel cord is the standard of the steel cord conveyor belt of ST630.

3.2. Change of Adhesive Layer in Simulation and Experiment.

When the pullout force reaches the maximum value, the steel cord is completely debonded from the rubber. The steel cord and the rubber are in a slip state and separated. As shown in Figure 5(a), it is a steel cord and rubber separated in the simulation. When the pullout force reaches the maximum, the unit fails and is deleted. The force between the steel cord and the rubber is almost zero. As shown in Figure 5(b), in the experiment, the pullout force was maximized and the steel cord was separated from the rubber. By comparing the adhesion layer between the simulation and the experiment, we can find that the changes between the two are relatively close.

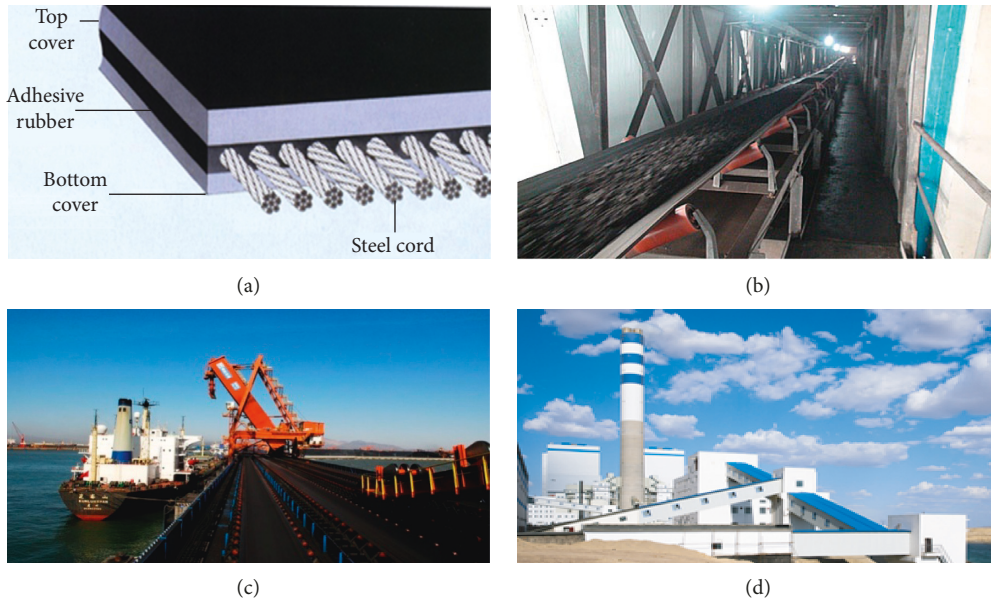


FIGURE 1: (a) Structure of the conveyor belt and application fields of the conveyors: (b) mining, (c) port, and (d) electric power.

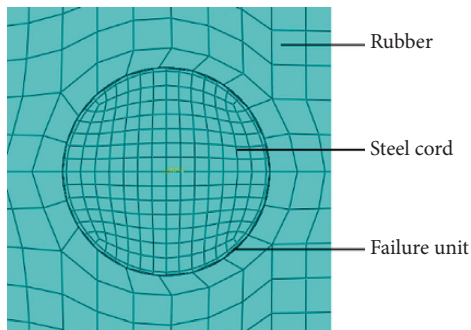


FIGURE 2: Unit settings.

3.3. *Simulation and Experimental Results.* In the simulation, a forced displacement is applied to the steel cord. When the displacement between the steel cord and the rubber changes, the magnitude and variation trends of the pullout force are obtained. In the experiment, we used a universal stretching machine to clamp the ends of the experimental sample. A forced displacement is applied over a section to stretch the sample so that the steel cord draws a different displacement from the rubber. The computer will record the magnitude and trend of the extraction force at different displacements.

In general, both in the simulation and experiment, the displacement between the steel cord and the rubber is changed to obtain the magnitude and variation of the extraction force.

Figure 6(a) shows the varieties of pullout force with time in the numerical simulation, and Figure 6(b) shows the experimental result. We can see that when the length of the steel cord is the same, the trend of the simulation and experimental pullout force is very close.

Table 1 shows the simulation and experimental data of the pullout force. We can know that when the length of steel cord is same, simulation and experimental extraction force results are very similar. So the simulation can be considered successful.

4. Analysis of Conveyor Belt Strength Factors

Different conveyor belt finite element models have been established by using Abaqus/CAE, to study the strength changes of steel cords under different factors. In addition to the above different steel cord length studies, simulations were also done for different steel cord diameters, rubber thickness, and steel cord numbers, and they are varied to study the effect on the strength of the steel cord conveyor belt.

4.1. *Steel Cord Conveyor Belt Length.* In the above simulation experiment, the relationship between the length and strength of steel cord conveyor belts is obtained and is shown in Figure 7.

When the length of the steel cord increases from 50.0 mm to 100.0 mm, the pullout force increases linearly, and the approximate satisfaction of the relation is as follows:

$$F = 4349 + 74.4 \times \nabla l \quad (\nabla l \geq 0), \quad (3)$$

where F is the pullout force and the unit is N and ∇l is the increments of steel cord length and the unit is mm.

4.2. *Steel Cord Diameter.* The effect of steel cord diameter from 2.0 mm to 4.5 mm has been studied numerically and the following conclusions are drawn. The finite element models of steel cord diameter of 2.0, 2.5, 3.0, 3.5, 4.0, and 4.5 mm are shown in Figure 8.

Numerical simulation results are shown in Figure 9. It shows the effect of the different steel cord diameters for the pullout force. When the diameter of the steel cord increases from 2.0 mm to 3.5 mm, the pullout force increases linearly, and the approximate satisfaction of the relation is as follows:

$$F = 2298 + 1943 \times \nabla d \quad (0 \leq \nabla d \leq 1.5), \quad (4)$$

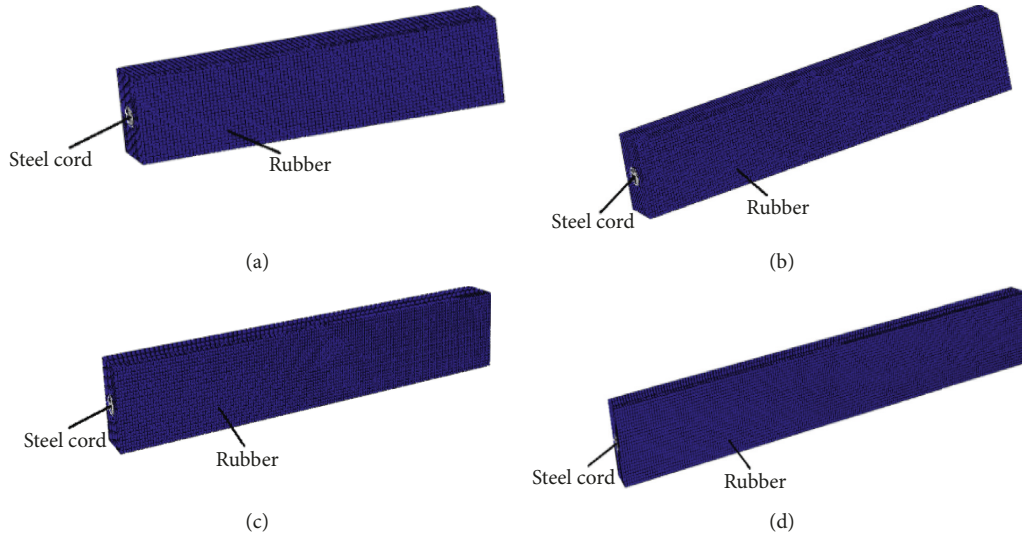


FIGURE 3: Finite element model of the single steel cord conveyor belt: (a) 50.0 mm; (b) 70.0 mm; (c) 80.0 mm; (d) 100.0 mm.

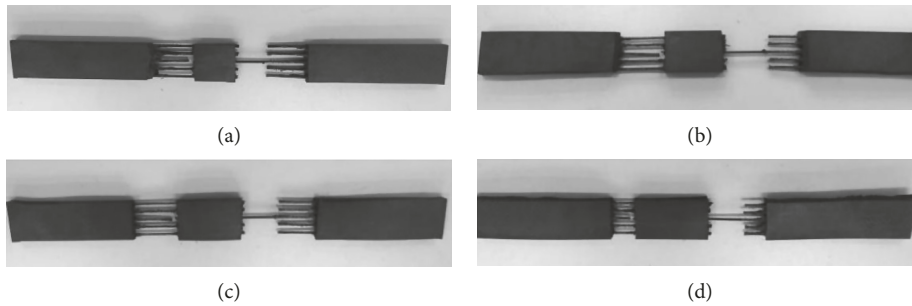


FIGURE 4: Splice samples of experiment. 50.0 mm (a), 70.0 mm (b), 80.0 mm (c), and 100.0 mm (d) single steel cord sample.

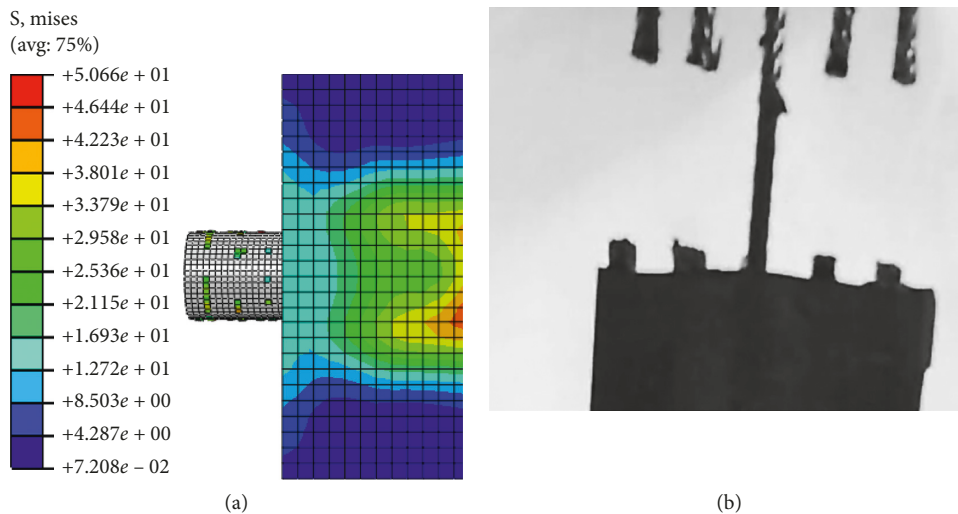


FIGURE 5: Steel cord and rubber separation. (a) Simulation result. (b) Experimental result.

where F is the pullout force and the unit is N and ∇d is the increment of steel cord diameter and the unit is mm.

When the diameter of the steel cord increases from 3.5 mm to 4.5 mm, the pullout force is increasing, but it has

become slow. However, the effect of different steel cord diameters on the strength of conveyor belts is enormous. It is important to guide us to produce the conveyor belt with the required strength.

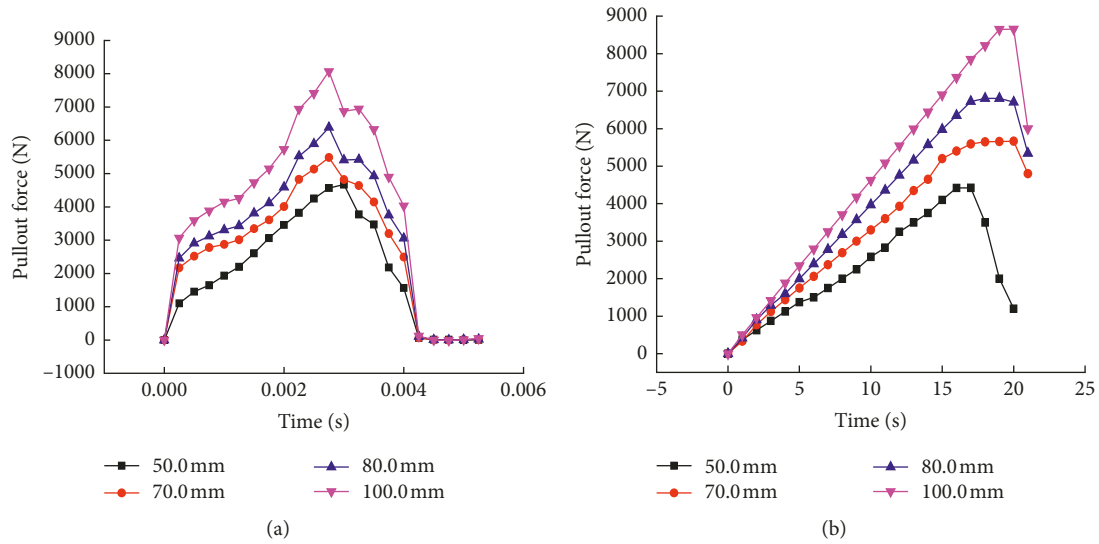


FIGURE 6: Simulation and experimental results. (a) Numerical results. (b) Experimental results.

TABLE 1: Simulation and experimental data.

Length of steel cord (mm)	Numerical value (N)	Experimental value (N)	Relative error (%)
50.0	4669	4422	5.59
70.0	5484	5664	3.18
80.0	6384	6807	6.74
100.0	8067	8652	6.76

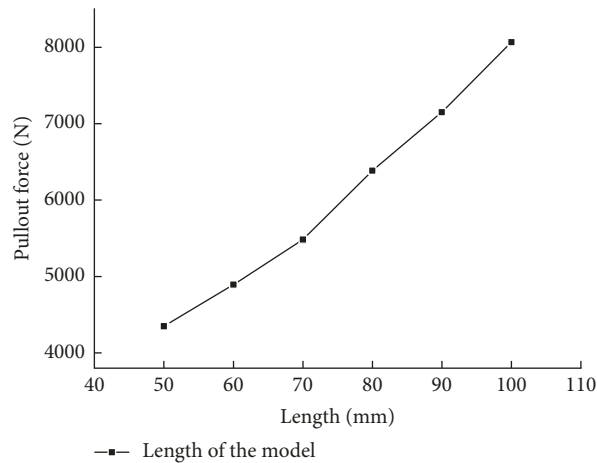


FIGURE 7: The change in pullout force with different lengths.

4.3. *Rubber Thickness.* For studying the effect of rubber thickness on the pullout force, the rubber thickness was considered to be 4.0, 5.0, 5.5, 6.0, 6.5, and 7.0 mm, and the finite element models of the steel cord conveyor belt with the strength specification of ST630 are shown in Figure 10. All the numerical simulation results are shown in Figure 11.

When the rubber thickness is increased from 4.0 mm to 5.0 mm, the pullout force increased 671 N. It can be said that the change is more obvious. However, when the rubber thickness is increased from 5.0 mm to 7.0 mm, the change of the pullout force is quite slow. It can almost be considered

that the force no longer increases. In general, the contribution of rubber to strength of the steel cord conveyor belt is very small compared to the steel cord. It is not feasible to change the strength of the conveyor belt by changing the rubber thickness.

4.4. *Steel Cord Number.* In the above simulations, all of them are single steel cord. In order to further study the strength of the steel cord conveyor belt, we built multiple steel cords. We established a model of steel cord conveyor belts with

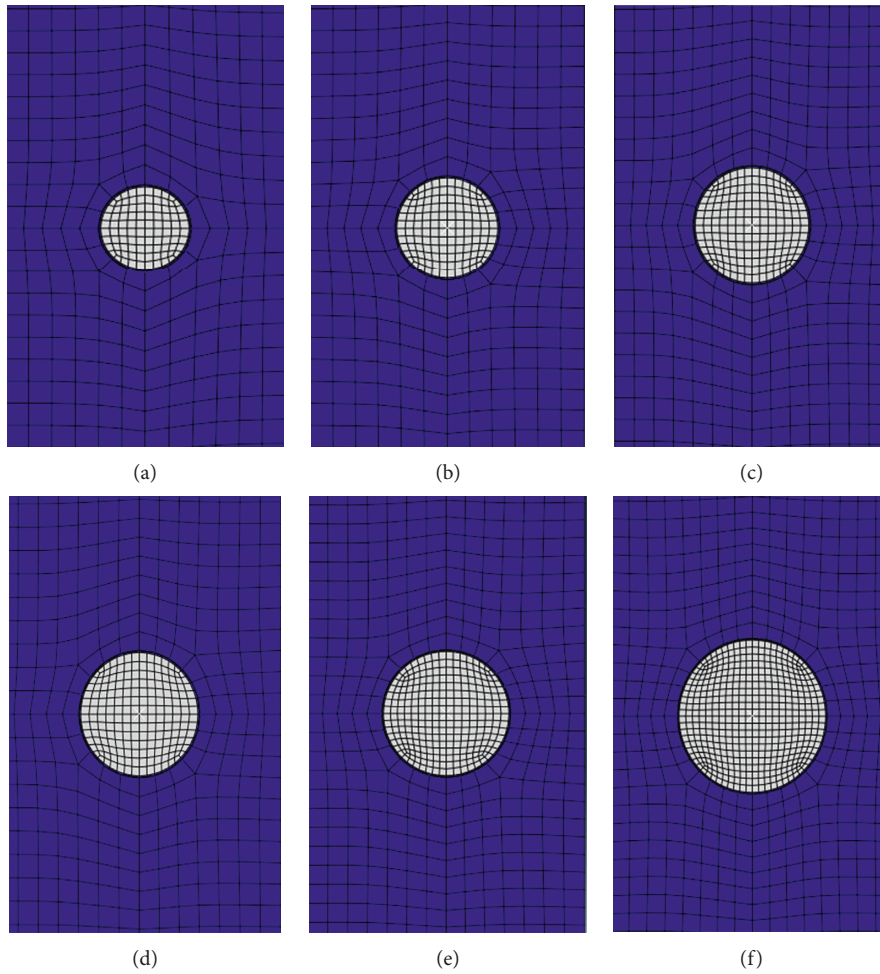


FIGURE 8: Finite element model of different steel cord diameters. (a) 2.0 mm, (b) 2.5 mm, (c) 3.0 mm, (d) 3.5 mm, (e) 4.0 mm, and (f) 4.5 mm.

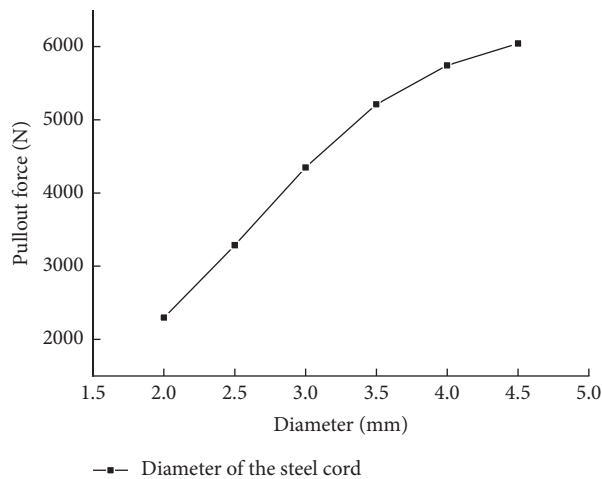


FIGURE 9: The change in pullout force with different steel cord diameters.

different numbers of steel cords and simulated. As shown in Figure 12, there are two and four steel cord conveyor belt models. Simulations were performed on 50.0 mm long models of the single steel cord. The numerical and

experimental pullout force with time for different steel cord numbers is obtained in Figures 13(a) and 13(b), respectively.

When the number of steel cord is increased from one to four, the pullout force also increases. However, compared to

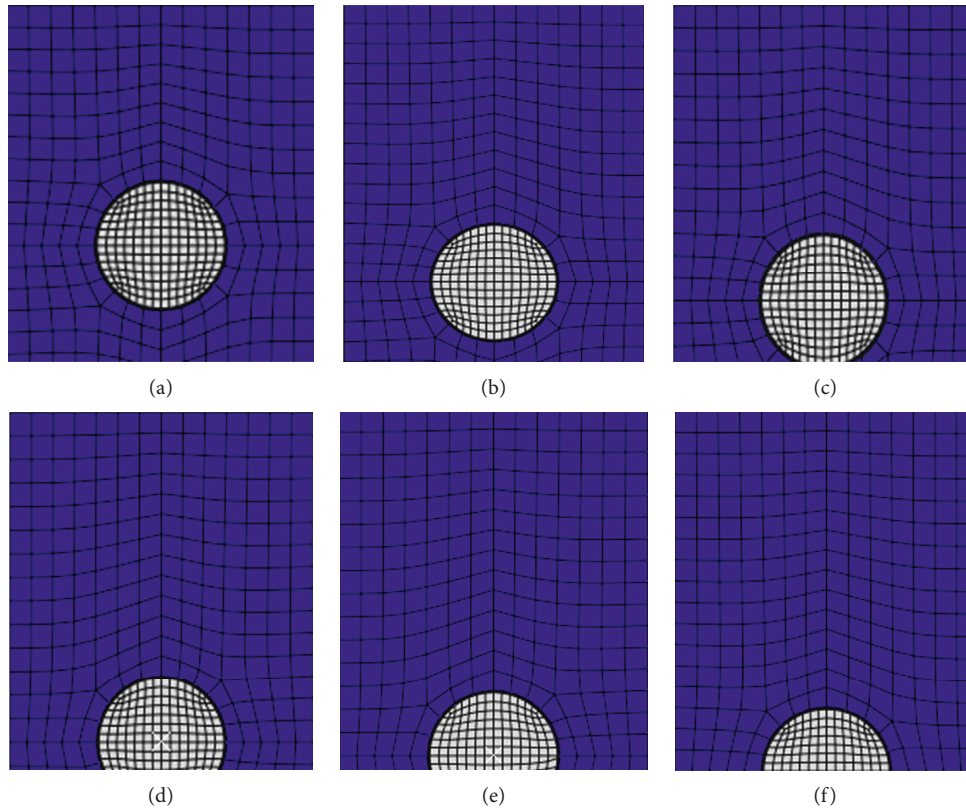


FIGURE 10: Finite element model of different rubber thickness. (a) 4.0 mm, (b) 5.0 mm, (c) 5.5 mm, (d) 6.0 mm, (e) 6.5 mm, and (f) 7.0 mm.

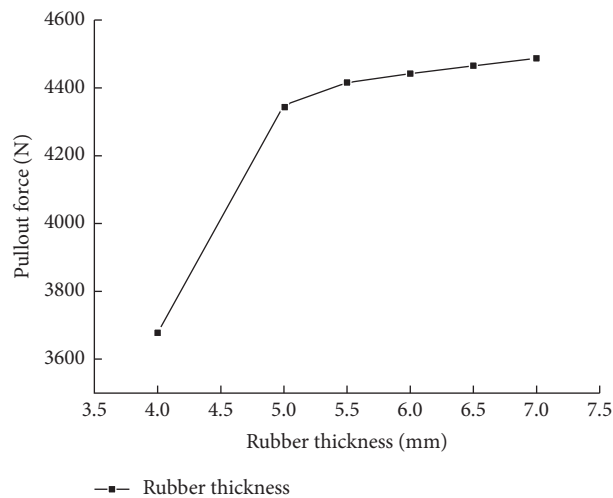


FIGURE 11: The change in pullout force with different rubber thickness.

one and two steel cords, when the number of steel cord is increased, the pullout force is determined to be less than the same length of the single steel cord. The simulation and the experiment have the same conclusion. When we simulated two steel cord models, the force exerted by the two steel cords is reversed, the same as the actual experiment. In the process of pulling out the steel cord, the rubber damage between the two steel cords is quite serious. This leads to reducing the pullout force of the steel cord. In the study of multiple steel cords, the simulation results are in good agreement with the experimental results.

For four steel cords, there are two steel cords on each side. Comparing one and four steel cords is actually a comparison of the pullout force between one steel cord and two steel cords on one side. From the experimental results and simulation results, we can clearly see that increasing the number of steel cords does increase the pullout force of the conveyor belt. However, even if the steel cords are doubled, the increase in pullout force is less than doubled pullout force. In other words, the increase in the number of steel cords does not mean that the tension will increase by the same multiple, and the rate of increase in pullout force is less

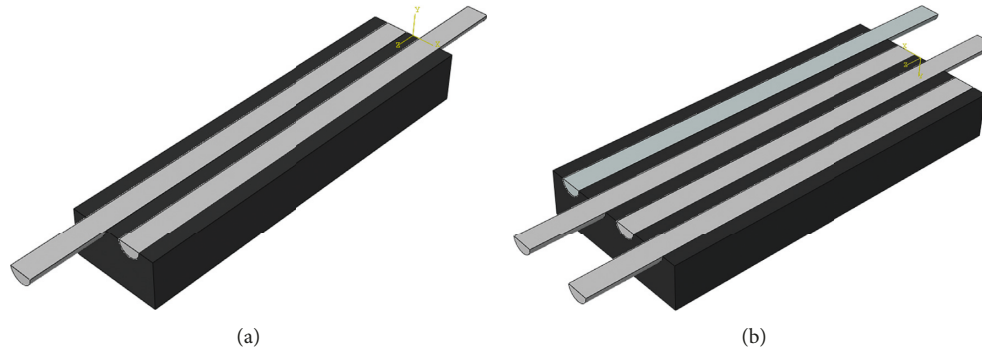


FIGURE 12: Model of the steel cord conveyor belt. (a) Two steel cords. (b) Four steel cords.

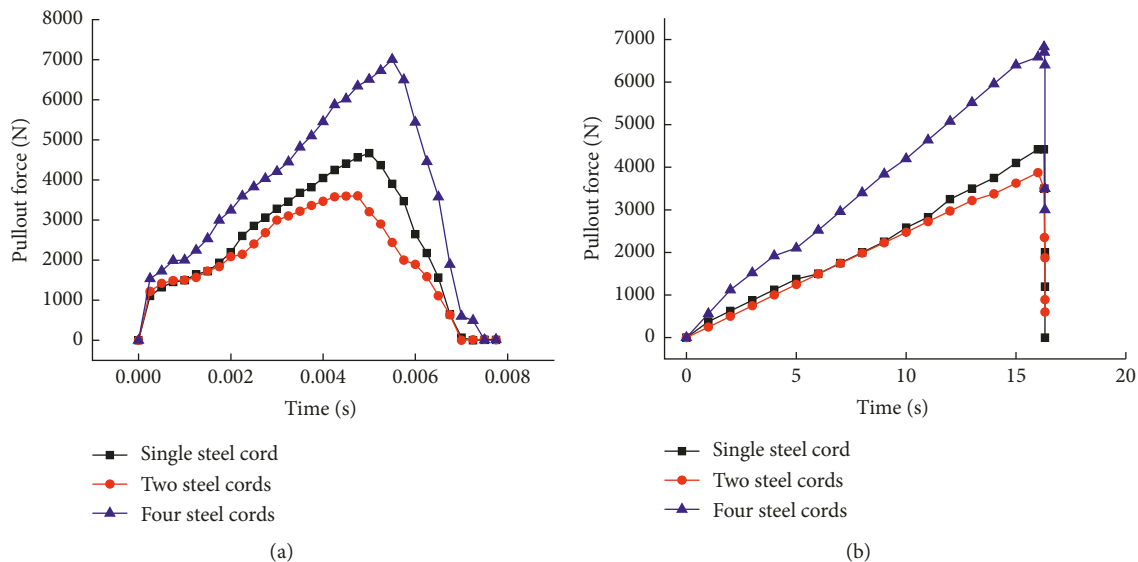


FIGURE 13: The change in pullout force with different steel cord numbers. (a) Numerical results. (b) Experimental results.

than the rate of increase in the number of steel cords. Therefore, we can say that, in practical applications, it is not economical to constantly increase the strength of the conveyor belt by increasing the number of steel cords.

5. Conclusion

There are many factors affecting the strength of the steel cord conveyor belt, such as steel cord length, diameter, rubber thickness, and the number of steel cord. This paper analyses the strength factors of the steel cord conveyor belt based on the FEM. Firstly, we verified the reliability of numerical simulation by comparing experiment and simulation. Then, we simulated the model with different steel cord diameters, rubber thickness, and different number of steel cords, to study the effect on the pullout force of the steel cord conveyor belt. The conveyor belt length, steel cord diameter, rubber thickness, and steel cord number at normal impact were found to have different influences. In the four factors, the effect of rubber thickness is the least noticeable. The diameter of the steel cord and conveyor belt length impact on the steel cord conveyor belt is approximately linear. For the different number of steel cords, the increase in the

number of steel cords does not mean that the tension will increase by the same multiple, and the rate of increase in pullout force is less than the rate of increase in the number of steel cords. The conclusions obtained above provide values for splice strength, which can tell us the influence of different factors and guide us to make conveyor belts of different strengths. In this way, wasting resources can be avoided as well.

Data Availability

The raw/processed data required to reproduce these findings cannot be shared at this time as the data also form part of an ongoing study.

Conflicts of Interest

The authors declare that they have no conflicts of interest.

Acknowledgments

This work was supported by the National Natural Science Foundation of China (51504164), the Key Scientific and

Technological Support Projects of Tianjin Key R&D Program (18YFZCGX00930), the Tianjin Science and Technology Project (18YFJLCG00060), and the Program for Innovative Research Team in University of Tianjin (Grant no. TD13-5034).

References

- [1] D. Marasová, M. Ľ. Ambriško, A. GrinčováAndrejiová, and A. Grincova, "Examination of the process of damaging the top covering layer of a conveyor belt applying the FEM," *Measurement*, vol. 112, pp. 47–52, 2017.
- [2] M. Huang and W. Renzhi, "Real time monitoring techniques and fault diagnosis of mining steel cord belt conveyors," *Journal of China Coal Society*, vol. 30, no. 2, pp. 245–250, 2005.
- [3] D. Mazurkiewicz, "Tests of extendability and strength of adhesive-sealed joints in the context of developing a computer system for monitoring the condition of belt joints during conveyor operation," *Eksploatacja I Niezawodność—Maintenance and Reliability*, vol. 47, no. 3, pp. 34–39, 2010.
- [4] D. Mazurkiewicz, "Analysis of the ageing impact on the strength of the adhesive sealed joints of conveyor belts," *Journal of Materials Processing Technology*, vol. 208, no. 1–3, pp. 477–485, 2008.
- [5] A. Harrison, "A new technique for measuring loss of adhesion in conveyor belt splices," *Australian Journal of Coal Mining Technology and Research*, vol. 4, pp. 27–34, 1983.
- [6] Melco Mining Supplies, "Method and device for monitoring and inspecting a conveyor belt," DE 3517314(A1) 1986-02, Melco Mining Supplies, Melco Mining Supplies, Germiston, South Africa, 1986.
- [7] Phoenix Conveyor Belt System Co., "A device for nondestructive testing of conveyor belts," CN 20058004178 8.X 2008-05, Phoenix Conveyor Belt System Co., Phoenix Conveyor Belt System Co., Chennai, India, 2005.
- [8] X. Li, C. Miao, Y. Zhang, and W. Wang, "Automatic fault detection for steel cord conveyor belt based on statistical features," *Journal of China Coal Society*, vol. 37, no. 7, pp. 1233–1238, 2012.
- [9] G. Fedorko, V. Molnar, D. Marasova et al., "Failure analysis of belt conveyor damage caused by the falling material. Part II: application of computer metrotomography," *Engineering Failure Analysis*, vol. 34, pp. 431–442, 2013.
- [10] D. Mazurkiewicz, "Maintenance of belt conveyors using an expert system based on fuzzy logic," *Archives of Civil and Mechanical Engineering*, vol. 15, no. 2, pp. 412–418, 2015.
- [11] M. Bajda and M. Hardygóra, "The influence of natural ageing processes on the strength parameters of steel cord conveyor belts," *International Journal of Mining, Reclamation and Environment*, vol. 32, no. 6, pp. 430–439, 2018.
- [12] L. Chen, P. Ma, C. Wang, Z. Sun, and D. Dang, "Finite element analysis of dynamic fatigue of a new steel cord conveyor belt (HHE) single steel wire," *China Rubber*, vol. 12, pp. 46–48, 2014.
- [13] D. Mazurkiewicz, "Problems of numerical simulation of stress and strain in the area of the adhesive-bonded joint of a conveyor belt," *Archives of Civil and Mechanical Engineering*, vol. 9, no. 2, pp. 75–91, 2009.
- [14] V. Taraba, D. Marasová, D. Kubala, and V. Semjon, "Mathematical modelling of the process of conveyor belt damage caused by the impact stress," *Applied Mechanics and Materials*, vol. 683, pp. 153–158, 2014.
- [15] W. Du, B. Ma, D. Cao, and Z. Xie, "Research on stress and fatigue life of steel wire rope," *Coal Engineering*, vol. 49, no. 8, pp. 134–137, 2017.
- [16] X. Li, X. Long, H. Jiang, and H. Long, "Influence of different cord pitch on the pullout force of steel cord conveyor belt splice," *Journal of Adhesion Science and Technology*, vol. 32, no. 20, pp. 2268–2281, 2018.
- [17] X. Long, X. Li, and H. Long, "Analysis of influence of multiple steel cords on splice strength," *Journal of Adhesion Science and Technology*, vol. 32, no. 24, pp. 2753–2763, 2018.
- [18] X. G. Long, X. Y. Long, H. Q. Jiang, and H. B. Long, "Finite element simulation and experimental verification of steel cord extraction of steel cord conveyor belt splice," *IOP Conference Series: Materials Science and Engineering*, vol. 369, Article ID 012025, 2018.
- [19] Y. Li, R. Sa, C. Shi, J. Wu, Y. Sun, and M. Tian, "Study on joint strength of kevlar rubber conveyor belt," *China Rubber Industry*, vol. 62, no. 12, pp. 713–719, 2015.

Research Article

Hot Deformation Behavior and Microstructural Evolution of Twin-Roll-Casting Mg Alloy during High-Temperature Compression

Qingshan Yang ^{1,2}, Jiahong Dai,³ Sensen Chai,¹ Daliang Yu,¹ Bin Jiang,² and Fusheng Pan²

¹School of Metallurgy and Material Engineering, Chongqing University of Science and Technology, Chongqing 401331, China

²National Engineering Research Center for Magnesium Alloy, Chongqing University, Chongqing 400044, China

³College of Materials Science and Engineering, Yangtze Normal University, Chongqing 408100, China

Correspondence should be addressed to Qingshan Yang; qsyang@cqu.edu.cn

Received 18 July 2019; Accepted 27 November 2019; Published 18 December 2019

Guest Editor: Benjamin I. Imasogie

Copyright © 2019 Qingshan Yang et al. This is an open access article distributed under the Creative Commons Attribution License, which permits unrestricted use, distribution, and reproduction in any medium, provided the original work is properly cited.

The deformation behavior and microstructural evolution of twin-roll-casting AZ31 Mg alloy sheets were investigated via hot compression tests at 0°, 5°, and 10° from the normal direction. Compression strains of 5%, 15%, 25%, and 35% were employed at high temperatures of 450°C and 500°C. The flow stress as well as the difference in the flow stress associated with different sampling directions decreased when the temperature was increased. Furthermore, the volume fraction of dynamically recrystallized grains increased with increasing deformation, whereas the average grain size decreased. The DRX grain size and the volume fraction of dynamically recrystallized grains increased with increasing deformation temperature. During ultrahigh temperature compression, the effect of sampling direction on the compression microstructure is relatively small.

1. Introduction

Magnesium (Mg) alloys, as the lightest structural alloys, have received increasing attention and have been extensively applied in various transportation systems [1–3]. However, the inherently poor workability of these alloys hinders their use in further engineering applications, owing mainly to the limited number of slip systems operating at room temperature [4–6]. Thus, the automotive applications of Mg alloys are limited mainly to die castings. Wrought products such as sheet and bar have been developed with the aim of broadening the application range of these alloys. In addition, the sheet should be readily formable into complex shapes. Mg alloys are more workable at elevated temperatures than at room temperature, owing to the activation of slip systems other than the basal slip system [7–9]. Hence, the hot forming of Mg alloys has been extensively explored.

The formability of Mg alloys can be increased through different fabrication processes, which mainly rely on the hot

deformation methods. Mg-Al-Zn alloy, as the most widely used Mg alloys, has been extensively studied. Previous studies have shown that Mg alloys might undergo dynamic recrystallization (DRX) during hot working processes. J. C. Tan and M. J. Tan [10] evaluated the dominance of continuous recrystallization phenomena in the AZ31 alloy exposed to temperatures of 250–400°C. They reported that due to the rapid grain growth, negligible grain refinement occurs during high-temperature DRX. Maximum grain refinement occurred at medium temperatures. Sitdikov and Kaibyshev suggested a temperature- and strain-dependency regime for the grain size variation [11]. Barnett reported that the dynamically recrystallized grains of Mg alloys are less sensitive to deformation conditions than those of other metals [12].

A twin-roll-casting (TRC) process combines casting and hot rolling into a single process, which would provide a means of producing Mg strip products at competitive costs for commercial applications [13, 14]. However, reported studies of the associated twin-roll-casting and hot compression (HC)

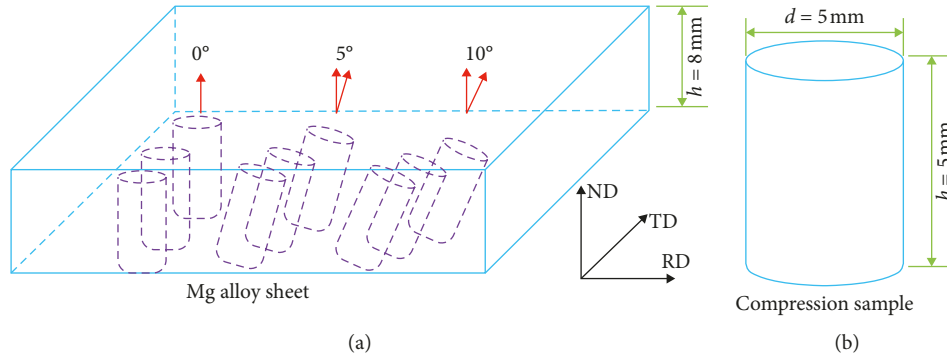


FIGURE 1: (a) Schematic showing the sampling directions. (b) Size of samples subjected to high-temperature compression.

processing of Mg alloys are rare. Therefore, in this work, the hot deformation behavior and microstructural evolution of twin-roll-cast AZ31 alloy were investigated via hot compression at 450°C and 500°C. The effect of different original sampling directions and different accumulated plastic deformations on the high-temperature deformation mechanism of the alloy was explored.

2. Experimental Procedure

An 8-mm-thick twin-roll-casting (TRC) AZ31 alloy (Mg-3 Al-1 Zn, in wt.%) was investigated in this work. Cylindrical hot compression testing specimens were machined to a size of $\Phi 5 \times H 5$ mm. In preparation for the compression tests, cylindrical samples were cut from the TRC-AZ31 sheet at 0°, 5°, and 10° to the normal direction (ND), as shown in Figure 1.

To investigate the effects of high temperatures and accumulated plastic deformation, isothermal hot compression tests were performed at 450°C and 500°C for deformations ranging from 5% to 35% in steps of 10%. During the tests, specimens were heated (heating rate: 10°C/s) to the deformation temperature and held isothermally for 240 s. The specimens were then subjected to a hot compression test (strain rate: 0.15 s^{-1}) on a Gleeble1500D machine. After hot deformation, the samples were water cooled to obtain the deformed microstructures.

After quenching in water, the deformed specimens were sectioned in the center parallel to the compression axis, and the microstructure was observed via optical microscopy (OM). To further investigate the occurrence of dynamic recrystallization (DRX) during high-temperature compression, the microstructures were examined after various deformation strains. The volume fraction of dynamically recrystallized grains was determined through a point counting technique. The DRX grains were almost readily distinguishable from the pre-existing grains, and the corresponding grain size was determined using an imaging analysis system.

3. Results and Discussion

3.1. Flow Stress Behavior. Figure 2 shows the true stress-strain curves for different deformations ranging from 5% to 35% under a strain rate of 0.15 s^{-1} at 450°C. No steady state

was observed for the 0° and 5° samples subjected to a low deformation of 5%. A flow-stress steady state was observed when the deformation increased to 15%, 25%, and 35%. Most samples exhibited an almost steady-state flow behavior, and work hardening was restricted to very small strains (<0.05) followed by mild flow softening, leading to a steady-state flow. The temperature-dependent flow behavior observed for Mg alloys was attributed to the activation of nonbasal slip systems at elevated temperatures. Chapuis and Liu reported that increasing the plastic deformation temperature of Mg alloys can result in high strain rate sensitivity, and secondary slip modes can be easily activated [15]. The true stress values of TRC-AZ31 with different sampling directions and different accumulated plastic deformations during the steady stage at 450°C are listed in Table 1. For the same deformation, the steady-state stress increased with the sampling direction. The difference in the flow stress associated with different sampling directions is attributed to the grain orientation of the twin-roll-cast AZ31 sheet alloy. Furthermore, the variation in the steady-state stress between different sampling directions decreased with increasing deformation, from 6 MPa at 15% deformation to 2 MPa at 35% deformation. Therefore, large strain and more complete recrystallization induced by hot deformation can improve the anisotropy of the twin-roll-cast AZ31 sheet alloy.

Figure 3 shows the true stress-strain curves obtained under the same deformation conditions at 500°C. It can be seen that each sample reached a steady state. The true stress values of TRC-AZ31 with different sampling directions and different accumulated plastic deformations during the steady stage at 500°C are summarized in Table 2. It can be observed that the steady-state stress decreased with increasing temperature, from an average of 35 MPa at 450°C to 28 MPa at 500°C. However, for a given deformation at 450°C, the steady-state stress increased with the sampling direction, which differed from the trends observed for deformation at 500°C. This may have resulted from the fact that as the temperature increases, activation of the nonbasal slip, such as prismatic $\langle a \rangle$ and pyramidal plane slip $\langle c+a \rangle$, is facilitated [16].

3.2. Microstructural Evolution. Figure 4 shows the initial longitudinal microstructure of the as-received TRC-AZ31

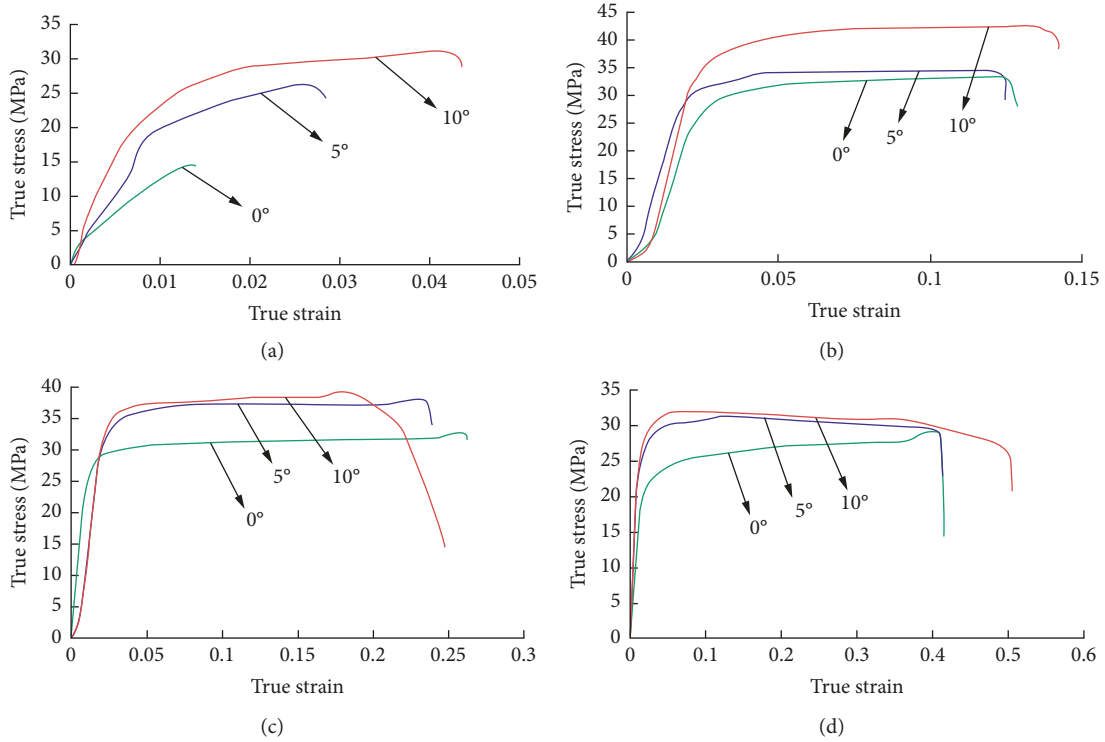


FIGURE 2: True stress-true strain curves of the TRC-AZ31 alloy during hot compression at 450°C: (a) 5% strain; (b) 15% strain; (c) 25% strain; (d) 35% strain.

TABLE 1: True stress (MPa) of the TRC-AZ31 alloy during the stable stage at 450°C.

Strain (%)	Sampling direction		
	0°	5°	10°
5	—	—	26
15	28	34	40
25	29	36	37
35	29	31	33

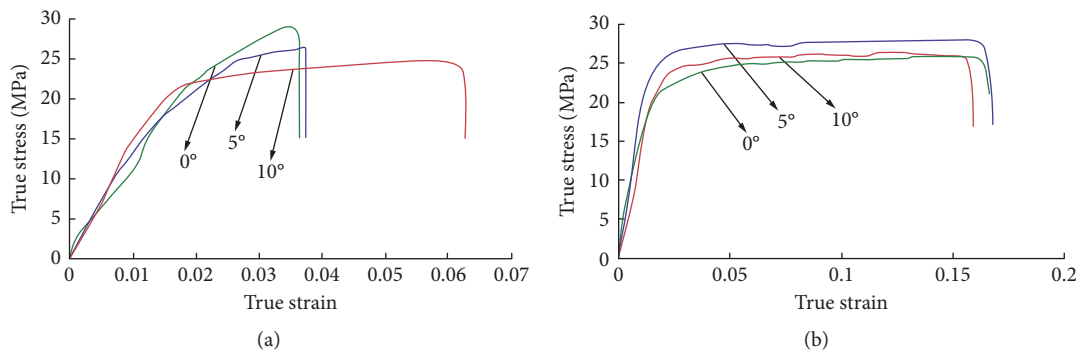


FIGURE 3: Continued.

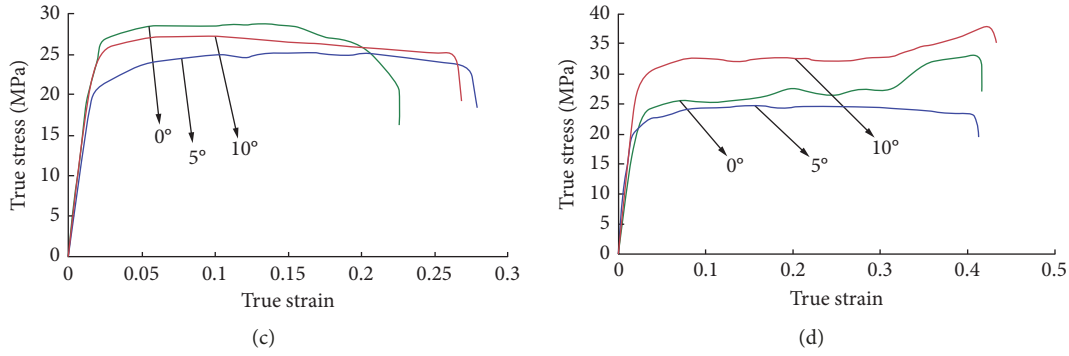


FIGURE 3: True stress-true strain curves of the TRC-AZ31 alloy during hot compression at 500°C: (a) 5% strain; (b) 15% strain; (c) 25% strain; (d) 35% strain.

TABLE 2: True stress (MPa) of the TRC-AZ31 alloy during the stable stage at 500°C.

Strain (%)	Sampling direction		
	0°	5°	10°
5	29	26	24
15	25	27	26
25	28	25	27
35	27	24	33

alloy. It can be observed that it consisted of dendritic columnar grains. Due to the high cooling rate and directional heat transfer during the TRC processes, large columnar grains have grown against the heat extraction direction, where the solidifying material has been in contact with the cold casting rolls.

Figure 5 reveals the microstructure after deformation at 450°C and strains ranging from 5% to 35% for sampling directions of 0°, 5°, and 10°. In general, the dynamic recrystallization process is classified into continuous and discontinuous DRX [17]. Continuous recrystallization is considered a recovery process accompanied by a progressive increase in boundary misorientation and the conversion of low-angle boundaries into high-angle boundaries [18]. This type of recrystallization may be accompanied by gradual softening in the flow curve, resulting in a plateau in the true stress-true strain curves. As shown in Figure 5, for the 0° sample with 5% strain, the necklace DRX grains are concentrated on grain boundaries due to the occurrence of nonbasal slip at high temperatures of 450°C. This indicated DRX behavior depended on the temperature-dependent deformation mode. At 450°C and mainly low strains, microscopic strain localization at slip lines resulted in the formation of bulges at the grain boundaries, thereby leading to nucleation of DRX grains. At moderate and high strains, DRX occurred via nucleation in slip bands, and in both cases, rapid dislocation climb led to the formation of low-angle boundaries [19]. Moving dislocations are trapped by these sub-boundaries and are gradually converted into true high-angle boundaries. The results obtained for the AZ31 samples with 5° and 15° directions are similar to those obtained for the 0° direction. High-temperature compression may be accompanied by dislocation annihilation and

grain boundary migration. Moreover, grain rotation is easily activated at high temperature.

Figure 6 shows the microstructural evolution of the as-compressed samples at 500°C. The nucleation of DRX grains is similar to that of 450°C compression. For the higher temperature, the degree of DRX was larger than the compression at 450°C, which resulted in growth of the grains. Figure 7 shows the volume fraction of dynamically recrystallized grains (DRX-G). It was determined to quantify the effect of deformation temperature and the degree of deformation on the microstructure after high-temperature compression. It can be seen that the volume fraction of DRX-G increased with increasing level of deformation. This is typical of nucleation and growth type of transformations. During high-temperature compression, dislocation climb leads to the formation of low-angle boundaries. When the strain increases, moving dislocations are trapped by these sub-boundaries and are gradually converted into true high-angle boundaries. The volume fraction and size of dynamically recrystallized grains at 500°C were higher than the fraction and size associated with 450°C and the same deformation conditions. During hot compression, work hardening occurred in the newly formed recrystallized grains, and the size of these grains became limited as the driving force for further growth was reduced. As the temperature decreased, the level of work hardening increased, and the growth of the new grains was limited, thereby leading to a reduction in the DRX grain size. As shown in Figures 5 and 6, at low strain levels, the average grain size decreased with increasing strain. Once the dynamically recrystallized grains were established, the DRX grain size changed only slightly with increasing strain.

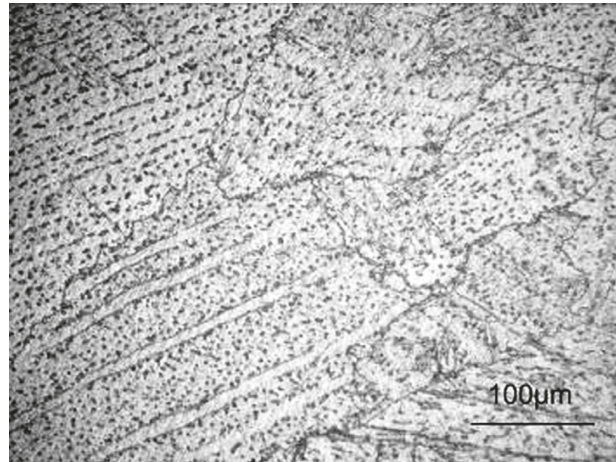


FIGURE 4: Optical micrograph of the TRC-AZ31 sheet alloy in the longitudinal orientation.

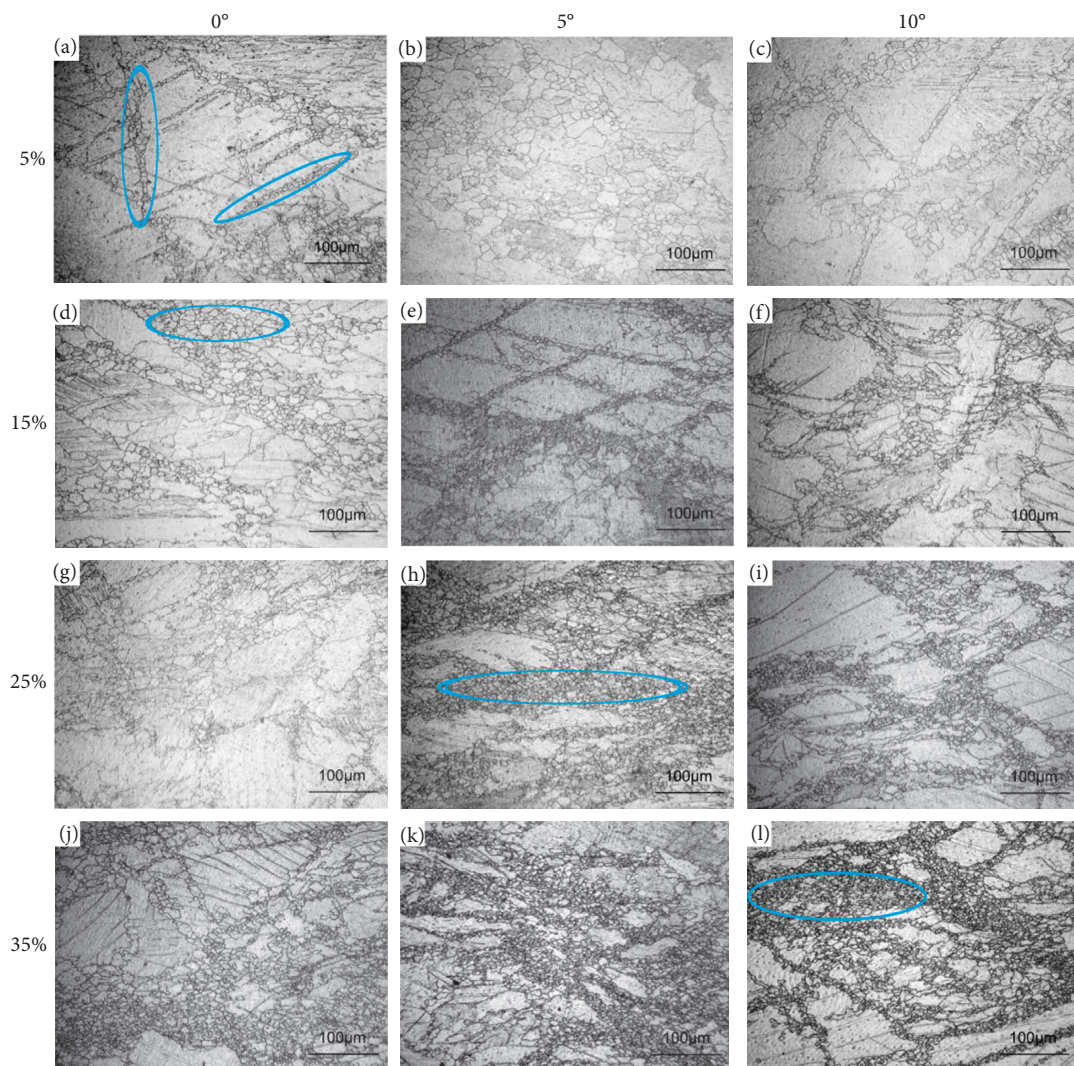


FIGURE 5: Microstructures of the twin-roll-cast (TRC) AZ31 alloy with different original sampling directions and different deformations under 450°C compression: (a) 0°-5%; (b) 5°-5%; (c) 10°-5%; (d) 0°-15%; (e) 5°-15%; (f) 10°-15%; (g) 0°-25%; (h) 5°-25%; (i) 10°-25%; (j) 0°-35%; (k) 5°-35%; (l) 10°-35%.

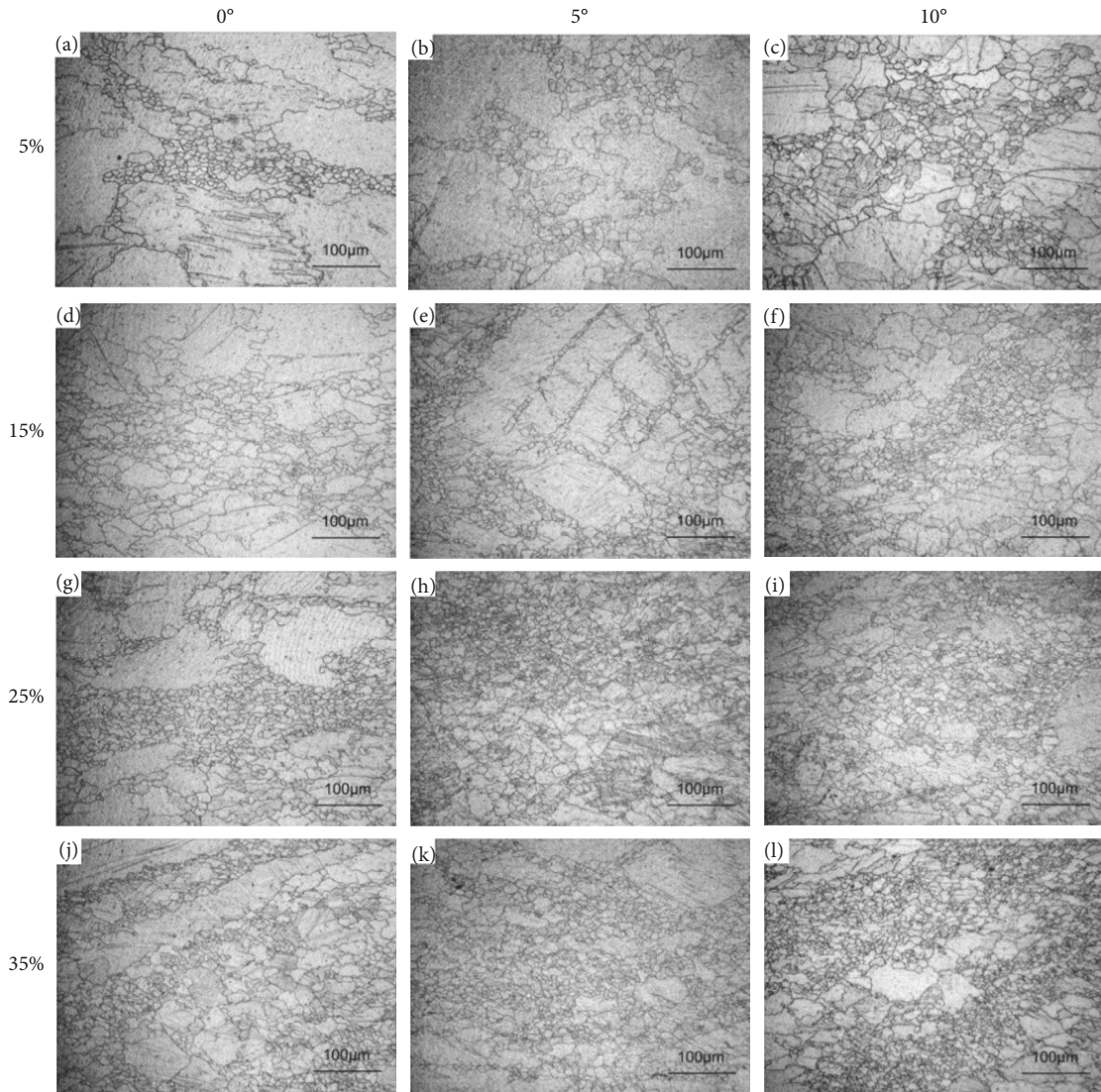


FIGURE 6: Microstructures of the twin-roll-cast (TRC) AZ31 alloy with different original sampling directions and different deformations at 500°C compression: (a) 0°-5%; (b) 5°-5%; (c) 10°-5%; (d) 0°-15%; (e) 5°-15%; (f) 10°-15%; (g) 0°-25%; (h) 5°-25%; (i) 10°-25%; (j) 0°-35%; (k) 5°-35%; (l) 10°-35%.

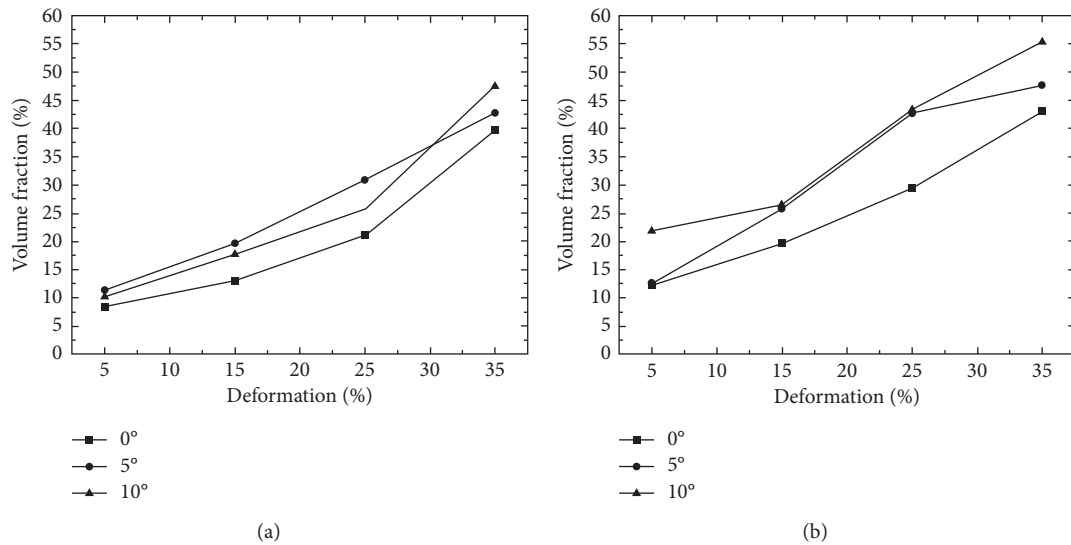


FIGURE 7: Volume fraction of dynamically recrystallized grains after hot deformation: (a) 450°C; (b) 500°C.

4. Conclusions

The hot deformation behavior and microstructural evolution were investigated for twin-roll-cast AZ31 alloys subjected to compression strains at high temperatures and different sampling directions. In our present work, the conclusions can be mainly drawn as follows:

- (1) The results revealed that the flow stress decreases with increasing temperature, from an average of 35 MPa at 450°C to 28 MPa at 500°C
- (2) The anisotropy of the flow stress associated with different sampling directions decreased with increasing temperature
- (3) The volume fraction and grain size of the dynamically recrystallized grains increased when the deformation temperature increased from 450°C to 500°C

Data Availability

All data included in this study are available upon request by contact with the corresponding author.

Conflicts of Interest

The authors declare that they have no conflicts of interest.

Acknowledgments

The authors are grateful for the financial supports from the National Natural Science Foundation of China (51701033 and 11847077), Chongqing Science and Technology Commission (cstc2018jcyjAX0022 and cstc2017jcyjAX0216), and Chongqing Municipal Education Commission (KJQN201901504, KJ1713336, and KJQN201801523).

References

- [1] J. Zhang, S. Liu, R. Wu, L. Hou, and M. Zhang, "Recent developments in high-strength Mg-RE-based alloys: focusing on Mg-Gd and Mg-Y systems," *Journal of Magnesium and Alloys*, vol. 6, no. 3, pp. 277–291, 2018.
- [2] T. Nakata, J. J. Bhattacharyya, S. R. Agnew, and S. Kamado, "Unexpected influence of prismatic plate-shaped precipitates on strengths and yield anisotropy in an extruded Mg-0.3Ca-1.0In-0.1Al-0.2Mn (at.%) alloy," *Scripta Materialia*, vol. 169, pp. 70–75, 2019.
- [3] W. Liu, B. Jiang, J. T. QingshanYang, B. Liu, and F. Pan, "Effect of Ce addition on hot tearing behavior of AZ91 alloy," *Progress in Natural Science: Materials International*, vol. 29, no. 4, pp. 453–456, 2019.
- [4] H. Pan, C. Yang, Y. Yang et al., "Ultra-fine grain size and exceptionally high strength in dilute Mg-Ca alloys achieved by conventional one-step extrusion," *Materials Letters*, vol. 237, pp. 65–68, 2019.
- [5] J. H. Kim, B.-C. Suh, T. T. T. Trang, Ji H. Hwang, and N. J. Kim, "Orientations of dynamically recrystallized grains nucleated at double twins in Mg-4Zn-1Sn alloy," *Scripta Materialia*, vol. 170, pp. 11–15, 2019.
- [6] Q. Yang, Q. Dai, C. Lou et al., "Twinning, grain orientation, and texture variations in Mg alloy processed by pre-rolling," *Progress in Natural Science: Materials International*, vol. 29, no. 2, pp. 231–236, 2019.
- [7] L. Wang, Z. Zhang, M. Cao et al., "Enhanced stretch formability of magnesium alloy sheet by prestretching at various speeds at higher temperature," *JOM*, vol. 71, no. 5, pp. 1705–1713, 2019.
- [8] K. Wang, J. Wang, P. Xing et al., "Microstructure and mechanical properties of Mg-Gd-Y-Zn-Mn alloy sheets processed by large-strain high-efficiency rolling," *Materials Science and Engineering: A*, vol. 748, pp. 100–107, 2019.
- [9] Q. Yang, H. Dong, J. Zhang, B. Jiang, and F. Pan, "Influence of pre-rolling on microstructural evolution of non-basal textured magnesium alloy," *International Journal of Materials Research*, vol. 110, no. 9, pp. 892–895, 2019.
- [10] J. C. Tan and M. J. Tan, "Dynamic continuous recrystallization characteristics in two stage deformation of Mg-3Al-1Zn alloy sheet," *Materials Science and Engineering A*, vol. 339, no. 1-2, pp. 124–132, 2003.
- [11] O. Sitdikov and R. Kaibyshev, "Dynamic recrystallization in pure magnesium," *Materials Transactions*, vol. 42, no. 9, pp. 1928–1937, 2001.
- [12] M. R. Barnett, "Hot working microstructure map for magnesium AZ31," *Materials Science Forum*, vol. 426–432, no. 6, pp. 515–520, 2003.
- [13] B. Jiang, W. Liu, Q. Dong, M.-X. Zhang, and F. Pan, "Grain refinement of Ca addition in a twin-roll-cast Mg-3Al-1Zn alloy," *Materials Chemistry and Physics*, vol. 133, no. 2-3, pp. 611–616, 2012.
- [14] T. T. T. Trang, J. H. Zhang, J. H. Kim et al., "Designing a magnesium alloy with high strength and high formability," *Nature Communications*, vol. 9, no. 1, Article ID 2522, 2018.
- [15] A. Chapuis and Q. Liu, "Modeling strain rate sensitivity and high temperature deformation of Mg-3Al-1Zn alloy," *Journal of Magnesium and Alloys*, vol. 7, no. 3, pp. 433–443, 2019.
- [16] B. Jiang, W. Liu, S. Chen, Q. Yang, and F. Pan, "Mechanical properties and microstructure of as-extruded AZ31 Mg alloy at high temperatures," *Materials Science and Engineering: A*, vol. 530, pp. 51–56, 2011.
- [17] W. J. Kim and T. J. Lee, "Two different types of deformation behaviors in ultrafine grained Mg alloys at high temperatures and development of the generalized constitutive equation for describing their deformation behavior," *Materials Science and Engineering: A*, vol. 613, pp. 264–273, 2014.
- [18] F. Wang, R. Zheng, J. Chen et al., "Significant improvement in the strength of Mg-Al-Zn-Ca-Mn extruded alloy by tailoring the initial microstructure," *Vacuum*, vol. 161, pp. 429–433, 2019.
- [19] A. Sankaran, S. Vadakke Madam, A. Nouri, and M. R. Barnett, "Attaining high compressive strains in pure Mg at room temperature by encasing with pure Al," *Scripta Materialia*, vol. 66, no. 10, pp. 725–728, 2012.

Research Article

Brazeability, Microstructure, and Joint Characteristics of $ZrO_2/Ti-6Al-4V$ Brazed by Ag-Cu-Ti Filler Reinforced with Cerium Oxide Nanoparticles

Ashutosh Sharma  and Byungmin Ahn 

Department of Materials Science and Engineering and Department of Energy Systems Research, Ajou University, Suwon 16499, Republic of Korea

Correspondence should be addressed to Byungmin Ahn; byungmin@ajou.ac.kr

Received 30 July 2019; Revised 11 October 2019; Accepted 5 November 2019; Published 12 December 2019

Guest Editor: Rezwanul Haque

Copyright © 2019 Ashutosh Sharma and Byungmin Ahn. This is an open access article distributed under the Creative Commons Attribution License, which permits unrestricted use, distribution, and reproduction in any medium, provided the original work is properly cited.

In this work, we have attempted to develop the Ag-Cu-Ti filler for bonding ZrO_2 to Ti-6Al-4V. The CeO_2 nanoparticles were reinforced in the eutectic Ag-Cu-Ti filler via mechanical mixing and melting route. Furthermore, the brazeability, microstructure, and mechanical behavior, as well as brazing performance of the $ZrO_2/Ti-6Al-4V$ joints, were assessed. The wettability of the Ag-Cu-Ti matrix was increased from 89 to 98% on Ti-6Al-4V and from 83 to 89% on the ZrO_2 substrate after the addition of 0.05% CeO_2 . Also, there was a depression in the melting point of the composite fillers up to 3°C. The microstructure consists of Cu- and Ag-rich phases and Cu-Ti intermetallic compounds (IMCs). The joint shear strength was improved with the addition of CeO_2 up to 0.05 wt.% in the matrix. It was inferred that, for an excellent brazing performance of the $ZrO_2/Ti-6Al-4V$ joint, the optimum amount of CeO_2 should be 0.05 wt.% in the Ag-Cu-Ti matrix.

1. Introduction

Bonding of ceramic materials to metals is a recent hot topic in various engineering applications, including heat exchangers, connectors, capacitors, thermoelectrics, solar cells, and complex structural joints [1, 2]. It is always a practical challenge to bond these ceramic materials directly due to a wide difference in physicochemical and mechanical properties of ceramics and metals that imposes a great challenge in microjoining operations [2]. For this purpose, various popular brazing fillers are already developed where the most popular ones are eutectic Ag-Cu or Ag-Cu-Ti alloys as reported in the past [3, 4]. However, with regard to complex geometry, the thickness of IMCs, and cost, each filler is unique and has limitations of its own [5]. In such case, the selection of a superior filler metal is required for high reliability of brazed ceramic joints. If we inspect previous literatures, we see two major issues that are needed to be minimized in ceramic brazing, such as wetting of the contact

surfaces and the stress development caused by the mismatch in mechanical and thermal properties of two contact materials that depend on the deformation characteristics of the filler used [1–5].

There are various strategies developed to resolve these mentioned issues. First is the use of active metal brazing techniques. Active metal brazing is a simple and cost-effective approach where active elements like Ti or Zr as wetting promoters are used between the contact surfaces for bonding [1, 6]. Therefore, the popular Ag-Cu-Ti filler seems to be more reliable over the Ag-Cu filler due to its good wetting to most of the ceramics [7].

Second is the use of additive elements or reinforcement particles to refine the interfacial layer, redistribute the stress in the matrix, and relax the joint stress. These secondary phases act as a wetting enhancer when used in optimum amounts [8, 9]. It was reported that the use of reinforcements provides outstanding benefits in terms of joint strength and interfacial characteristics [10, 11]. In the

past, the use of nanomaterials has already been suggested as a potential technology for controlling the wetting, refining the grains, IMCs, as well as to tailor the joint microstructure [8–11]. In lead-free soldering, a variety of nanoparticles have found a wide scope in popular Sn-based alloys for tailoring the microstructure containing harmful Cu_6Sn_5 and Cu_3Sn IMCs across the Cu-Sn interface [12–14]. Analogous to brazing, nanoparticles have been tried in few studies related to the low-temperature Al-brazing filler and remarkably improved wetting and joint performance are obtained. Al-brazing fillers have been embedded with SiC, La_2O_3 , and ZrO_2 successfully in low-temperature Al-brazing [11]. There are various studies in the past where researchers have used metal or nonmetallic additives to control the brazing performance. More recently, Shin and his coworkers have improved the wetting and brazing property of $\text{Al}_2\text{O}_3/\text{Cu}$ joints with the addition of Sn in the Ag-Cu-Ti alloy during the brazing process [3]. Halbig and his coworkers used SiC particles in the Ag-Cu-Ti matrix for SiC brazing [15]. Miao et al. used graphite particles to improve the performance of metal-bonded high-speed grinding wheels [16]. Zhao et al. used MoS_2 particles to enhance tribological properties of cubic boron nitride abrasive composites [17]. In another study, Miao et al. recommended that TiX additives in the Ag-Cu-Ti matrix (TiB_2 , TiN, and TiC) improve the shear strength of the brazed joints [18]. Most popular nanoreinforcements used regularly to reinforce a metal alloy include Al_2O_3 , SiC, ZrO_2 , SnO_2 , CeO_2 , La_2O_3 , and ZrSiO_4 [14, 15, 19–23]. However, in ceramic brazing, limited studies exist on nanocomposite-based brazing fillers [24–26]. Among these nanoreinforcements, rare earth oxide, particularly, CeO_2 , has been used frequently for low temperature joining of electronic devices as well as in multiple applications such as photonics, energy storage devices, sensing, and power electronics.

In view of these merits, we have chosen CeO_2 nanoparticles produced via solution combustion method to reinforce the Ag-Cu-Ti matrix and apply for brazing of ZrO_2 and Ti-6Al-4V plates in the lap-joint configuration. The microstructural, mechanical, and thermal properties of the composite fillers were studied. The effect of various fractions of CeO_2 ($x=0, 0.03, 0.05, \text{ and } 0.1 \text{ wt\%}$) in the Ag-Cu-Ti matrix was studied for microstructure, wetting and brazed joint ZrO_2 , and Ti-6Al-4V strength.

2. Materials and Methods

2.1. Synthesis of CeO_2 Powder. Cerium oxide nanopowder was prepared by using the high-temperature solution combustion method using ceric ammonium nitrate, citric acid, and glycine [27]. All the chemicals were of reagent grade supplied by Sigma Aldrich, USA.

2.2. Base Materials. The base materials used for brazing were ZrO_2 and Ti-6Al-4V (Grade 5, ELI plate) rectangular plates obtained from Acucera, Inc., South Korea, and United Performance, USA, respectively. Both the base materials

were diced by using a diamond saw into slices with a size of $60.0 \text{ mm} \times 15.0 \text{ mm} \times 2.0 \text{ mm}$ for brazing and shear testing.

2.3. Synthesis of Composite. Four different types of composite fillers with different CeO_2 contents were used in the experiment, as shown in Table 1. The powder mixtures were blended in a planetary mill (Planetary Ball Mill PM 400 Retsch, Germany) at 300 rpm for 24 hours (ball to powder weight ratio = 15:1). After milling, the mixed powder samples were mixed with Nocolok flux (10:1 ratio) and melted at $1050^\circ\text{C}/30$ minutes in a tube furnace.

2.4. Brazeability. The brazeability of the composite fillers was determined from the spreading ratios of filler melted before and after melting (Figure 1).

The solidified composite filler (0.3 g approx.) was mixed with Nocolok flux (10:1 ratio) and placed over the substrate ($30 \text{ mm} \times 30 \text{ mm} \times 2 \text{ mm}$) at 920°C . After a gap of 30 s, the filler was melted completely over the substrate. The spreading ratio (S) was estimated from the difference in the spread ratios before and after experiment [28].

2.5. Melting Point. The effect of CeO_2 nanoparticles on the melting behavior of composite fillers was studied by using differential scanning calorimeter (DSC) apparatus (NETZSCH STA 449 F1). About 6–8 mg of specimens were heated in Al_2O_3 pans from 28 to 1000°C at a heating rate of $10^\circ\text{C}/\text{minute}$ under the Ar atmosphere to minimize air oxidation.

2.6. Joint Fabrication. The composite filler was rolled down to a thickness of 0.25 mm and then applied between ZrO_2 and Ti-6Al-4V alloy in a lap-joint structure. The whole assembly was brazed at 980°C for 10 min in a vacuum furnace at 5×10^{-6} Torr, as shown in the lap-joint structure in Figure 2.

2.7. Microstructure. The phase evolution and structure were determined by using X-ray diffractometer (XRD) from Bruker's D8 Advance, Germany, at operating parameters of 40 mA and 40 kV and copper target ($\lambda = 0.154 \text{ nm}$). The surface morphology of the developed composite fillers and joint cross section were examined in a field emission scanning electron microscope (FE-SEM, Hitachi, Japan). To observe the distinct features of the interface, the joint cross section was etched by using an aqueous solution of FeCl_3 , H_2O , HCl, and $\text{C}_2\text{H}_5\text{OH}$. The compositional analyses of the IMCs and phases were done by using the EDS detector attached to the FE-SEM.

2.8. Filler Microhardness. Microhardness of the developed composite fillers was measured by using a Vickers' microhardness tester (VMHT-6, Leica). The testing parameters include an applied load of 25 gf for a dwell time of 20 s, respectively. The microhardness was automatically calculated and displayed over the display panel of the machine.

TABLE 1: Composition of various composite fillers used.

Serial no.	Filler matrix	Reinforcement nanoceria (x in wt.%)	Sample ID
1		$x = 0$	Ag-Cu-Ti
2	Ag-28Cu-2Ti	$x = 0.03$	Ag-Cu-Ti-0.03 CeO ₂
3		$x = 0.05$	Ag-Cu-Ti-0.05 CeO ₂
4		$x = 0.1$	Ag-Cu-Ti-0.1 CeO ₂



FIGURE 1: Schematic diagram for the measurement of brazeability.

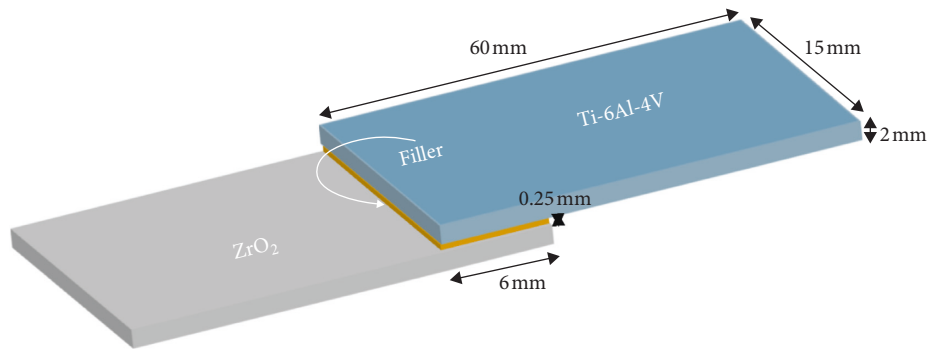


FIGURE 2: Schematic diagram for brazed joint fabrication.

2.9. *Brazing Joint Performance: Shear Test.* The shear strength of the joint was estimated according to the JIS Z 3192 standard [29]. The testing was done by employing a universal testing machine (5 ton UTM, DUT-30000 CM, DK Eng., Korea) at a crosshead speed of 3 mm/minute. The schematic of the set-up used for the shear test is shown in Figure 3.

3. Results and Discussion

3.1. *Reinforcement.* Figure 4(a) shows the XRD pattern of the CeO₂ powder (according to ICDD#00-034-0394) obtained after solution combustion synthesis [30]. The peak broadening indicates the nanocrystallinity of the powder with an increased lattice strain. The average crystallite size (D) of the powder particles is given by the Scherer equation [27]:

$$D = \frac{0.9\lambda}{B \cos \theta} \quad (1)$$

In general, the XRD peak broadening is governed by various factors such as the instrumental effects, crystallite size, and lattice strain. Here, λ is the wavelength of X-rays, θ is the Bragg angle, and B is the line broadening at full-width half-maximum intensity calculated from the broadening of a

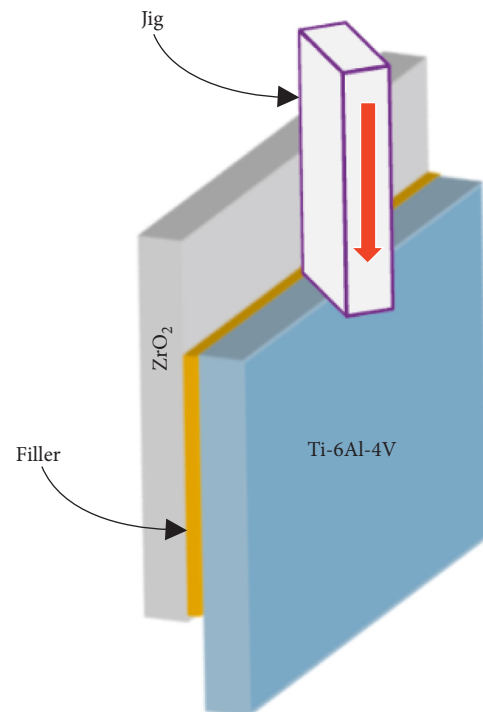


FIGURE 3: Schematic diagram for the shear test.

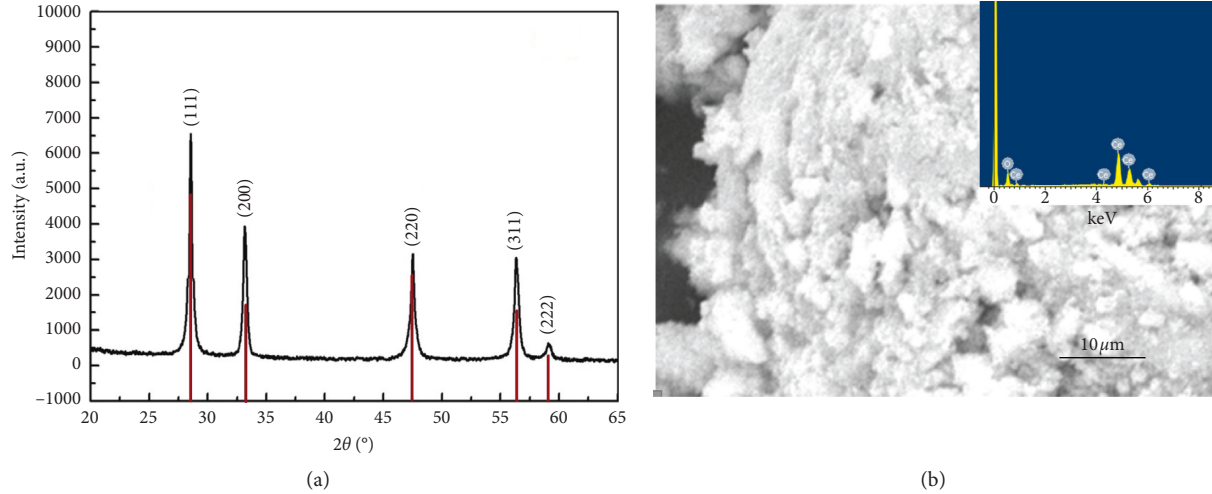


FIGURE 4: (a) XRD pattern (according to ICDD#00-034-0394) and (b) morphology of the ceria nanoparticles. The inset shows the EDS analysis of produced ceria nanopowder.

standard stress-free sample and instrumental broadening contributions, given by

$$B = \sqrt{B_{\text{standard}}^2 - B_{\text{instrumental}}^2} \quad (2)$$

The contribution to lattice strain is given by a modified Scherer equation:

$$B \cos \theta = \frac{0.9\lambda}{D} + \varepsilon \sin \theta. \quad (3)$$

The crystallite size D can be calculated from the peaks in the XRD pattern, and the average value of lattice strain was determined from the intercept at $\cos \theta = 0$ and the slope of $B \cos \theta$ versus $\sin \theta$.

The crystallite size was found to lie in the range of 20–30 nm with the average lattice strain of CeO_2 powder around 0.39. It is to be noted that as the particle size reduces, the number of surface atoms increases as compared to the bulk. This increase in the surface atoms per unit volume raises the lattice strain which is associated with the structural distortion. This results in high reactivity of the particles at nanoscale level.

The morphology of the CeO_2 powder particles (Figure 4(b)) is like loose spongy type which is a typical morphology obtained for combustion synthesized powder [27]. This type of structure is already observed in the past by several researchers. The EDS analysis in the inset of Figure 4(b) confirms the composition of the CeO_2 powder nanopowder.

3.2. Composite Phase and Microstructure. Figure 5 shows the XRD pattern of $\text{Ag-Cu-Ti-}x\text{CeO}_2$ composite fillers. The results indicated various peaks in the XRD spectrum. The phases detected were Ag (ICDD# 01-071-3752), Cu (ICDD#00-004-0836), Cu_2Ti (ICDD# 00-020-0371), and Cu_4Ti (ICDD# 00-020-0370) diffraction peaks [30]. The X-ray patterns of other samples were almost similar. There was no indication of the formation of new phases related to CeO_2 which indicated that there is no reaction of the filler matrix with the reinforcement particles (Figure 5(a)). The CeO_2 particles were not present in the XRD spectrum which

could be attributed to a very low amount of CeO_2 nanoparticles to be detected by the XRD analysis.

The different morphology of the composite fillers is shown in Figures 5(b)–5(e). We can see that the addition of CeO_2 nanoparticles has a great effect on the filler morphology. The corresponding phases were analyzed by the EDS, as shown in Figures 5(b)–5(d) and 5(f). The bright and dark phases are shown by spots 1 and 2, while Cu-Ti IMCs are distributed across the interface (spot 3), as shown in Figure 5(f). The EDS analysis results given in Table 2 also show the probable compositions of the phases of spots 1–3.

After the addition of CeO_2 nanoparticles, the Ag- and Cu-rich regions were found to be smaller up to the addition of 0.03 wt% CeO_2 . In other words, there is a refinement in the microstructure of the filler alloy. Generally, the morphology of the composite filler is refined by the addition of nanoparticles into the filler matrix. There are various theories proposed in the past that explain the effect of nanoparticles on composite morphology. According to the absorption theory of surface-active materials [8–11], addition of nanoparticles decreases the surface-free energy of the crystal plane where maximum adsorption of nanoparticle occurs. More precisely, the amount of adsorption of nanoparticles per unit area of j th plane is given by the following equation:

$$\Gamma^j = -\frac{C}{RT} \left(\frac{d\gamma^j}{dC} \right), \quad (4)$$

where RT represents the thermal energy/mole, C is the concentration of nanoparticles, and γ^j represents the surface energy/area of the j th plane before the adsorption of nanoparticles. After integration of equation (4), we get

$$\gamma_C^j = \gamma_0^j - RT \int_0^C \frac{\Gamma^j}{C} dC, \quad (5)$$

where γ_C^j represents surface energy/area of j th plane after adsorption of nanoparticles and γ_0^j is the surface energy/area of the j th plane before adsorption. The resultant surface energy is given from equation (5):

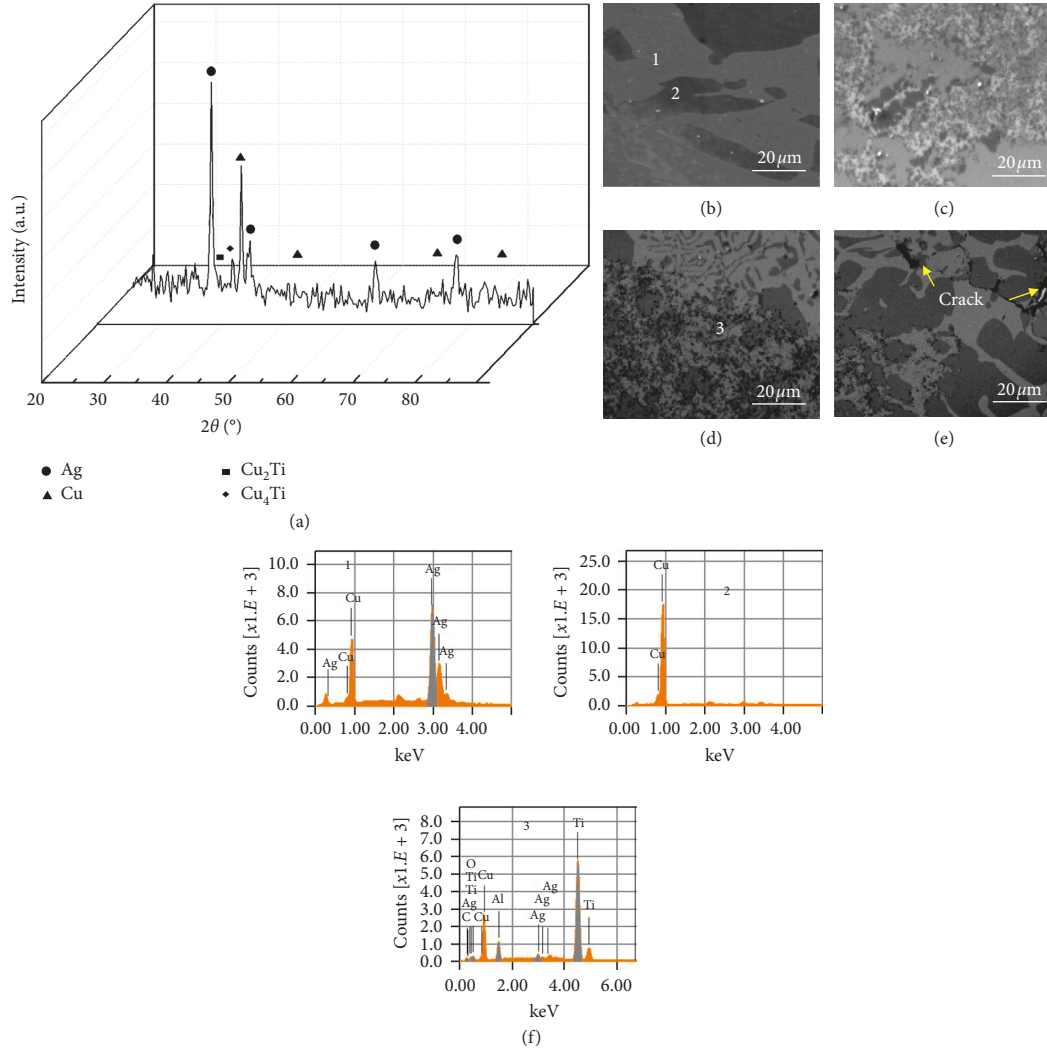


FIGURE 5: (a) XRD pattern of Ag-Cu-Ti- x CeO₂ ($x=0.1$ wt%) and (b–e) morphology of the Ag-Cu-Ti- x CeO₂ filler, $x=0, 0.03, 0.05,$ and 0.1 wt%. (f) EDS analysis of different phases in (b) and (d).

TABLE 2: EDS data of different phases in Figures 5(b)–5(d).

Serial no.	Sample ID	Cu (at.%)	Ag (at.%)	Ti (at.%)	Phase
1	Point 1	36.41	63.59		Ag-Cu
2	Point 2	100.00	0		Cu
3	Point 3	31.72	1.48	66.8	Cu ₂ Ti

$$\sum_j A_k \gamma_k^j = \sum_j \left(\gamma_0^j - RT \int_0^C \frac{\Gamma^j}{C} dC \right) A_k, \quad (6)$$

where A_j represents the surface area of j th plane and $\sum_j A_k \gamma_0^j$ is independent of concentration. Therefore, surface energy will be minimum when $RT \int_0^C \Gamma^j / C dC$ is maximized [8–13]. Thus, the growth velocity of a particular plane, j , will be decreased. Since the size of CeO₂ is around 20–30 nm, the size of the IMCs is of the order of several micrometers. As a result, the nanoparticles can be adsorbed easily to the IMC plane and restrict their growth.

Another theory for the effect of nanoparticles on morphology says that nanoparticles act as nucleating agents, and,

therefore they increase more nucleation sites in the matrix as well as on the IMCs during solidification [8–13]. Therefore, according to the aforementioned theories, the presence of an optimum amount of nanoparticles into the filler matrix will promote the grain and IMC refinement of the filler.

However, for $x=0.1$ wt%, the filler microstructure shows the presence of a few cracks (Figure 5(e)). This may be due to the high amount of CeO₂ nanoparticles getting segregated in due course, and localized cracking was noticed [9–11]. It has been reported by many researchers that high surface-active nanoparticles have a tendency of agglomeration. When the nanoparticle content increases in the matrix ($x \geq 0.05$ wt%), the interparticle distance among them decreases and they tend to segregate in the matrix. This localized segregation results in buildup of porosity and cracks may form in the joint after solidification [11–13].

3.3. Brazeability. Wettability of Ag-Cu-Ti- x CeO₂ filler on the ZrO₂ and Ti-6Al-4V substrates is shown in Figure 6. It

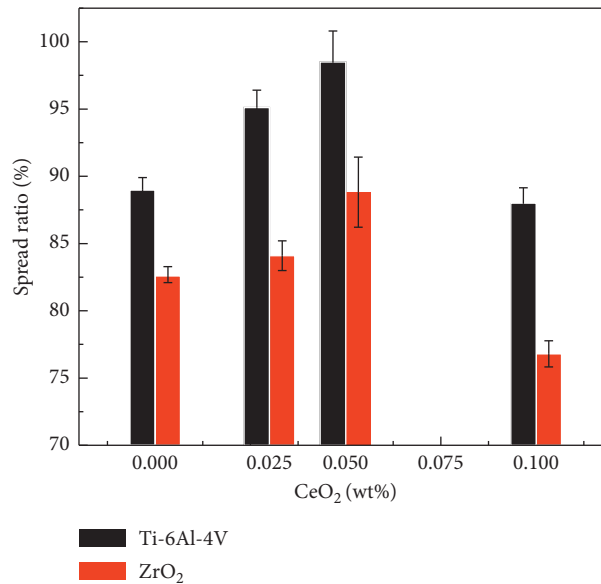


FIGURE 6: Spreading ratio of various Ag-Cu-Ti- x CeO₂ composites on Ti-6Al-4V and ZrO₂ substrates.

was observed that the spreading ratio rises continuously with the increase in CeO₂ fraction in the filler. When the content of CeO₂ was more than 0.05 wt%, the spreading ratio drops considerably and the spreadability of composite filler was decreased. The spreading ratio of the pure Ag-Cu-Ti was approximately 89% on Ti-6Al-4V and 83% on zirconia, which approached to a maximum of 98% on Ti-6Al-4V and 89% on zirconia. The spread ratio though decreased severely with the further addition of CeO₂ nanoparticles reaching up to 87% on Ti-6Al-4V but only 76% on zirconia side. This can be correlated with the presence of high surface energy ceria nanoparticles which depress the surface tension of the filler and enhance the wetting [20]. However, at a high amount of ceria nanoparticles in the matrix, the viscosity of the filler increases and therefore wetting decreases instead of the presence of the active Ti element [20].

It is also noted that, in spite of a higher spreading ratio on Ti-6Al-4V, it decreased up to some extent on zirconia substrates. This is obvious due to the presence of strong covalent bonding in zirconia ceramics compared to the metallic ones in metal. It can be concluded that the addition of an optimum amount of CeO₂ nanoparticles (0.05 wt%) enhances the spreading well on both zirconia as well as Ti-6Al-4V substrates.

3.4. Melting Point. Figure 7 represents DSC curves of the produced composite fillers Ag-Cu-Ti- x CeO₂. Only one sharp melting peak is noticed. The melting point of Ag falls near 961.8°C. The phase diagram of Ag-Cu shows the melting point of Ag-Cu lying near 779°C. Although Ti and CeO₂ components are present, the onset melting point lies around the eutectic melting point 781–778°C. The melting point of Ag-Cu-Ti- x CeO₂ fillers is slightly higher but falls within the normal working limits of brazing. The various onset melting points and peak melting temperature of the composite fillers are shown in Table 3.

The filler alloy ($x=0$) has a peak melting point at 786.5°C which changes to 784.8°C and 783.1°C for composite fillers with $x=0.03$ CeO₂ and $x=0.05$ CeO₂. The difference between the onset melting point (solidus) and peak melting (liquidus), the so-called pasty range, is very narrow (<10°C). A narrow pasty range has been reported to benefit the joining process as it avoids the defects like porosity and/or hot tear that occurs during thermal fluctuations [20, 21]. In other words, the change in the melting point of Ag-Cu-Ti- x CeO₂ composites is not high enough to bring any change in service temperature conditions.

3.5. Microstructure of the ZrO₂/Ti-6Al-4V Joint. Figures 8(a)–8(d) show the SEM image of the ZrO₂/Ti-6Al-4V interface brazed at 980°C. The interface zone is composed of several black and white patches. The interfacial elements were identified by the EDS analysis (Figure 8(e)). The spot 1 shows a fine layer near the Ti-6Al-4V side. The white and black phases (spots 2 and 3) correspond to the Ag- and Cu-rich phases. The at.% of Cu/Ti ratios were about 1:2 (23.95%: 51.16%) at spot 1a and 1:4 (14.26%: 49.34%) at spot 1b, respectively. This indicates the IMCs are composed of Cu₂Ti + Cu₄Ti. Also, Ag (79.37%) and Cu (84.28%) were mainly detected in spot 2 (white color) and 3 (black color).

Ti was prominent near the interface as shown although it existed a little across the interface. A thick layer of Cu₂Ti is present near the Ti-6Al-4V which is related to the diffusion of Ti from Ti-6Al-4V and Cu from the filler metal to form an excellent bond [4]. The IMC thicknesses of Ag-Cu-Ti filler ($x=0$ and 0.03) are 18.5 and 22.8 μm. The IMC thickness for $x=0.03$ is higher as compared to $x=0$. The reason can be a very small amount which is not sufficient enough to minimize the IMCs considerably in the matrix. The thickness of this layer is different for each condition being minimum (12.4 μm) at $x=0.05$. Also, the thickness of the interfacial

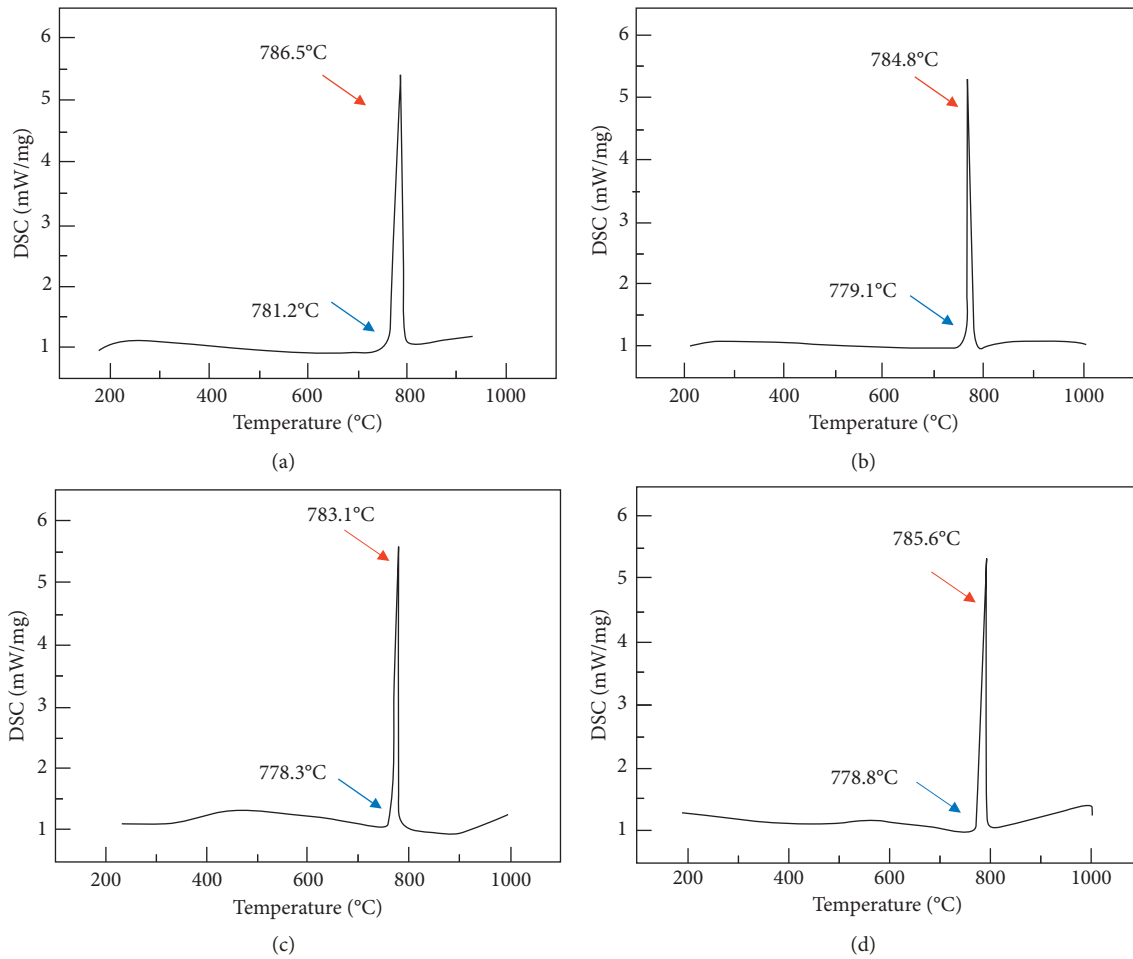


FIGURE 7: Melting point behavior of various Ag-Cu-Ti- x CeO₂ composites: (a) $x=0$; (b) $x=0.03$; (c) $x=0.05$; (d) $x=0.1$.

TABLE 3: Various temperatures obtained from the melting curve of fillers.

Serial no.	Sample ID	$T_{\text{onset m.p.}} (^{\circ}\text{C})$	$T_{\text{peak}} (^{\circ}\text{C})$
1	Ag-Cu-Ti	781.2	786.5
2	Ag-Cu-Ti-0.03 CeO ₂	779.1	784.8
3	Ag-Cu-Ti-0.05 CeO ₂	778.3	783.1
4	Ag-Cu-Ti-0.1 CeO ₂	778.8	785.6

layer is on a little higher side ($15.4\ \mu\text{m}$) for $x=0.1$ compared to $12.4\ \mu\text{m}$ ($x=0.05$) (Figures 8(c) and 8(d)). This might be due to a higher thickness of Cu₄Ti along with Cu₂Ti IMCs at the interface which weakens the bonding. The mechanism of joint formation can be understood by the model presented in Figure 9.

The reaction proceeds in various steps. During brazing, when the temperature is above the solidus of the filler, various elements diffuse to each other across the interface (Figures 9(a) and 9(b)). The filler melts, and then Ti is dissolved into the molten filler and interacts with Cu atoms. Ag occupies the solid solution matrix of the filler. The Cu-Ti IMCs nucleate at the boundaries (Figure 9(c)). The IMC form and grow in due course simultaneously between titanium and ZrO₂. ZrO₂ is bonded under the influence of Ti

which is absorbed in the surface pores through capillary action at the ZrO₂ surface (Figures 9(c)–9(d)). The CeO₂ nanoparticles are attached to the IMCs and prevent their further growth, as shown by thickness measured from the joint SEM in previous section.

3.6. Microhardness. The microhardness values of Ag-Cu-Ti- x CeO₂ composite fillers are given in Table 4. It is seen that the microhardness increases from 115.1 to 126.6 Hv when the CeO₂ content in the filler matrix rises from 0 to 0.05 wt%. This shows a reasonable increase in hardness (11.5%) of the filler matrix. This increase in microhardness value can be ascribed to the fine microstructure containing finer IMCs and Cu- and Ag-rich phases in the Ag-Cu-Ti matrix [31, 32]. The presence of an optimum amount of harder CeO₂ (0.05 wt%) particles in the matrix results in the hindrance of localized plastic deformation of the matrix when CeO₂ particles are present.

A further decrease in hardness (112.5 Hv) is also noticed when 0.1 wt% CeO₂ is added into the filler matrix. Generally, at a high concentration of nanoparticles, the sample hardness should be higher. However, due to high surface energy of CeO₂ nanoparticles, their mixing in the filler powder is not uniform and their incorporation is poor in the solidified

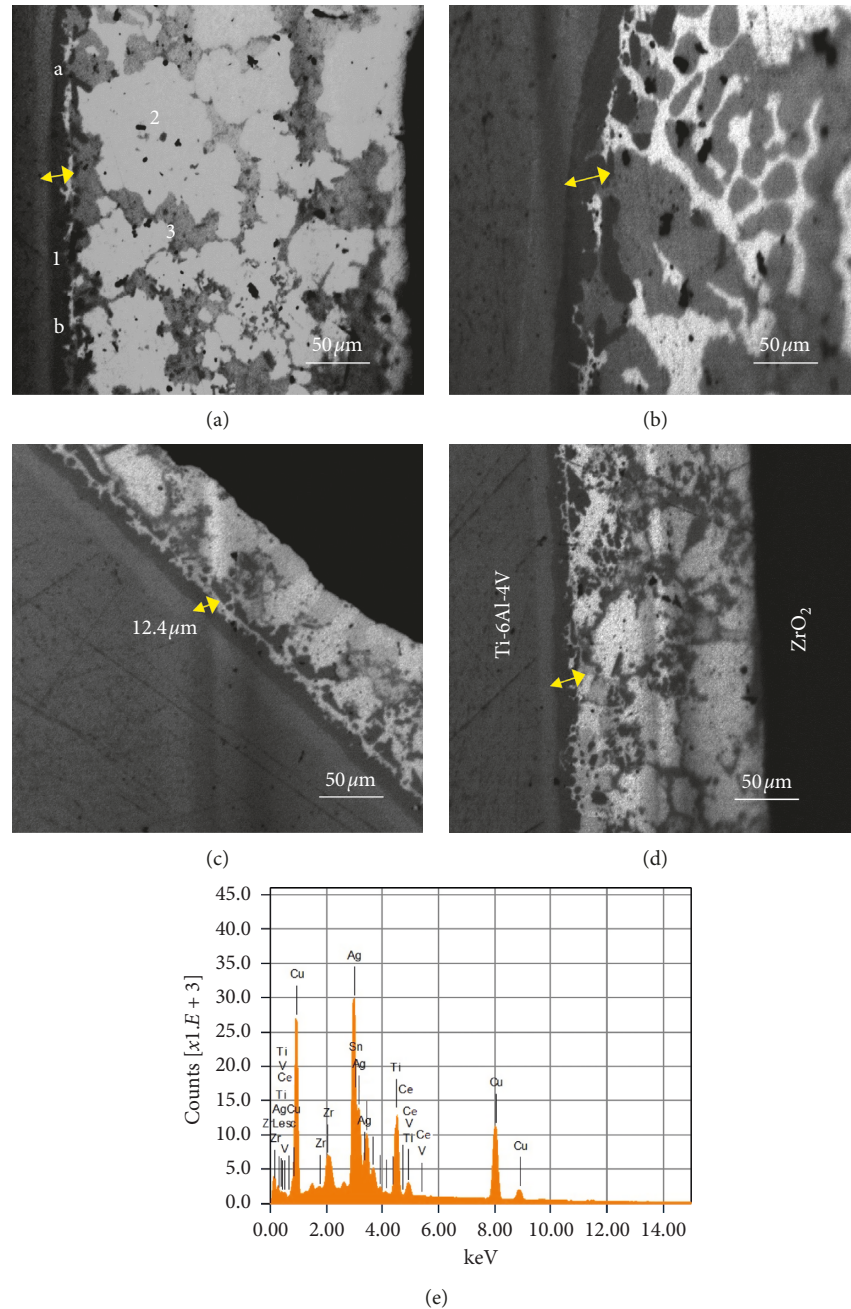


FIGURE 8: The cross-sectional SEM image of the ZrO₂/Ti-6Al-4V interface brazed using various Ag-Cu-Ti-xCeO₂ composites: (a) $x=0$; (b) $x=0.03$; (c) $x=0.05$; (d) $x=0.1$; (e) EDS analysis of (d).

melt. Therefore, the hardness decrease is associated with two factors: (1) presence of cracks in the sample and (2) poor incorporation of the CeO₂ nanoparticles in the filler matrix at high concentration. This may be due to the increased viscosity and poor wetting of CeO₂ nanoparticles in the melt beyond $x > 0.05$ wt% [11].

3.7. Brazed Joint Shear Strength. The joint shear strength was performed for various composite fillers ($x=0, 0.03, 0.05,$ and 0.1). The shear stress-strain diagram is shown in Figure 10. The various shear stress data are shown in Table 5.

It can be seen that the joint shear strength increases with the addition of CeO₂ nanoparticles up to 0.05 wt% in the filler matrix. The sample brazed with filler with $x=0$ shows a shear strength of ~ 19.9 MPa. The stress increases gradually to 20.4 MPa and 22.8 MPa for the case of $x=0.03$ and 0.05 respectively. The improvement in joint strength at an optimum content of CeO₂ (0.05 wt%) can be attributed to the various factors: (1) presence of harder CeO₂ nanoparticles that obstruct the localized deformation of the matrix, (2) CeO₂ nanoparticles restrict the growth of Cu-Ti IMCs in the filler matrix, and (3) Orowan strengthening due to dislocations form loops around the fine IMCs and CeO₂ particles [8, 11, 13].

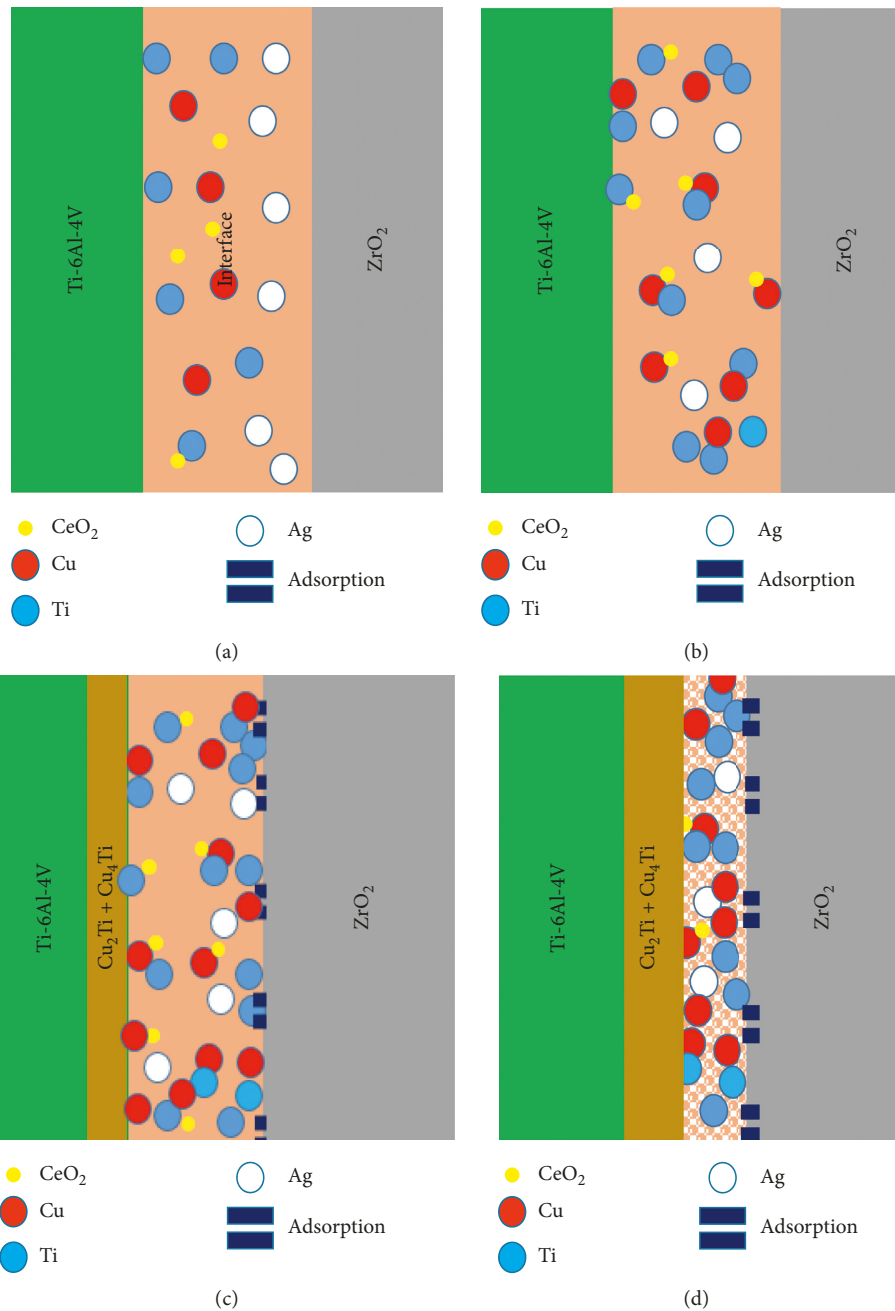


FIGURE 9: Schematic for joint formation and bonding of the ZrO₂/Ti-6Al-4V joint.

TABLE 4: Microhardness values of composite fillers as a function of CeO₂ (wt%).

Serial no.	Sample ID	Microhardness (Hv)
1	Ag-Cu-Ti	115.1
2	Ag-Cu-Ti-0.03 CeO ₂	119.4
3	Ag-Cu-Ti-0.05 CeO ₂	126.6
4	Ag-Cu-Ti-0.1 CeO ₂	112.5

The shear strength is decreased to 12.6 MPa for $x = 0.1$, as expected. This may be due to the poor spreadability of this sample as already discussed [9–11]. A very high amount of CeO₂ nanoparticles (0.1 wt%) is not desirable in the Ag-Cu-Ti

matrix because it may deteriorate the joint microstructure and strength. This may be due to the high amount of ceria nanoparticles in the melt that decreases the melt fluidity and spreadability [11]. Therefore, it can be concluded from this

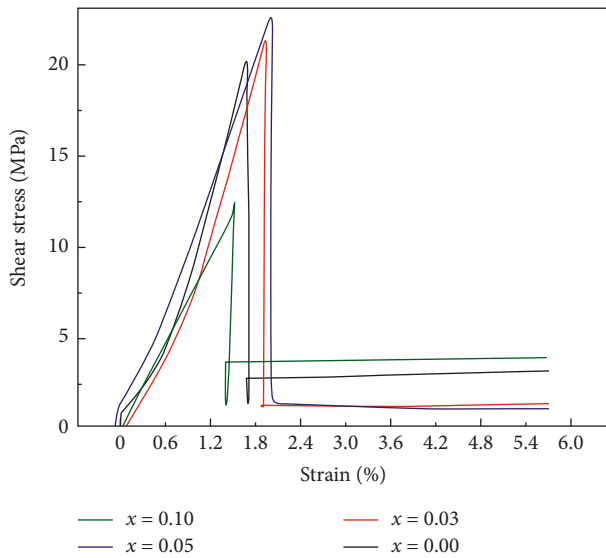


FIGURE 10: Shear stress-strain curves of the various Ag-Cu-Ti- x CeO₂ composites.

TABLE 5: Shear strength data obtained from the shear stress-strain curve.

Serial no.	Sample ID	UTS (MPa)
1	Ag-Cu-Ti	19.9
2	Ag-Cu-Ti-0.03 CeO ₂	20.4
3	Ag-Cu-Ti-0.05 CeO ₂	22.8
4	Ag-Cu-Ti-0.1 CeO ₂	12.6

work that, for an optimum brazing performance of the ZrO₂/Ti-6Al-4V joint, the desired amount of CeO₂ nanoparticles should not exceed ~0.05 wt% in the Ag-Cu-Ti filler matrix.

4. Conclusions

- (1) The cerium oxide nanoparticles were successfully produced using the solution combustion method. The particle size of the ceria nanoparticles was under 20–30 nm, and lattice strain was around 0.39.
- (2) The Ag-Cu-Ti filler microstructure was composed of Cu-rich and Ag-rich phases and Cu-Ti IMCs. It was found that, with an addition of ceria in the filler matrix (up to 0.05 wt%), the various phases were refined considerably.
- (3) The addition of CeO₂ nanoparticles in the filler matrix improved the wettability of filler on both ZrO₂ and Ti-6Al-4V substrates up to $x=0.05$ and then decreased dramatically at $x=0.1$ due to increasing melt viscosity.
- (4) The melting point study shows a depression in the melting point of composite fillers around 3°C when reinforced with 0.05 wt% CeO₂.
- (5) With the increase in the CeO₂ content, the thickness of the reactive layer (Cu₂Ti + Cu₄Ti) between the interface and base materials was reduced

significantly up to the optimum ceria fraction 0.05 wt % in the filler matrix.

- (6) The microhardness of the filler matrix shows an 11.1% increase over the filler matrix when embedded with 0.05 wt% ceria nanoparticles.
- (7) The joint shear test showed that maximum brazed strength was obtained for $x=0.05$; however, it decreased further due to the poor brazeability of filler at $x=0.1$.

Data Availability

The data used to support the findings of this study are available from the corresponding author upon request.

Conflicts of Interest

The authors declare that there are no conflicts of interest regarding the publication of this work.

Acknowledgments

This research was supported by Basic Science Research Program through the National Research Foundation of Korea (NRF) funded by the Ministry of Education (NRF-2018R1D1A1B07044481 to B.A. and NRF-2018R1D1A1B07044706 to A.S.).

References

- [1] R. M. do Nascimento, A. E. Martinelli, and A. J. A. Buschinelli, "Review article: recent advances in metal-ceramic brazing," *Cerâmica*, vol. 49, no. 312, pp. 178–198, 2003.
- [2] M. B. Uday, M. N. Ahmad Fauzi, M. N. Alias, and S. Rajoo, "Current issues and problems in the joining of ceramic to metal," in *Joining Technologies*, M. Ishak, Ed., InTech Publications, Rijeka, Croatia, 2016.
- [3] J. Shin, A. Sharma, D.-H. Jung, and J. P. Jung, "Effect of Sn content on filler and bonding characteristics of active metal brazed Cu/Al₂O₃ joint," *Korean Journal of Metals and Materials*, vol. 56, no. 5, pp. 366–374, 2018.
- [4] A. Sharma, S. H. Kee, F. Jung, Y. Heo, and J. P. Jung, "Compressive strength evaluation in brazed ZrO₂/Ti-6Al-4V joints using finite element analysis," *Journal of Materials Engineering and Performance*, vol. 25, no. 5, pp. 1722–1728, 2016.
- [5] V. Srinivas, A. K. Singh, V. Gopala Krishna, and G. Madhusudhan Reddy, "Vacuum brazing of dissimilar tubular component of AA2219 and AISI 304 by a low melting Al-18Ag-20Cu-5Si-0.2Zn braze alloy," *Journal of Materials Processing Technology*, vol. 252, pp. 1–12, 2018.
- [6] W. D. Kingery, H. K. Bowen, and D. R. Uhlmann, *Introduction to Ceramics*, Wiley-Interscience, Hoboken, NJ, USA, 2nd edition, 1976.
- [7] M. M. Schwartz, *Brazing*, ASM International, Cleveland, OH, USA, 2nd edition, 2003.
- [8] A. Sharma, M.-H. Roh, D.-H. Jung, and J.-P. Jung, "Effect of ZrO₂ nanoparticles on the microstructure of Al-Si-Cu filler for low-temperature Al brazing applications," *Metallurgical and Materials Transactions A*, vol. 47, no. 1, pp. 510–521, 2016.
- [9] A. Sharma, D. U. Lim, and J. P. Jung, "Microstructure and brazeability of SiC nanoparticles reinforced Al-9Si-20Cu

- produced by induction melting,” *Materials Science and Technology*, vol. 32, no. 8, pp. 773–779, 2016.
- [10] A. Sharma, M. H. Roh, and J. P. Jung, “Effect of La_2O_3 nanoparticles on the brazeability, microstructure, and mechanical properties of Al-11Si-20Cu alloy,” *Journal of Materials Engineering and Performance*, vol. 25, no. 8, pp. 3538–3545, 2016.
- [11] A. Sharma, D. E. Xu, and J. P. Jung, “Effect of different nanoparticles on microstructure, wetting and joint strength of Al-12Si-20Cu braze filler,” *Materials Research Express*, vol. 6, no. 5, Article ID 056526, 2019.
- [12] J. Shen and Y. C. Chan, “Research advances in nano-composite solders,” *Microelectronics Reliability*, vol. 49, no. 3, pp. 223–234, 2009.
- [13] A. Sharma, B. G. Baek, and J. P. Jung, “Influence of La_2O_3 nanoparticle additions on microstructure, wetting, and tensile characteristics of Sn-Ag-Cu alloy,” *Materials & Design*, vol. 87, pp. 370–379, 2015.
- [14] A. Sharma, H. Yu, I. S. Cho, H. Seo, and B. Ahn, “ ZrO_2 nanoparticle embedded low silver lead free solder alloy for modern electronic devices,” *Electronic Materials Letters*, vol. 15, no. 1, pp. 27–35, 2019.
- [15] M. C. Halbig, B. P. Coddington, R. Asthana, and M. Singh, “Characterization of silicon carbide joints fabricated using SiC particulate-reinforced Ag-Cu-Ti alloys,” *Ceramics International*, vol. 39, no. 4, pp. 4151–4162, 2013.
- [16] Q. Miao, W. Ding, D. Fu, Z. Chen, and Y. Fu, “Influence of graphite addition on bonding properties of abrasive layer of metal-bonded CBN wheel,” *The International Journal of Advanced Manufacturing Technology*, vol. 93, no. 5–8, pp. 2675–2684, 2017.
- [17] B. Zhao, W. Ding, W. Kuang, and Y. Fu, “Microstructure and tribological property of self-lubrication CBN abrasive composites containing molybdenum disulfide,” *Industrial Lubrication and Tribology*, vol. 71, no. 5, pp. 712–717, 2019.
- [18] Q. Miao, W. Ding, Y. Zhu, Z. Chen, and Y. Fu, “Brazing of CBN grains with Ag-Cu-Ti/TiX composite filler—the effect of TiX particles on microstructure and strength of bonding layer,” *Materials & Design*, vol. 98, pp. 243–253, 2016.
- [19] J. Yang, H. Y. Fang, and X. Wan, “Effects of Al_2O_3 particulate contained composite filler materials on the strength of alumina joints,” *Journal of Materials Science & Technology*, vol. 18, no. 4, pp. 289–290, 2002.
- [20] A. Sharma, A. K. Srivastava, K. Lee, and B. Ahn, “Impact of non-reactive ceria nanoparticles on the wettability and reaction kinetics between lead-free Sn-58Bi and Cu pad,” *Metals and Materials International*, vol. 25, no. 4, pp. 1027–1038, 2019.
- [21] A. Sharma, A. K. Srivastava, and B. Ahn, “Microstructure, mechanical properties, and drop reliability of CeO_2 reinforced Sn-9Zn composite for low temperature soldering,” *Materials Research Express*, vol. 6, no. 5, Article ID 056520, 2019.
- [22] R. Sun, Y. Sui, J. Qi et al., “Influence of SnO_2 nanoparticles addition on microstructure, thermal analysis, and interfacial IMC growth of Sn1.0Ag0.7Cu solder,” *Journal of Electronic Materials*, vol. 46, no. 7, pp. 4197–4205, 2017.
- [23] S. Bhattacharya, A. Sharma, S. Das, and K. Das, “Synthesis and properties of pulse electrodeposited lead-free tin-based Sn/ ZrSiO_4 nanocomposite coatings,” *Metallurgical and Materials Transactions A*, vol. 47, no. 3, pp. 1292–1312, 2016.
- [24] F. Moszner, C. Cancellieri, C. Becker, M. Chiodi, J. Janczak-Rusch, and L. P. H. Jeurgens, “Nano-structured Cu/W brazing fillers for advanced joining applications,” *Journal of Materials Science and Engineering B*, vol. 6, no. 5, pp. 226–230, 2016.
- [25] H. Bian, Q. Zhang, Y. Song, D. Liu, J. Liu, and X. Song, “Microstructure and mechanical properties of a SiO_2 ceramic and TC_4 alloy joint brazed with a nanocomposite filler,” *Journal of Materials Engineering and Performance*, vol. 28, no. 7, pp. 4427–4433, 2019.
- [26] D. Busbaher, W. Liu, and D. P. Sekulic, “Mechanical properties of nanoparticles reinforced Mo-Ni braze for a dispenser cathode application,” in *Proceedings of the 14th International Vacuum Electronics Conference (IVEC)*, pp. 1–2, IEEE, Monterey, CA, USA, April 2013.
- [27] A. Sharma, “Effect of synthesis routes on microstructure of nanocrystalline cerium oxide powder,” *Materials Sciences and Applications*, vol. 4, no. 9, pp. 504–508, 2013.
- [28] A. Sharma, H.-R. Sohn, and J. P. Jung, “Effect of graphene nanoplatelets on wetting, microstructure, and tensile characteristics of Sn-3.0Ag-0.5Cu (SAC) alloy,” *Metallurgical and Materials Transactions A*, vol. 47, no. 1, pp. 494–503, 2016.
- [29] JIS Z 3192: 1999, *Methods of Tensile and Shear Tests for Brazed Joint*, Japanese Standards Association, Tokyo, Japan, 1999.
- [30] *Powder Diffraction File, International Center for Diffraction Data (ICDD)*, Newtown Square, PA 19073-3273, USA, <http://www.icdd.com/>.
- [31] Y. M. He, J. Zhang, C. F. Liu, and Y. Sun, “Microstructure and mechanical properties of $\text{Si}_3\text{N}_4/\text{Si}_3\text{N}_4$ joint brazed with Ag-Cu-Ti + SiCp composite filler,” *Materials Science and Engineering: A*, vol. 527, no. 12, pp. 2819–2825, 2010.
- [32] Q. Miao, W. Ding, Y. Zhu, Z. Chen, J. Xu, and C. Yang, “Joining interface and compressive strength of brazed cubic boron nitride grains with Ag-Cu-Ti/TiX composite fillers,” *Ceramics International*, vol. 42, no. 12, pp. 13723–13737, 2016.

Research Article

Precision Forming Technology for Crimping of Large Straight Welded Pipes

Li-feng Fan ¹, Pei Liang,² Ge Wang,² Ying Gao ³ and Benguo Zhang⁴

¹Transportation Institute, Inner Mongolia University, Hohhot 010070, China

²National Engineering Research Center for Equipment and Technology of Cold Strip Rolling, Yanshan University, Qinhuangdao 066004, China

³College of Material Science and Engineering, Hebei University of Science and Technology, Shijiazhuang 050018, China

⁴Jiangsu Mould Intelligent Manufacturing Engineering Research Center, Yancheng 224051, China

Correspondence should be addressed to Li-feng Fan; fanlifeng@imu.edu.cn

Received 5 July 2019; Accepted 14 October 2019; Published 31 October 2019

Guest Editor: Benjamin I. Imasogie

Copyright © 2019 Li-feng Fan et al. This is an open access article distributed under the Creative Commons Attribution License, which permits unrestricted use, distribution, and reproduction in any medium, provided the original work is properly cited.

Crimping plays a pivotal role in the production of large-diameter submerged-arc welded pipes. In the crimping forming process, predicting the springback while considering the real-time variation of material parameters is a major challenge faced by many researchers, which has a direct impact on the quality of the welded pipe. To address this problem, the precision forming technology of crimping was developed. The engineering theory of plastic bending was used to investigate the crimping forming process. Two methods, namely, the slope reverse method and the optimization method, were adopted to identify the material parameters. The results showed that the inverted material parameters can be evaluated in real time based on the analytical model of crimping. The maximum relative error of the identification value is less than 4%. Therefore, the springback and displacement during crimping can be predicted dynamically to control the crimping forming quality. Thus, this project provides an important opportunity to achieve precise forming through crimping.

1. Introduction

The forming technology of crimping has been extensively used in the production of large-diameter straight seam submerged-arc welded (LSAW) pipes. To improve the geometry and dimensional accuracy of LSAW pipes, both sides of the sheet edge were bent into a certain nominal curvature by crimping, which can effectively prevent peach breaks and cracking during expansion.

A considerable amount of literature has been published on crimping forming processes. These studies address the stress and strain state of the plate in crimping [1], the effects of technological parameters on the crimping forming quality [2], and the effects of crimping on the pipe quality [3–5] by the finite element analysis (FEA) method.

The most significant disadvantages of FEA in the design of crimping parameters are its time required and the difficulty in identifying material parameters. However, the

analytical method can improve the computational efficiency by idealizing the forming conditions. Scholars have analyzed the crimping forming process quality using analytical methods for the design parameters [6, 7], bending moment/forming force [8], stress/strain, and springback [9].

It has previously been observed that the control of springback, which happens after the removal of the forming loads, remains a key issue in the crimping process. A number of intersectional studies have been published on springback calculations [10–12], springback reduction [13, 14], and the springback mechanism [15]. However, few studies have investigated the influence of the fluctuation of mechanical properties on the control accuracy of springback in applications. Hence, efforts have been made to reduce the influence of the fluctuation of mechanical material properties on springback by the robustness design method [16, 17], but this work still has not achieved the purpose of precise forming of crimping.

Therefore, the purpose of this investigation is to propose a precision forming method for crimping. First, the quantitative relationship between the bending displacement and bending force was calculated by the analytical method of crimping. Second, the identification of material parameters was performed by the gray correlation method. Finally, crimping displacement predictions were achieved by the springback prediction model. The ideal crimping displacement can undergo dynamic adjustment by using the precision forming technology for crimping. The proposed technology has demonstrated that it is not only the forming accuracy that can be effectively improved in precision crimping but a lot of design times can be saved.

2. Analytical Model of Crimping

In this study, the analytical method as an efficient tool was used to calculate the quantitative relationship between the bending displacement and bending force. In the crimping forming process, the punch and the edges of the sheet are fixed. With the die loading progressively increasing, the edges of the sheet are gradually bent along the punch surface. Then, the process of unloading the sheet is begun by moving the die down when the sheet reaches the target bending angle. Crimping is completed after springback of the sheet (Figure 1).

The parameter equation of the involute can be used to describe the shape of the punch and die in Cartesian coordinates:

$$\begin{cases} x(\varphi) = R_p \cos \varphi + \varphi R_p \sin \varphi, \\ y(\varphi) = R_p \sin \varphi + \varphi R_p \cos \varphi, \end{cases} \quad (1)$$

where R_p is the base radius and φ is the base angle.

To facilitate subsequent calculation, a new XOY coordinate system, with point O as the original point that is the involute end point corresponding to the terminal base angle β_p , is established. The parameter equation of the crimping punch in the XOY coordinate system is modified as follows:

$$\begin{cases} X(\varphi) = (x(\varphi) - x(\beta_p))\cos(\beta_p) + (y(\varphi) - y(\beta_p))\sin(\beta_p), \\ Y(\varphi) = -(x(\varphi) - x(\beta_p))\sin(\beta_p) + (y(\varphi) - y(\beta_p))\cos(\beta_p). \end{cases} \quad (2)$$

Therefore, the curvature radius of punch ρ according to the involute property can be calculated as follows:

$$\rho = R_p \cdot (\beta_p - \theta), \quad (3)$$

where θ is the crimping bending angle.

In the analytical model of crimping, the description of the material behavior is very important. To simplify the calculation, it is assumed that a state of plane strain exists:

$$\varepsilon = \frac{y}{\rho}. \quad (4)$$

The elastic behavior according to Hooke's law can be written as follows for a state of plane strain:

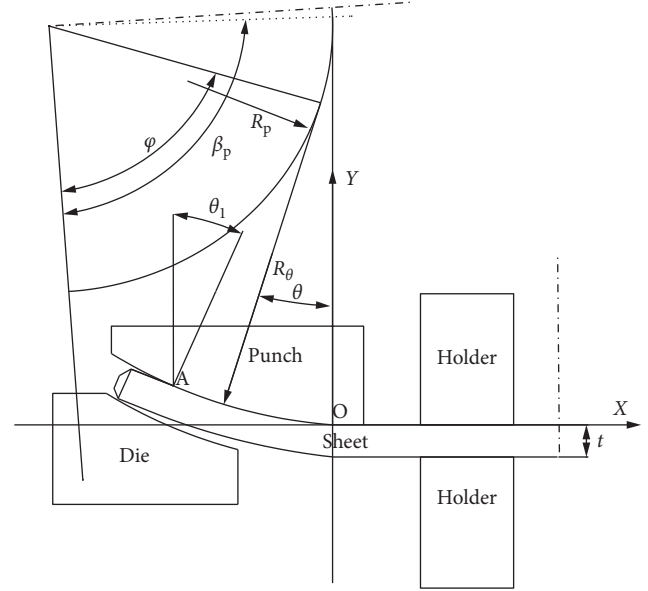


FIGURE 1: Crimping sketch.

$$\sigma = E\varepsilon. \quad (5)$$

As the stress-strain relationship for plastic deformation, a linear hardening law is adopted here:

$$\sigma = \sigma_s + E_p \varepsilon. \quad (6)$$

In this study, three deformed stages can be determined in the whole crimping forming process: (1) elastic deformation, (2) unwrapped stage in the elastoplastic regime, and (3) wrapped stage in the elastoplastic regime.

2.1. Elastic Deformation Stage. When the radius of curvature in crimping section ρ is larger than the elastic limit radius of curvature ρ_e

$$\rho_e = \frac{tE}{2\sigma_s}. \quad (7)$$

In this phase, the crimping deformation occupies the whole elastic deformation stage. Thus, the bending moment can be expressed as

$$M = \frac{EI}{\rho}, \quad (8)$$

where I is the section moment of inertia, $I = 2 \int_0^{t/2} y^2 dy$.

In addition, the bending moment can be calculated according to the external force

$$\begin{cases} M = F_x(y_1 - y) + F_y(x_1 - x), \\ F_x = F \sin \theta_1, \\ F_y = F \cos \theta_1, \end{cases} \quad (9)$$

where F_x is the horizontal forming force and F_y is the vertical forming force.

According to the geometry, the following relationships can be obtained:

$$\begin{cases} \frac{ds}{d\theta} = \rho, \\ dx = ds \cos \theta, \\ dy = ds \sin \theta. \end{cases} \quad (10)$$

We simultaneously apply equations (8)–(10) and differentiate both sides of the equation:

$$-EI \frac{d^2\theta}{ds^2} = F \sin \theta_1 \sin \theta + F \cos \theta_1 \cos \theta. \quad (11)$$

Note:

$$\frac{d^2\theta}{ds^2} = \frac{1}{2} \frac{d}{d\theta} \left[\left(\frac{d\theta}{ds} \right)^2 \right]. \quad (12)$$

Therefore, the equation can become

$$-\frac{EI}{2} d \left[\left(\frac{d\theta}{ds} \right)^2 \right] = (F \sin \theta_1 \sin \theta + F \cos \theta_1 \cos \theta) d\theta. \quad (13)$$

The following equation can be obtained by integrating both sides of differential equation:

$$-\frac{EI}{2} \left(\frac{d\theta}{ds} \right)^2 = -F \sin \theta_1 \cos \theta + F \cos \theta_1 \sin \theta + C. \quad (14)$$

According to boundary conditions, when $\theta = \theta_1$, $ds/d\theta$ and the coefficient $C = 0$. Therefore,

$$\frac{ds}{d\theta} = \sqrt{\frac{EI}{2F(\sin \theta_1 \cos \theta - \cos \theta_1 \sin \theta)}}. \quad (15)$$

The curve equation can be obtained by solving the differential equation, and the crimping angle θ_1 can be determined by the following formula:

$$s = \int_0^{\theta_1} \psi(\theta) d\theta = L, \quad (16)$$

where $\psi(\theta) = \sqrt{EI/2F \sin(\theta_1 - \theta)}$.

2.2. Unwrapped Stage in Elastoplastic Deformation. As the bending displacement increases, the bending radius of the curvature is smaller than the maximum elastic radius of the curvature but still larger than the radius of curvature of the punch. The stage enters the unwrapped stage in elastoplastic deformation. Therefore, the entire deformation section can be divided into an elastic deformation section and an elastic-plastic deformation section. The elastic-plastic bending moment M can be expressed as

$$M = A\rho^2 + B\frac{1}{\rho} + C, \quad (17)$$

where $A = ((2\sigma_s^3 - 2E_p\sigma_s^3)/3E^2) - (\sigma_s^3/E^2)(1 - (E_p/E))$, $B = E_p t^3/12$, and $C = (\sigma_s t^4/4)(1 - (E_p/E))$.

The differential equations can be obtained by simultaneous application of equations (2) and (3):

$$A \left(\frac{ds}{d\theta} \right)^2 + B \left(\frac{d\theta}{ds} \right) + C = F_x(y_1 - y) + F_y(x_1 - x). \quad (18)$$

Differentiate as follows:

$$A \frac{d}{ds} \left[\left(\frac{ds}{d\theta} \right)^2 \right] + B \frac{d}{ds} \left(\frac{d\theta}{ds} \right) = -F_x \frac{dy}{ds} - F_y \frac{dx}{ds}. \quad (19)$$

Note that

$$2 \frac{d^2s}{d\theta^2} = \frac{d}{ds} \left[\left(\frac{ds}{d\theta} \right)^2 \right]. \quad (20)$$

The differential equation can be obtained as follows:

$$2A \frac{d^2s}{d\theta^2} + B \frac{d^2\theta}{ds^2} = -F \cos(\theta_1 - \theta). \quad (21)$$

The conditions $\theta = \theta_p$ and $s = l_p$ mark the boundary point between the elastic section and the elastoplastic section. In addition, at $M = M_{\max-e}$, the following formula can be satisfied:

$$M_{\max-e} = \sqrt{2FEI \sin(\theta_1 - \theta_p)} = \frac{1}{6} \sigma_s t^2. \quad (22)$$

From this boundary condition, the relationship between F and the position of the boundary point is given but depends only on the value that cannot be determined by the elastoplastic deformation section, and the elastic deformation section is needed to supplement the solution:

$$s = \int_{\theta_p}^{\theta_1} \psi(\theta) d\theta = L - l_p = l_e. \quad (23)$$

2.3. Elastoplastic Deformation Wrapped Stage. As the bending deformation increases, the radius of curvature becomes equal to the radius of curvature of the punch at the corresponding position, and the deformation is in the elastoplastic deformation wrapped stage. The whole sheet can be divided into three sections: elastic, elastoplastic unwrapped, and elastoplastic wrapped section.

The relationship between the bending moment and the curvature of the elastic-plastic cladding section can be calculated according to the radius of curvature of the convex model surface. The origin of the coordinate system is translated to the centroid of the starting position of the bending of the sheet, and the downward translation is available:

$$\begin{cases} x^*(\varphi) = [x(\varphi) - x(\beta_p)] \cos \beta_p + [y(\varphi) - y(\beta_p)] \sin \beta_p, \\ y^*(\varphi) = [x(\varphi) - x(\beta_p)] \sin \beta_p + [y(\varphi) - y(\beta_p)] \cos \beta_p + \frac{t}{2}. \end{cases} \quad (24)$$

According to the involute property, the curvature radius of the sheet intermediate layer ρ_θ can be known:

$$\rho_\theta = R_p \cdot (\beta_p - \theta) + \frac{t}{2}. \quad (25)$$

Therefore, the bending moment of the covered section is

$$M_\theta = \left[\frac{2\sigma_s^3 - 2E_p\sigma_s^3}{3E^2} - \frac{\sigma_s^3}{E^2} \left(1 - \frac{E_p}{E} \right) \right] \rho_\theta^2 + \frac{E_p t^3}{12} \frac{1}{\rho_\theta} + \frac{\sigma_s t^4}{4} \left(1 - \frac{E_p}{E} \right). \quad (26)$$

According to the involute arc length formula, the length of the wrapping section can be obtained as

$$l_w = \int_\theta^{\theta_w} \sqrt{\left(\frac{dx^*}{d\theta} \right)^2 + \left(\frac{dy^*}{d\theta} \right)^2} d\theta. \quad (27)$$

When $\theta_w \leq \theta \leq \theta_p$, the length of the unwrapping section can be obtained from

$$2A \frac{d^2 s}{d\theta^2} + B \frac{d^2 \theta}{ds^2} = -F \cos(\theta_1 - \theta). \quad (28)$$

The elastic deformation section is needed to supplement the solution:

$$s = \int_{\theta_p}^{\theta_1} \psi(\theta) d\theta = L - l_p - l_w. \quad (29)$$

2.4. Verification for Analytical Model. In this study, an X80 grade $\Phi 1219 \times 22 \times 12000$ mm large-diameter straight seam welded pipe was taken as an example, and a #3 crimping mold was adopted as the research object. The mold parameters are shown in Table 1.

To evaluate the precision of the bending analysis model, the crimping forming process was conducted by a hydropress in the plant. The forming force and displacement can be collected with a pressure sensor and a displacement sensor. Then, the comparison between the measured values and those calculated from the analytical model is shown in Figure 2.

As seen from Figure 2, the calculation results are in good agreement with the measurement results and their maximum relative error is less than 9.06%.

3. Identification of the Material Parameters

To adjust the forming parameters online, it is necessary to identify the mechanical properties of materials in real time considering the influence of fluctuations of the mechanical material properties on the springback. Therefore, first, the effects of the mechanical properties on the bending load curve are analyzed based on the crimping analytical model, and then the initial segment of the bending load curve is used to identify the elastic modulus. Finally, the objective function is constructed by the gray correlation method, and the yield strength and the plastic modulus are identified by the inverse optimization method. In this section, the #3 crimping mold remains the research object.

3.1. Effects of the Material Parameters on the Forming Force.

To improve the identification accuracy and efficiency, the effects of the elastic modulus, yield strength, and plastic modulus on the bending displacement and bending load curve are analyzed, as shown in Figures 3–6.

TABLE 1: Parameters of the crimping mold.

Parameters	Value
Base radius of punch R_p (mm)	303.20
Terminal angle of the punch β_p (°)	88
Base radius of the die R_d (mm)	303.20
Terminal angle of the die β_d (°)	88
Length of crimping B (mm)	190
Horizontal distance between the punch and die D (mm)	80

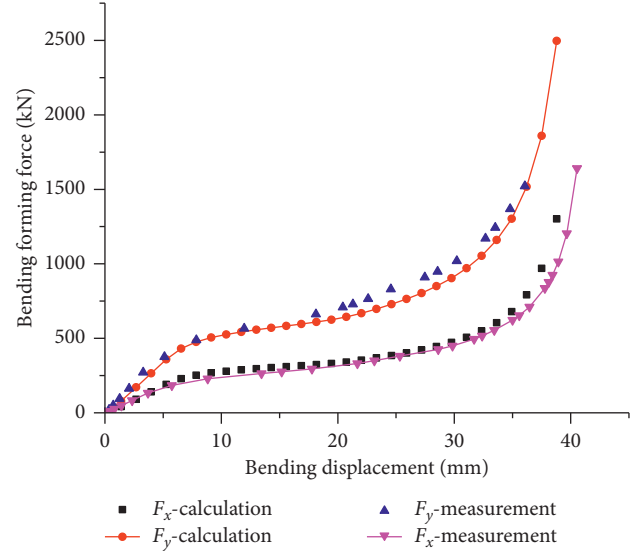


FIGURE 2: Verification with bending force.

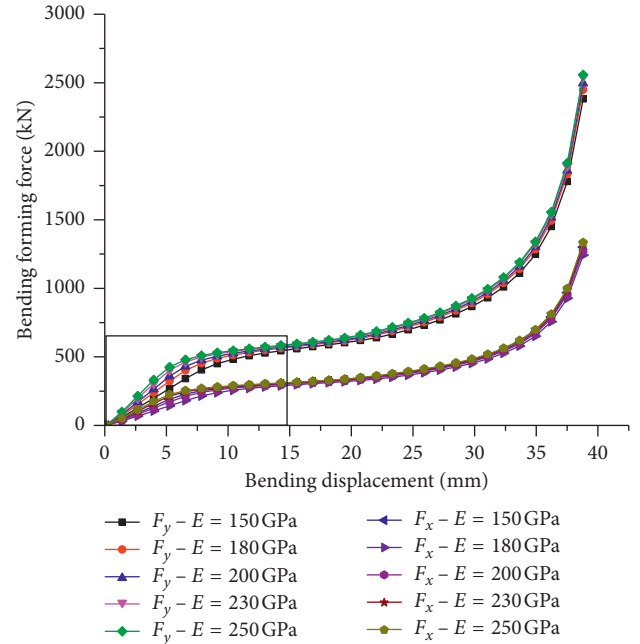


FIGURE 3: Effects of the elastic modulus on the bending load.

It can be seen from Figures 3 and 4 that the elastic modulus has a significant influence on the initial segment of the curve and has little effect on the subsequent plastic

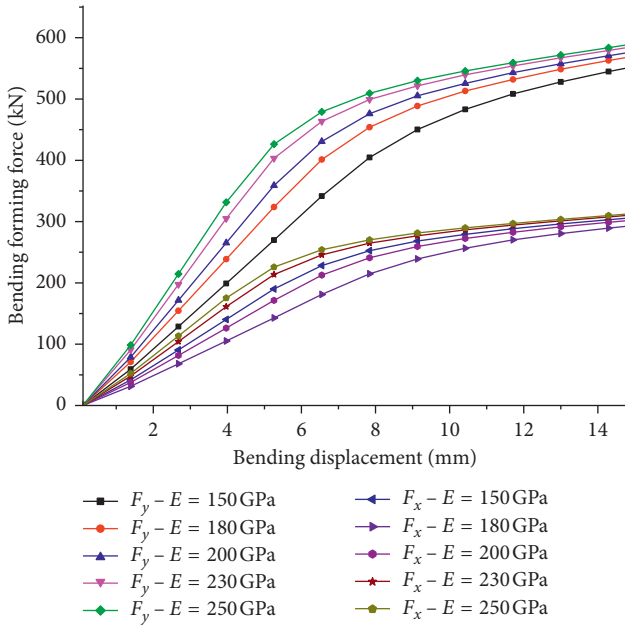


FIGURE 4: Partial enlargement of Figure 3.

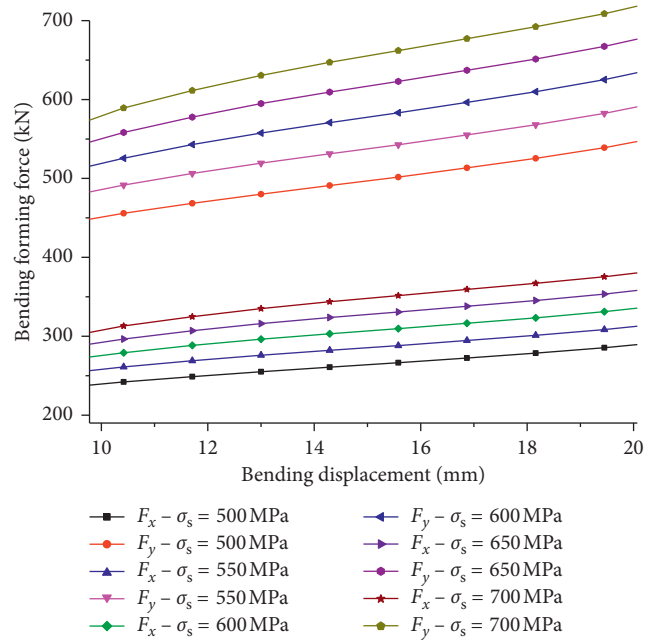


FIGURE 6: Partial enlargement of Figure 5.

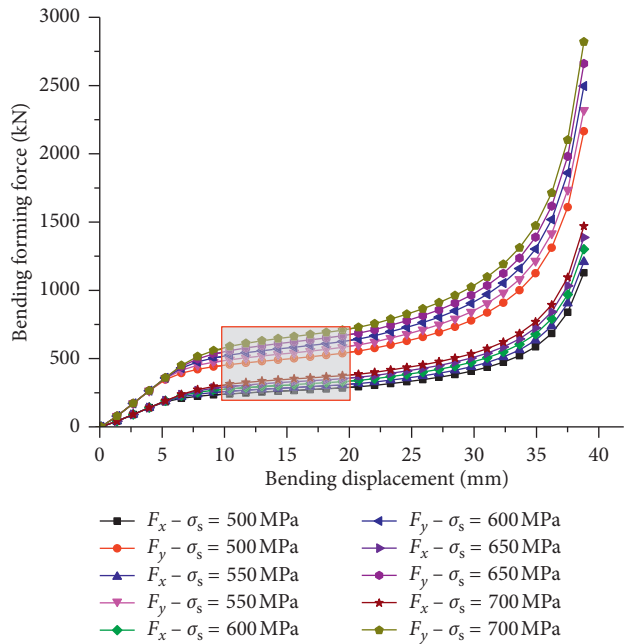


FIGURE 5: Effects of the yield strength on the bending load.

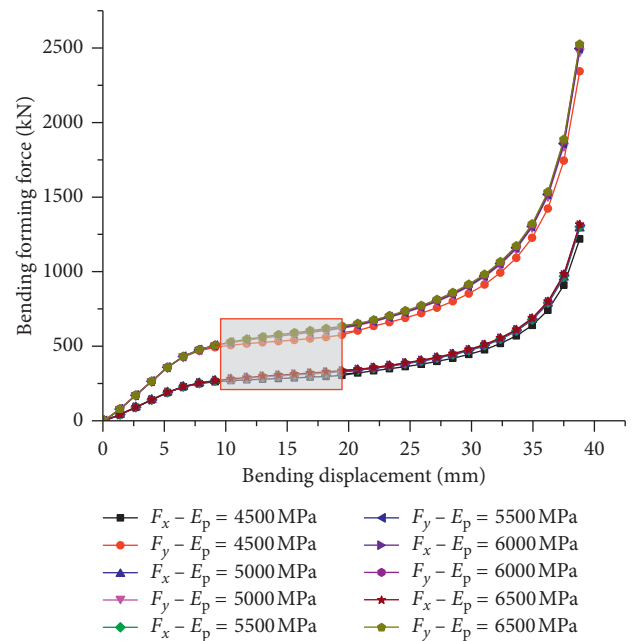


FIGURE 7: Effects of the plastic modulus on the bending load.

segment, and it is found that the initial segment of the curve is approximately linear.

It can be seen from Figures 5–8 that the change of the yield strength has no effect on the initial section of the curve, but the influence on the subsequent plastic section of the curve is more obvious, and the bending load increases as the yield strength increases with the same bending stroke.

3.2. Identification of the Elastic Modulus. In the elastic deformation stage, it was determined from the theoretical

analytical model that only the elastic modulus has a direct influence on the bending load. The analysis of the influence rate of the elastic modulus on the forming load at different displacements is shown in Figure 9. This demonstrated that in the elastic deformation stage ($h < 5 \text{ mm}$), the degree of influence increases with increasing displacement and that linearity is satisfied.

However, in the plastic deformation stage, the plastic material parameters play a major role, and the influence of the elastic modulus on the forming load is weakened. To

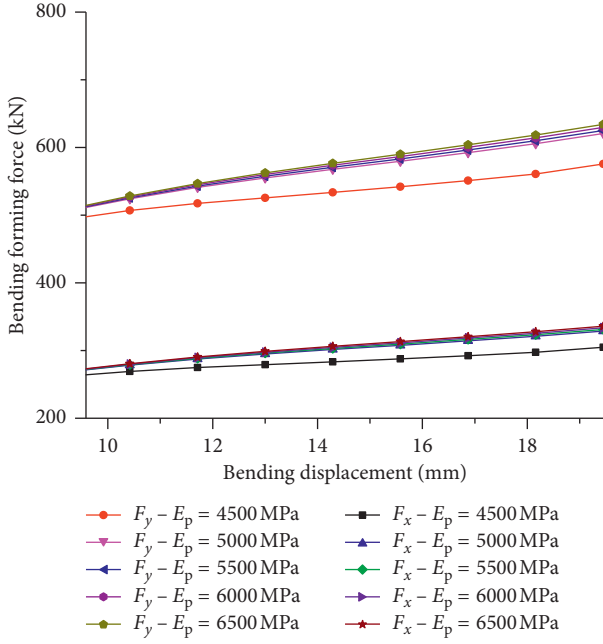


FIGURE 8: Partial enlargement of Figure 7.

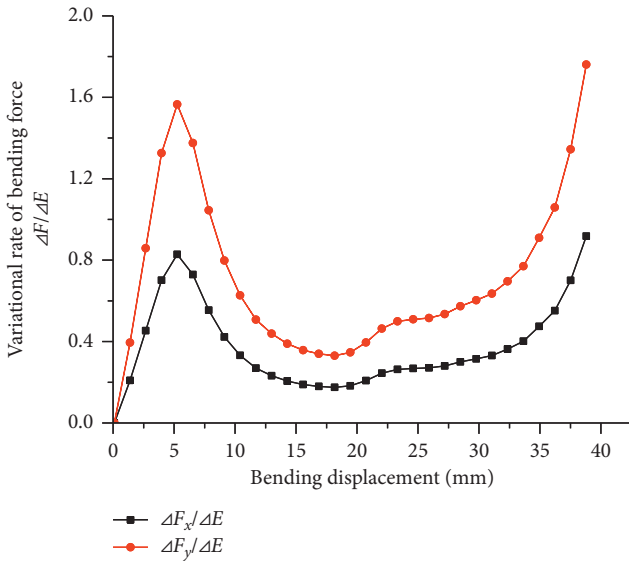


FIGURE 9: Effect of the rate elastic modulus on the bending load.

identify the elastic modulus in the elastic deformation stage, the effect of the elastic modulus on the slope of the loading curve at the elastic deformation stage is analyzed in Figure 10, as fit by the following linear formula:

$$\begin{cases} E = -0.0028S_y + 402.07, \\ E = -0.0053S_x + 402.08, \end{cases} \quad (30)$$

where E is the elastic modulus and S_x , S_y is the slope of the horizontal and vertical forming forces, respectively.

Therefore, the elastic modulus can be identified by equation (30).

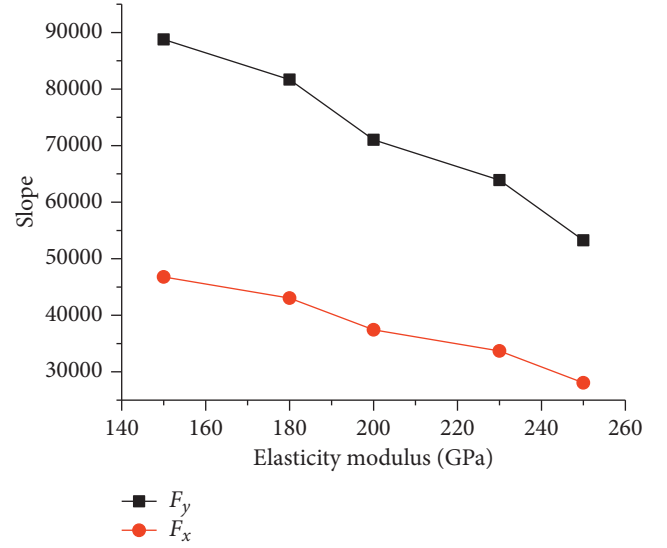


FIGURE 10: Effects of the elastic modulus on the slope of the loading curve during the elastic deformation stage.

3.3. Plastic Parameter Inversion. It is found that both the yield strength and the plastic modulus have a significant influence on the plastic segment of the bending load curve, and its trends are to increase slowly and then rapidly in Figures 11 and 12.

Therefore, to identify the plastic parameters, the yield strength and plastic modulus are substituted into the crimping analytical model for trial calculation by the optimization algorithm, in which the calculated curve is refined to approximate the measured curve until it reaches the allowable error.

The gray relational theory was applied to construct the objective function of inverse identification f_{object} , which can comprehensively evaluate the approximation characteristics of the calculated curve and the measured curve as follows.

3.3.1. Reference Sequence and Relative Sequence. The bending loads $F^e = [F_1 \ F_2 \ \dots \ F_n]$ corresponding to the measured bending displacements $h = [h_1 \ h_2 \ \dots \ h_n]$ were selected as the reference sequence, and then the bending loads $F_i(k) = [F_i(1) \ F_i(2) \ \dots \ F_i(n)]$ corresponding to the bending displacements $h = [h_1 \ h_2 \ \dots \ h_n]$ were calculated by the analytical model by a genetic algorithm for comparison.

3.3.2. Dimensionless Data. To facilitate analysis, it is necessary to conduct dimensionless data processing on the original data before the comparison. When the target has visual characteristics, the data processing is as follows:

$$F_i^d(k) = \frac{F_i(k) - \min_{i \in N} F_i(k)}{\max_{i \in N} |F_i(k) - F^e(k)| - \min_{i \in N} |F_i(k) - F^e(k)|}, \quad (31)$$

where $F_i^d(k)$ is the $F_i(k)$ data processing results.

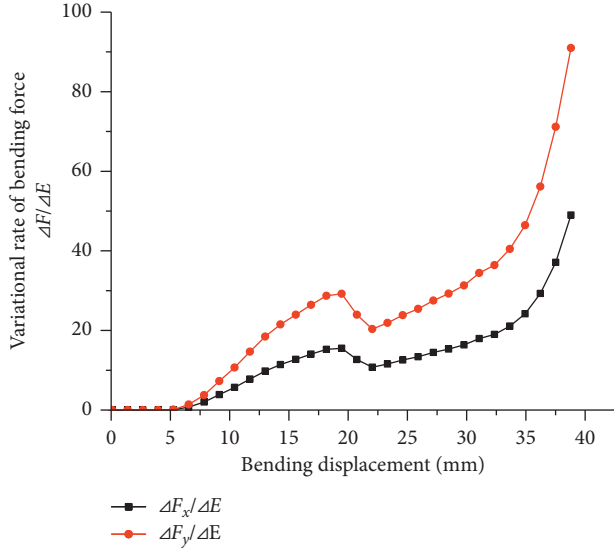


FIGURE 11: Effect of the rate plastic modulus on the bending load.

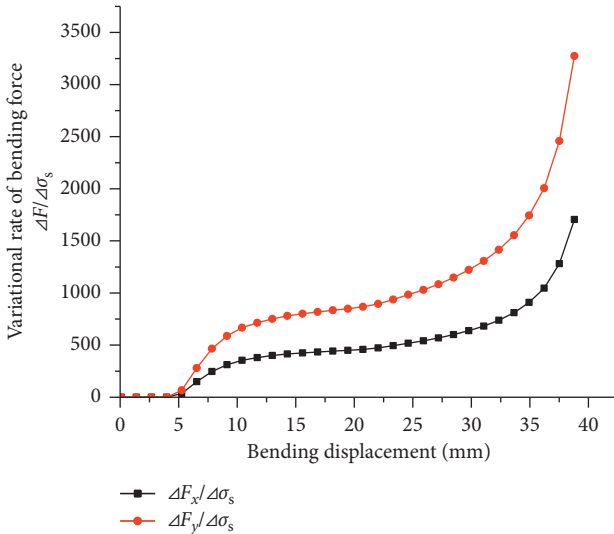


FIGURE 12: Effect of the rate yield strength on the bending load.

3.3.3. Gray Correlation Coefficient. The gray relational coefficients were used to measure the difference between the theoretical and experimental results. The gray relational coefficient $\xi_i(k)$ can be written as follows:

$$\xi_i(k) = \frac{\min_{i \in N} \min_{i \in N} F_i(k) + \rho \max_{i \in N} \max_{i \in N} |F^e(k) - F_i(k)|}{|F^e(k) - F_i(k)| + \rho \max_{i \in N} \max_{i \in N} |F^e(k) - F_i(k)|}, \quad (32)$$

where $\rho = 0.5436$.

3.3.4. Gray Relational Grade. The gray relational grade corresponding to each performance characteristic is computed, and the overall evaluation of the multiresponse characteristics is based on the gray relational grade, which is given by [18]:

$$r(F^e, F_i) = \frac{1}{n} \sum_{k=1}^n \lambda_k \xi_i(k). \quad (33)$$

A higher gray relational grade represents that the experimental result is closer to the ideally normalized value.

3.3.5. Gray Difference Degree. In the optimization design, the minimum value of the objective function is usually obtained, so the concept of gray difference degree is introduced [19]:

$$d_i = 1 - r(F^e, F_i). \quad (34)$$

Therefore, the above gray difference is used as the objective function of identification optimization:

$$f_{\text{object}} = \min [d_i(F^e, F_i)]. \quad (35)$$

Finally, the optimization model is constructed as follows:

$$\begin{aligned} & \text{design variable}(\sigma_s, E_p), \\ & \text{constraint condition} \begin{cases} \sigma_s^l \leq \sigma_s \leq \sigma_s^u, \\ E_p^l \leq E_p \leq E_p^u, \end{cases} \\ & f_{\text{object}} = \min [d_i(F^e, F_i)]. \end{aligned} \quad (36)$$

The relatively stable NLPQL (nonlinear programming by quadratic Lagrangian) algorithm is selected as the inversion optimization algorithm to solve the optimization model, which expands the objective function by the second-order Taylor series, linearizes the constraint condition, and obtains the next design point by solving the quadratic programming optimization problem. Finally, the plastic parameters, including the yield strength and plastic modulus, were identified by optimization.

3.4. Verification for Parameter Identification. To verify the reliability of the parameter identification technology, the material mechanical properties of X80 were calculated by the parameter identification technique described in 3.3 and compared with the results of the uniaxial tensile test in Table 2.

As seen from Table 2, the maximum relative error of the identification value is less than 4%. This satisfies the requirements.

4. Crimping Displacement Prediction

4.1. Springback Prediction Model. To predict the crimping displacement, a calculation model of the springback must be constructed by the analysis method. Thus, according to unloading laws, the curvature after springback can be obtained by

$$\frac{1}{\rho_T} = \frac{1}{\rho_\theta} - \frac{1}{\rho_\theta^e}. \quad (37)$$

The springback curvature can be expressed as follows:

TABLE 2: Comparison with identification and test.

Parameters	Identification	Test	Relative error (%)
Elastic modulus E (GPa)	203	210	3.3
Yield strength σ_s (MPa)	575	596	3.5
Plastic modulus E_p (MPa)	5702	5500	3.67

$$\frac{1}{\rho_\theta^e} = \frac{M_\theta}{EI}. \quad (38)$$

For the elastoplastic deformation wrapped stage, the bending moment can be calculated by equations (25) and (26). For the unwrapped stage in elastoplastic deformation, the bending moment can be calculated by equation (16). In addition, the differential equations can be established:

$$\frac{1}{\rho_\theta^e} = \frac{ds}{d\theta}. \quad (39)$$

When $M = M_{\max-e} = (1/6)\sigma_s t^2$, $\theta = \theta_p$, and $s = l_p$, the angle after springback $\theta = \theta_*$ can be obtained by solving the above differential equations. Then, we evaluate whether the crimping angle after springback satisfies the target value, and if this condition is satisfied, the predicted displacement is obtained. If not, the displacement is increased and recalculated until the criterion is satisfied.

To evaluate the precision of the springback analysis model, the crimping forming process is conducted by a hydropress in the plant. The forming force and displacement can be collected with a pressure sensor and a displacement sensor. Then, the comparison between measurement and calculation from the analytical model is shown in Figure 13.

As seen from Figure 13, the calculation results are in good agreement with the measurement results and their maximum relative error is 4.76%.

4.2. Application. In this study, a $\Phi 1219 \times 22 \times 12000$ mm large-diameter straight seam welded pipe was taken as an example. First, the elastic modulus E , yield strength σ_s , and plastic modulus E_p of the mechanical properties of the material were determined by tensile testing. Then, a #3 mold was used for crimping forming.

To verify the feasibility of precision forming technology for crimping, the crimping forming process was performed using different displacements: 23, 28, 33, 38, and 42 mm. The forming displacement can be obtained from the displacement sensor, and the crimping angle after springback was measured by three-coordinate measuring instruments. Finally, a comparison between the calculations and measurements is shown in Figure 14.

It can be seen from Figure 14 that the proposed precise forming technology can dynamically adjust the bending displacement in real time and effectively control the quality of crimping forming.

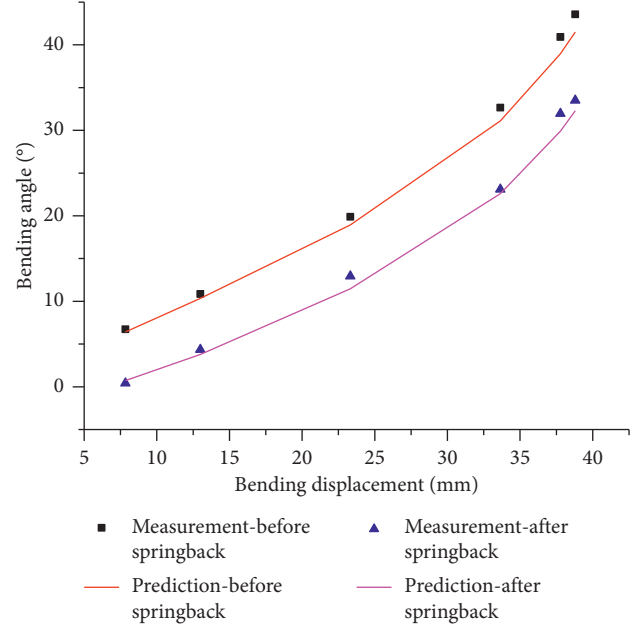


FIGURE 13: Verification with the bending angle.

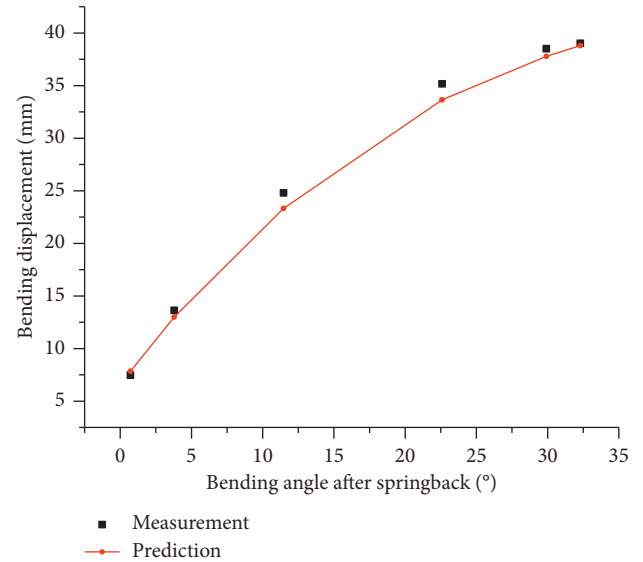


FIGURE 14: Verification with bending angle and bending displacement.

5. Conclusions

To calculate the springback considering the real-time variation of material parameters, the identification of material parameters was performed by an analytical model of crimping and the inverse optimization method. Then, the crimping displacement was predicted based on the springback model. The conclusions were as follows:

- (1) Three phases compose the whole crimping forming process: the elastic deformation stage, the unwrapped stage in elastoplastic deformation, and the wrapped stage in elastoplastic deformation. The

quantitative relationship between the bending displacement and bending force was calculated by an analytical model of crimping.

- (2) The elastic modulus has a significant effect on the bending force curve, and the initial segment of the bending force curve is approximately linear. The elastic modulus can be identified by the linear formula.
- (3) The yield strength and the plastic modulus have a significant effect on the plastic segment of the bending load curve, and the trends are to increase slowly and then rapidly. The plastic parameters, including the yield strength and plastic modulus, can be identified by the gray correlation method.
- (4) Precision forming technology for crimping was achieved by identification of the material parameters and by crimping displacement prediction technology.

Data Availability

The datasets supporting the conclusions of this article are included within the article.

Conflicts of Interest

The authors declare no conflicts of interest.

Authors' Contributions

Li-Feng Fan supervised the research and wrote the manuscript and the others assisted with sampling and laboratory analyses.

Acknowledgments

The authors thank Professor Ying Gao of Hebei University of Science and Technology for his critical discussion and reading during manuscript preparation. This study was supported by the National Natural Science Foundation of China (51761030) and the Inner Mongolia Natural Science Foundation of China (2019MS05081).

References

- [1] G. Palumbo and L. Tricarico, "Effect of forming and calibration operations on the final shape of large diameter welded tubes," *Journal of Materials Processing Technology*, vol. 164-165, no. 5, pp. 1089-1098, 2005.
- [2] L. Fan, Y. Gao, Q. Li, and H. Xu, "Quality control on crimping of large diameter welding pipe," *Chinese Journal of Mechanical Engineering*, vol. 25, no. 6, pp. 1264-1273, 2012.
- [3] J. Liu, K. Huang, and F. Ruan, "Effects of the parameters of prebending on O-forming of pipe in UOE process," *Journal of Plasticity Engineering*, vol. 12, no. 3, pp. 71-75, 2005, in Chinese.
- [4] M. D. Herynk, S. Kyriakides, A. Onoufriou, and H. D. Yun, "Effects of the UOE/UOC pipe manufacturing processes on pipe collapse pressure," *International Journal of Mechanical Sciences*, vol. 49, no. 5, pp. 533-553, 2007.
- [5] T. Zou, G. Wu, D. Li, Q. Ren, J. Xin, and Y. Peng, "A numerical method for predicting O-forming gap in UOE pipe manufacturing," *International Journal of Mechanical Sciences*, vol. 98, no. 5, pp. 39-58, 2015.
- [6] L. Hong, "Prebending process of longitudinal submerged arc welding production line," *Welding Pipe and Tube*, vol. 29, no. 1, pp. 55-57, 2006, in Chinese.
- [7] Z. Xie and J. Xia, "Prebending process parameter design of longitudinal submerged arc welding pipe," *Welding Pipe and Tube*, vol. 30, no. 3, pp. 52-54, 2007, in Chinese.
- [8] S. Zhao, *Study on Quality Control Strategy and Simulation System Development of UOE Pipe Forming*, Yanshan University, Qinhuangdao, China, 2010, in Chinese.
- [9] Q. Yang, *Springback Analytic and Process Parameters Optimization of Plate Edge Preflex for the Forming of Large Diameter Longitudinal Seam Welded pipe*, Yanshan university, Qinhuangdao, China, 2012, in Chinese.
- [10] P.-A. Eggertsen and K. Mattiasson, "On constitutive modeling for springback analysis," *International Journal of Mechanical Sciences*, vol. 52, no. 6, pp. 804-818, 2010.
- [11] S. Sumikawa, A. Ishiwatari, J. Hiramoto, and T. Urabe, "Improvement of springback prediction accuracy using material model considering elastoplastic anisotropy and Bauschinger effect," *Journal of Materials Processing Technology*, vol. 230, pp. 1-7, 2016.
- [12] W. Julsri, S. Suranuntchai, and V. Uthaisangsuk, "Study of springback effect of AHS steels using a microstructure based modeling," *International Journal of Mechanical Sciences*, vol. 135, pp. 499-516, 2018.
- [13] L. Komgrit, H. Hamasaki, R. Hino, and F. Yoshida, "Elimination of springback of high-strength steel sheet by using additional bending with counter punch," *Journal of Materials Processing Technology*, vol. 229, pp. 199-206, 2016.
- [14] Z. Wang, Q. Hu, J. Yan, and J. Chen, "Springback prediction and compensation for the third generation of UHSS stamping based on a new kinematic hardening model and inertia relief approach," *The International Journal of Advanced Manufacturing Technology*, vol. 90, no. 1-4, pp. 875-885, 2017.
- [15] J. H. Kim, D. Kim, F. Barlat, and M.-G. Lee, "Crystal plasticity approach for predicting the Bauschinger effect in dual-phase steels," *Materials Science and Engineering: A*, vol. 539, pp. 259-270, 2012.
- [16] L. Fan, Y. Gao, Q. Li, and H. Xu, "Designing for robustness on crimping of large diameter welding pipe," *China Mechanical Engineering*, vol. 26, no. 8, pp. 1112-1116, 2015, in Chinese.
- [17] J. Yan, L. Fan, and J. Yun, "Stochastic analysis of crimping quality of large diameter welding pipe," *Mechanical Science and Technology for Aerospace Engineering*, vol. 34, no. 12, pp. 1880-1884, 2015, in Chinese.
- [18] S. Yarmohammadisatri, M. H. Shojaeefard, A. Khalkhali, and S. Goodarzi, "Sensitivity analysis and optimization of suspension bushing using Taguchi method and grey relational analysis," *International Journal of Vehicle Mechanics and Mobility*, vol. 57, no. 6, pp. 855-873, 2019.
- [19] A. B. Shinde and P. M. Pawar, "Multi-objective optimization of surface textured journal bearing by Taguchi based grey relational analysis," *Tribology International*, vol. 114, pp. 349-357, 2017.

Research Article

Dynamic Behavior of Self-Piercing Riveted and Mechanical Clinched Joints of Dissimilar Materials: An Experimental Comparative Investigation

Yulong Ge  and Yong Xia 

State Key Laboratory of Automotive Safety and Energy, School of Vehicle and Mobility, Tsinghua University, Beijing 100084, China

Correspondence should be addressed to Yong Xia; xiayong@tsinghua.edu.cn

Received 28 June 2019; Revised 10 August 2019; Accepted 27 August 2019; Published 12 September 2019

Guest Editor: Rezwanul Haque

Copyright © 2019 Yulong Ge and Yong Xia. This is an open access article distributed under the Creative Commons Attribution License, which permits unrestricted use, distribution, and reproduction in any medium, provided the original work is properly cited.

The present work compares the dynamic effect of a self-piercing riveted (SPR) joint with that of a mechanical clinched joint having the dissimilar materials combination. The substrates used in this investigation are aluminum alloy AA5182-O and deep drawing steel DX51D+Z. The static and dynamic behaviors and the failure modes of the SPR and clinching joints are characterized by lap-shear, cross-tension, and coach-peel tests. The influence of the strain-rate-dependent mechanical behavior of the substrates on the joints is examined; this can help improve prediction of the energy absorption of the joints under impact loading. Considering the realistic baking process in a painting shop, the deforming and hardening effects on the SPR and the clinched joints induced by baking are also studied. The specimens are heated to 180°C for 30 min in an oven and then cooled down in air. The SPR and the clinched joints before and after the baking process are compared in terms of the mechanical behavior.

1. Introduction

Currently, manufacturers of lightweight vehicles not only pursue more excellent structural performance of materials but also put effort into selecting or developing reliable technologies for joining dissimilar materials to achieve sufficient structural stiffness and crashworthiness. Among the combinations of dissimilar materials, joints with steels and aluminum alloys are the most prevalent ones applied to achieve viable and sustainable products. Mechanical, chemical, thermal, or hybrid joining processes can be selected to connect steel and aluminum alloy. The process could become complicated considering factors such as manufacturing conditions and cost. Self-piercing riveting (SPR) and mechanical clinching have many advantages and are quite suitable for manufacturing steel-aluminum joints. SPR demonstrates good mechanical and fatigue strength, while clinching has a lower manufacturing cost.

Suitable and cost-efficient mechanical joining technologies must be developed to utilize the weight reduction

potential of steels combined with aluminum alloys and thus enable further affordable weight reduction in mass vehicle production. Mechanical joining technologies like SPR and mechanical clinching have been established in many automotive productions for joining multimaterial or light-metal car bodies, as these cold joining processes can be applied to joining dissimilar metals [1, 2].

SPR is used to join two or more sheets of materials by driving a rivet piercing through the top sheet or the top and middle sheets and partially piercing and locking into the bottom sheet to form a mechanical joint. During the SPR process, the spreading of the rivet skirt is guided by a suitable die, and the punched slug from the top sheet and the middle sheet is embedded into the rivet shank [3]. During the SPR process, the characteristic curve (force-displacement curve) can reveal the relationship between residual stress and its physical occurrence [4].

The mechanical clinching process is a method of joining sheet metal by localized cold forming of materials, which is also capable of connecting three layers of sheets [5]. The result

is an interlocking friction joint between two and more layers of material formed by a punch into a special die [6]. The die radius, depth, and die groove shape can affect the joinability, and the die groove width is the most important parameter affecting the material flow effect of the clinching process [7]. The analysis of clinched joints of DX51 and DP600 steels shows that increasing the joint diameter and forming force results in increased strength [8, 9]. In addition to round clinching, joints of square clinching tools are also used with orientation angles of 0° or 90° relative to the shearing load [10].

Comparing the production costs of these joining processes, clinching shows a lower running cost in the automotive industry. However, the mechanical characteristics of the joints are very different [11]. SPR joints have superior static and fatigue properties, while clinched joints also present favorable fatigue performance [12]. Higher strength is always observed in lap-shear testing compared with cross-tension testing [13]. As part of structural crashworthiness, dynamic tests are needed to study the dynamic behaviors of joints. Dynamic joint strength evaluation procedures have been introduced, and the dynamic strength data for SPR joints of dissimilar metals have been measured. It has been reported that the high speeds during dynamic tests can increase the joint strength and decrease the dissipated energy of steel-aluminum steels [14]. In addition, an experimental study on the behavior of SPR joints between aluminum AlMg3.5Mn and AlMg3.0Mn materials under dynamic loading conditions using a split Hopkinson tension bar in both the shearing and pulling-out direction was performed, showing a negligible rate effect on the joint [15]. Various failure modes may be observed in SPR joints. The three primary ones are rivet head pullout, rivet tail pullout, and sheet tearing [16]. Conversely, although there are insufficient studies on the dynamic behavior of clinched joints, they show a comparable energy absorption on the aluminum single-hat structure impact condition to the spot-welded joint with a suitable clinching process [17].

In this study, an aluminum alloy AA5182-O and mild steel DX51D+Z material combination is used. Exemplary results from lap-shear, cross-tension, and coach-peeling tensile tests are shown. The static and dynamic behaviors and the failure modes of both joints are characterized. In addition, as an increase in temperature can lead to a reduction in the strength of aluminum-magnesium alloys such as AA5182 [18], baked specimens are tested and compared to nonbaked ones in terms of their mechanical behavior to study the baking effect.

2. Experimental Procedure

Aluminum alloy AA5182-O and mild steel DX51D+Z are conventionally used for automobile body panels. The mechanical properties of the aluminum alloy and steel sheets are given in Table 1. The isotropic hardening law can be expressed using Swift's law:

$$\sigma = K \times (\varepsilon_0 + \varepsilon_p)^n, \quad (1)$$

TABLE 1: Mechanical properties of AA5182-O and DX51.

	AA5182-O	DX51D+Z
E (MPa)	6800	207000
ν	0.34	0.3
$\sigma_{0.2}$ (MPa)	90.7	165.4
K	506.9	473.2
ε_0	0.004	0.0055
n	0.302	0.229

where σ is the stress and ε_p is the plastic strain. K , ε_0 , and n are material constants. The thicknesses of AA5182-O and DX51 were 0.85 mm and 1.20 mm, respectively, in this study.

The cross-sectional shapes of the joints are shown in Figure 1. The quality of an SPR joint from the cross-sectional perspective is primarily characterized in terms of the amount of mechanical interlock, known as rivet flaring, which is in the range of 300~400 μm in this case. The clinched joint is characterized by the following parameters [7]: the axial thickness of the sheets (707 μm), the thinning of the upper sheet (576 μm), and the clinch lock (121 μm).

Lap-shear, cross-tension, and coach-peel test specimens used to determine static strength are illustrated in Figure 2. In the lap-shear test, shear force is the main load induced on the joint, and the deformation behavior is limited to intrinsic deformation of the joint. Cross-tension specimens are used for normal direction tests. In addition, coach-peel tests were performed. DX51 is on the top, and AA5182-O is on the bottom.

AA5182-O material sheets for automotive BIW applications show softening behavior with respect to the pre-strained sheets after the paint bake cycle. The specimens were placed in an oven at 180°C for 30 min and tested under static conditions to determine the influence of the baking process on the mechanical behavior of the joints.

A universal testing machine (Zwick Z020) and hydraulic testing machine (Zwick H5020) were used to conduct the static and dynamic tests, respectively. The global loading speeds were 0.083×10^{-3} m/s, 0.1 m/s, and 2 m/s. The digital image correlation method (VIC-2D) was adopted for deformation measurement. The gauge length of lap-shear and coach-peel specimens was 50 mm, and the displacements measured in cross-tension tests were the separative displacement of the fixtures, which are regarded as rigid.

The substrate materials have different responses to the strain rate effect. Previous studies have reported that a negative strain rate dependence of the material strength has been observed for Al-Mg alloys at a quasistatic strain rate, but there is a positive strain rate dependence for a high strain rate [19]. The yielding strain rate of DX51D+Z could increase by approximately 50% from static to intermediate strain rates [20].

Tests for lap-shear and coach-peel specimens under loading speeds of 0.1 m/s and 2 m/s were also performed to understand the mechanical behavior and failure modes of joints using a hydraulic high-speed testing machine. All tests were repeated three times to guarantee reproducibility, and the median result is shown.

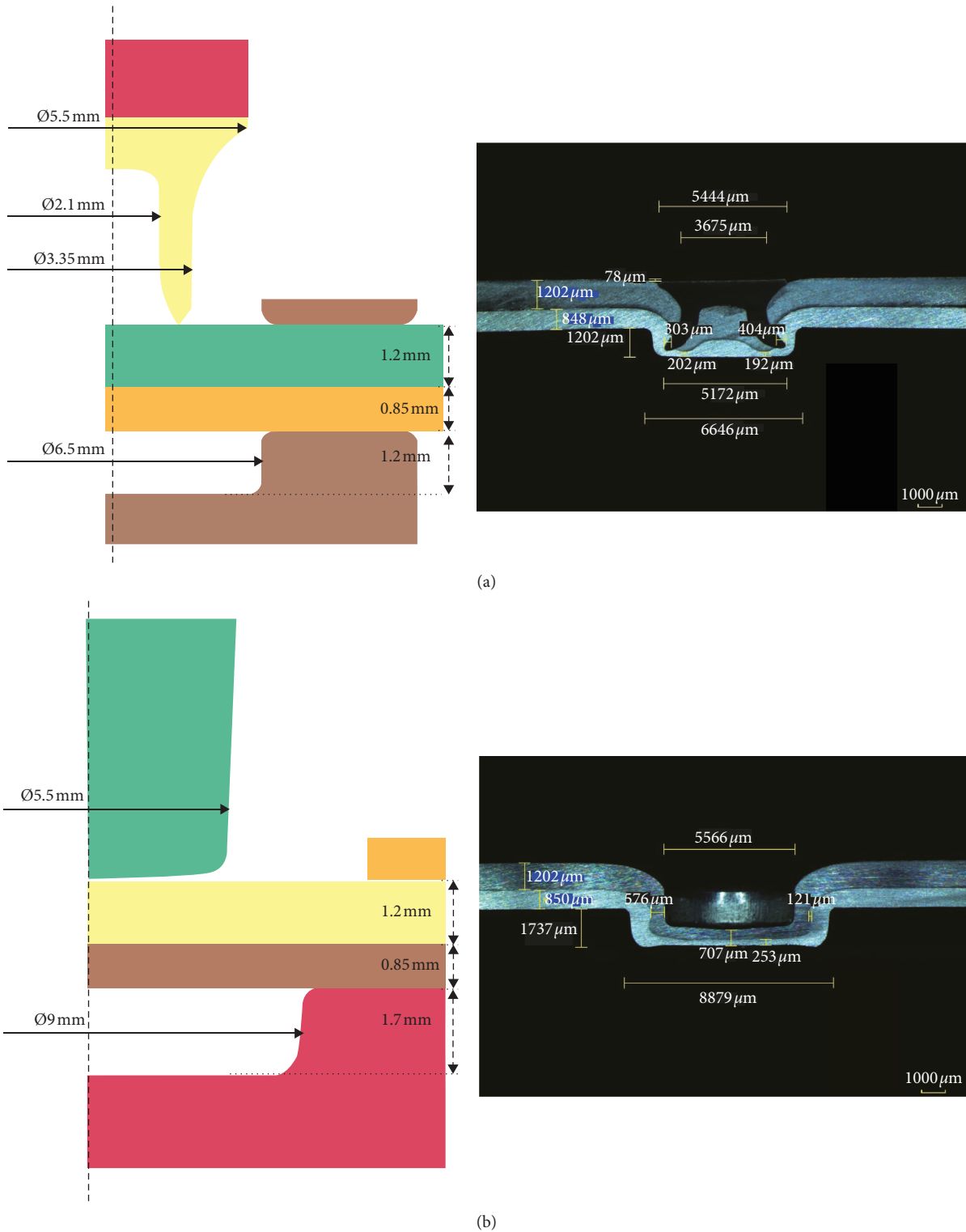


FIGURE 1: Tool geometries and cross-sectional shapes of (a) self-piercing joint and (b) mechanical clinched joint.

3. Results of Static and Dynamic Tests

3.1. *Static Test.* The force-displacement curves and failures for static lap-shear tests of joints obtained by both joining processes are illustrated in Figure 3. The maximum loads and stiffnesses, which are the slope of the linear stage, for the SPR

joint and the clinched joint are similar. The elongation, however, is quite different. The deformation process of the SPR joint can be divided into three phases: elastic deformation, failure initiation, and failure extension. The rivet helps to prevent the steel sheet from being pulled out. As an alternative, the rivet moves in the aluminum sheet, which

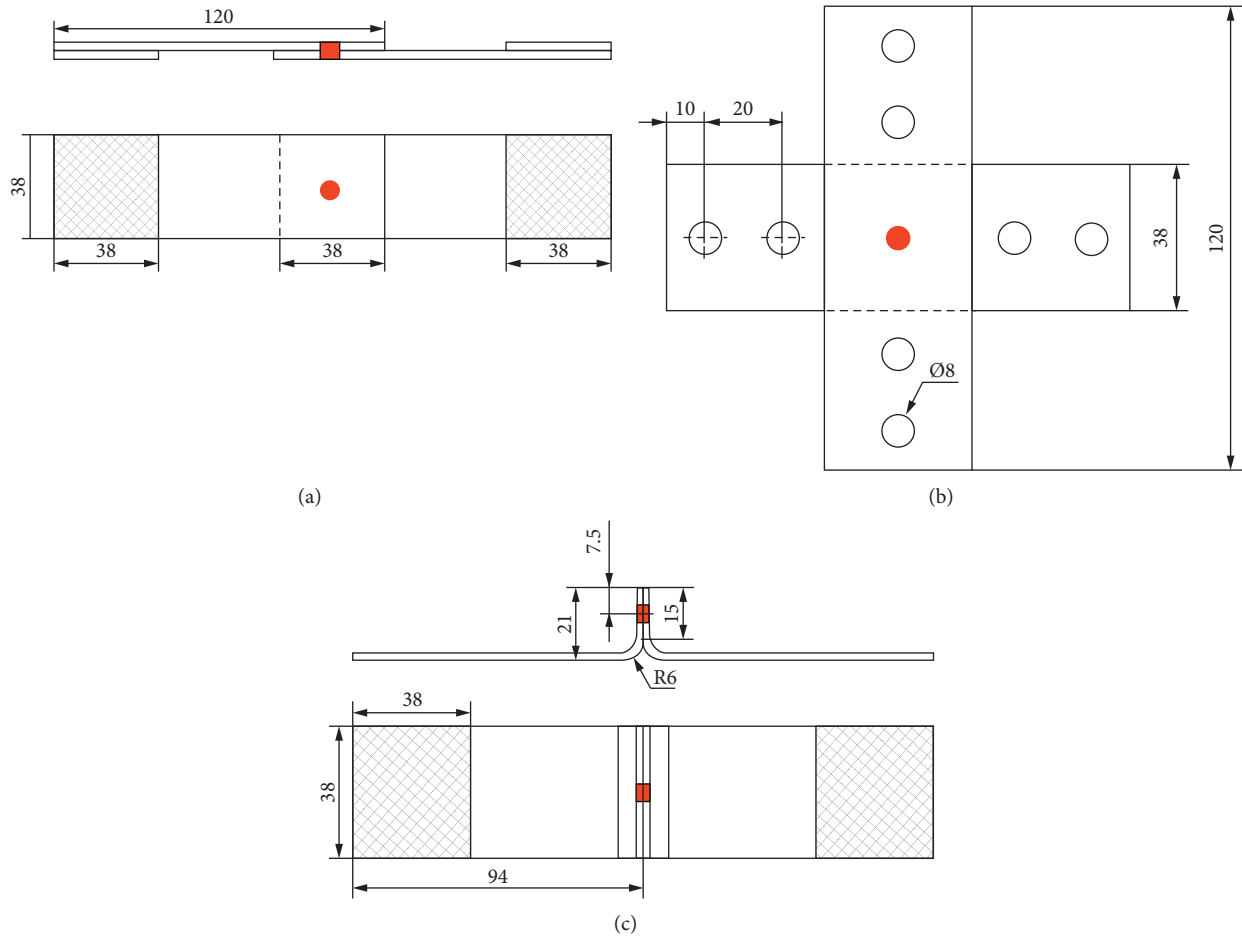
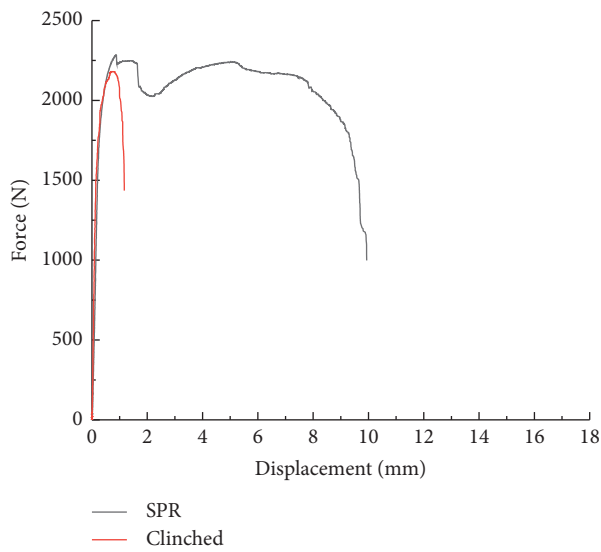


FIGURE 2: Specimens of joints for testing: (a) lap-shear, (b) cross-tension, and (c) coach-peel.



(a)

(b)

FIGURE 3: Continued.



(c)

FIGURE 3: Static lap shear tests: (a) force-displacement curves, (b) material fracture failure mode of the SPR joint, and (c) pulling-out failure mode of the clinched joint at 0.083×10^{-3} m/s.

tears it apart and leads to a plateau in load before total failure. For the clinched joint, deformation breaks the geometry of the interlock, so that the load decreases rapidly. They have similar peak force-bearing capabilities, but the total energy dissipated of a single SPR joint is 10 times that of a clinched joint.

In these tests, as the strength of steel sheet is higher than that of the aluminum one, steel sheets on the top are bent up and large local deformation occurs on the button of the aluminum sheets, which results in joint failure. In the SPR joint, fracture can be found on the aluminum sheet from the button to the edge, bottom sheet tearing mode, which is not a common failure type in similar materials' joints. On the contrary, no large deformation occurs out of the button area in the clinched joint. The steel sheet is pulled out from the interlock on the aluminum sheet, and there is no material fracture on either sheet.

The force-displacement curves and failures for static cross-tension tests of the joints are illustrated in Figure 4. Unlike the lap-shear tests, the elongation and maximum loads are distinct, although the stiffnesses of the two joints are similar. The clinched joint has approximately 60% of the ultimate strength and of the SPR joint.

In terms of failure, pull-out is the dominant mode in both joints. Severe local doming occurs on the steel and aluminum sheets, and the strength of the steel sheets and rivets is higher, which leads to the expansion of clinched region on the bottom sheet. The interlocks in both joints are unbuttoned, so the steel sheets/rivets are plugged out, and no obvious material damage is found in either joint.

Similar mechanical behaviors are also observed in the static coach-peel tests, as the joints in these two forms primarily undergo a normal direction force, as shown in Figure 5. The deformation process of these aluminum-steel joints is more complicated. As the aluminum sheet of DX51 is stronger and thicker, when it is flattened by the moment, the bottom sheet of AA5182-O is rolled up in the joining regions, rather than flattened. This leads to sliding out of the interlocks of SPR and clinched joints and a pull-out failure mode. On the other hand, comparing the curves of two joints, the imbedded rivet tail can help to prevent the rivet from peeled out. Hence, a plateau in loading arises in the SPR joint before failure and the clinched joint fails right after peak loading.

From these tests, it can be seen that in the AA5182-O and DX51 joints under static conditions, the stiffness of the two joints is similar, but the toughness of the SPR joint

is remarkably higher than that of the clinched joint. The normal strengths of these joints are much lower than their shear strengths. It is worth mentioning that plateaus appear when the loading reaches the peak of SPR joints under lap-shear and coach-peel conditions. This indicates that when the button begins to separate, the rivet can still help to bear the loading, but the clinched joint fails rapidly. Tail pull-out is the main failure mode in the cross-tension and coach-peel tests, which implies that it is better to prevent the joints from being exposed to a normal direction load.

3.2. Dynamic Test. Dynamic tests were conducted under global loading speeds of 0.1 and 2 m/s. Figure 6 shows the force-displacement curves and failure modes of the SPR joint at the two speeds and comparison to the quasi-static one. The stiffness and maximum strength of the joint are not significantly influenced by dynamic effects. Conversely, the ductility decreases from the 0.083×10^{-3} m/s condition to the 0.1 m/s condition and then remains at a similar value when the speed is increased to 2 m/s. The loading plateau disappears under dynamic conditions, so that a trapezoidal mechanical response degenerates to a triangular response. The total energy absorption capability decreases by more than 50%, from approximately 21 to 10 J.

Although the bottom sheet tearing is observed as the dominate failure mode, the modification of the curves could be the result of different dynamic behaviors with respect to the substrate materials. Generally, steels are more sensitive to strain rate effects than aluminum alloys, which contributes to the loss of load-bearing capability of the rivet tail. This leads to a transition of the deformation patterns on steel and aluminum sheets. At 0.083×10^{-3} m/s, the aluminum sheet remains flat during the tensioning process, and the steel sheet is bent. Conversely, as the yielding stress increases because of the strain rate effect, the steel sheet remains flat, while the aluminum sheet is bent, after which material failure occurs. The bent bottom sheets under dynamic conditions lead to a larger loading angle like peeling and a rapid failure.

Considering the coach-peel tests, Figure 7 demonstrates the mechanical behaviors of SPR joints at three test speeds. The static strength and stiffness are higher than the dynamic values, while the toughness is lower, which could also be the result of differences in the strain rate effect between substrate

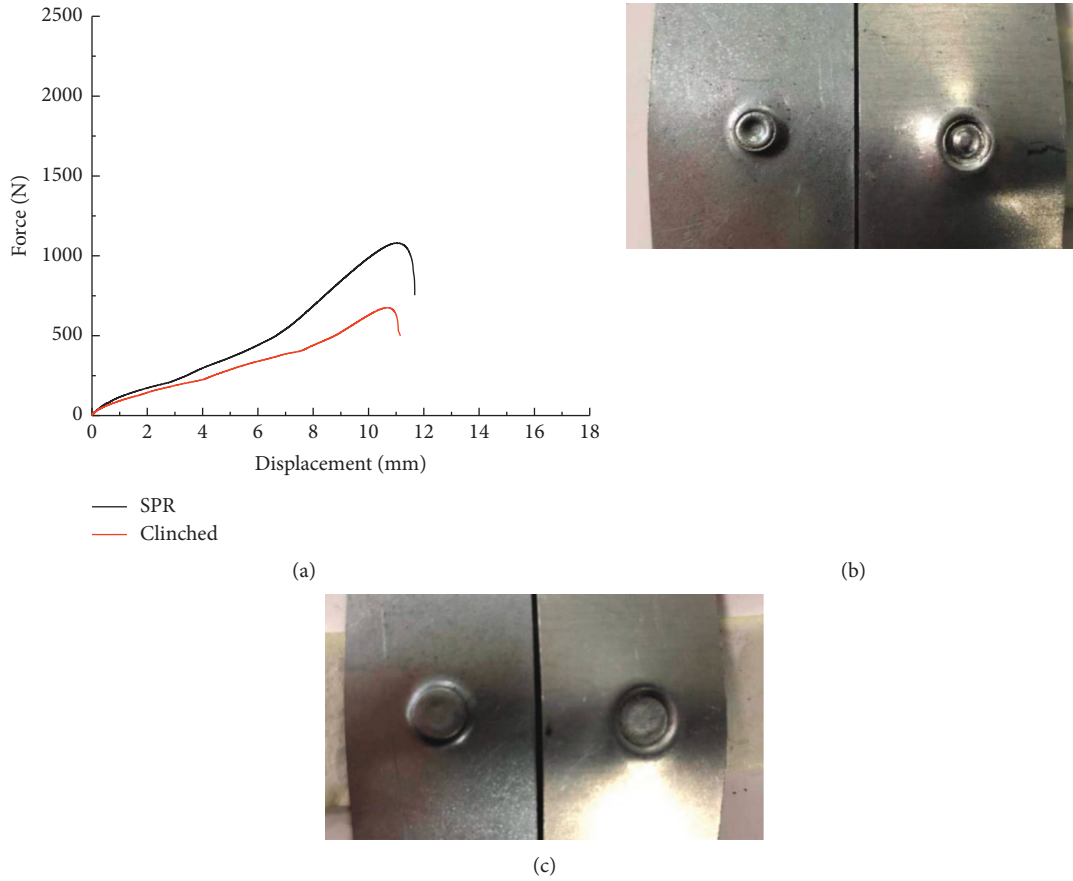


FIGURE 4: Static cross-tension tests: (a) force-displacement curves, (b) pulling-out failure modes of SPR joint, and (c) clinched joint at 0.083×10^{-3} m/s.

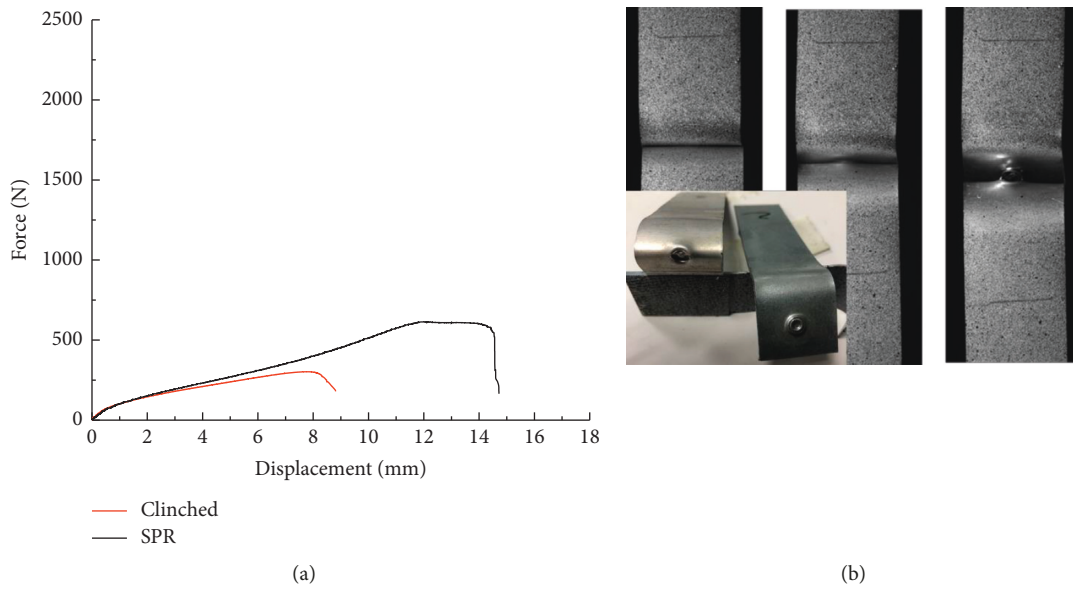


FIGURE 5: Continued.

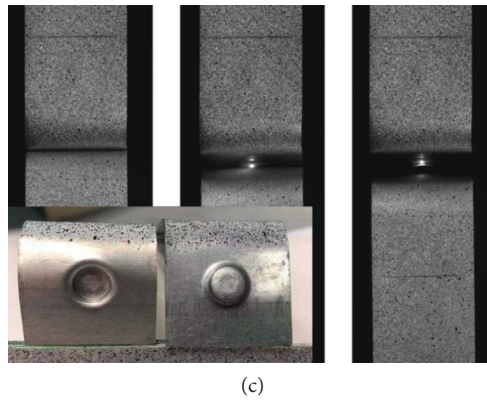


FIGURE 5: Static coach-peel tests: (a) force-displacement curves, (b) deformation process of SPR joint, and (c) clinched joint at 0.083×10^{-3} m/s.

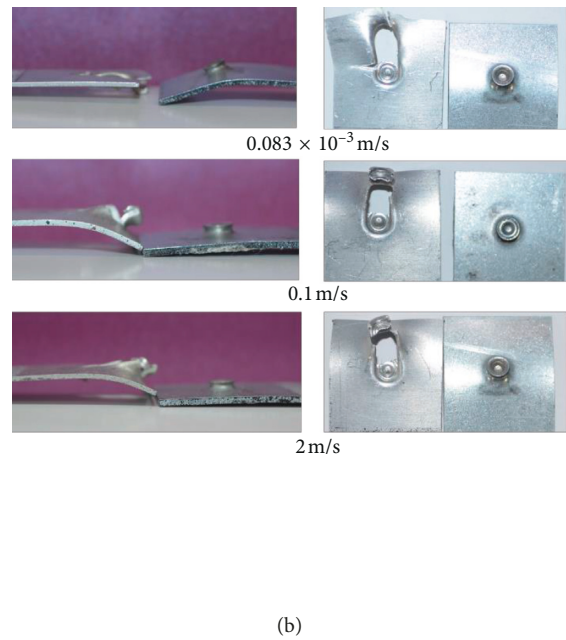
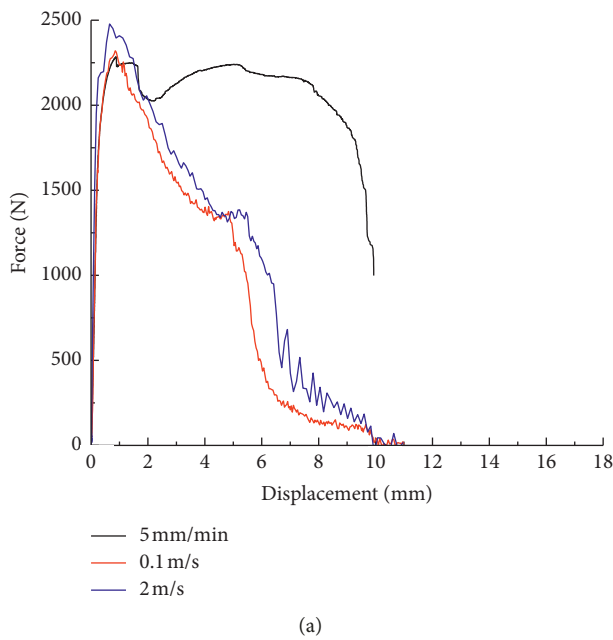


FIGURE 6: Dynamic lap-shear tests of SPR joints: (a) force-displacement curves and (b) failure modes at three speeds.

materials. As the yielding stress increases, the deformation of the steel sheet is delayed, so that the stiffness of the specimen is more dependent on the bending stiffness of the aluminum sheet, which decreases. The failure modes at the three speeds are all unbuttoning without material fracture on either steel or aluminum sheets. The static energy absorption is approximately 5.5 J, and the dynamic absorption is approximately 5.4 J, which indicates that although the mechanical behavior is influenced by the loading speed for coach-peel specimens, the energy absorption capability is not.

The dynamic response of a clinched joint to shear loading is different from that of an SPR joint. As shown in Figure 8, although the stiffness is not sensitive to the loading speed, the maximum strength and ductility increase with the loading speed. The distortion of interlocks leads to unbuttoning and pull-out failure mode of the joints at all three speeds. The deformation pattern of the steel and aluminum

sheets is also similar; that is, the steel sheet is bent, and the aluminum sheet remains flat. However, the local doming on the aluminum sheet is enlarged. This helps prevent the button from being pulled out. It could be a result of the earlier deformation of aluminum under dynamic conditions. It is noteworthy that although the strength and ductility are enhanced by the dynamic effect, the energy absorption of clinched joints exposed to lap-shear condition is much less than that of the SPR joints, which are approximately 2.2 J for the static condition, 3.5 J for 0.1 m/s, and 5 J for 2 m/s.

Correspondingly, the clinched joint under coach-peel condition is enhanced by the loading speed. Both the maximum strength and ductile are enlarged. The total energy absorption capability increases from 1.8 (5 mm/min) to 1.9 J under 0.1 m/s and 2.2 J under 2 m/s, as shown in Figure 9. Although the mechanical responses are different, the deformation patterns under three speeds are quite the

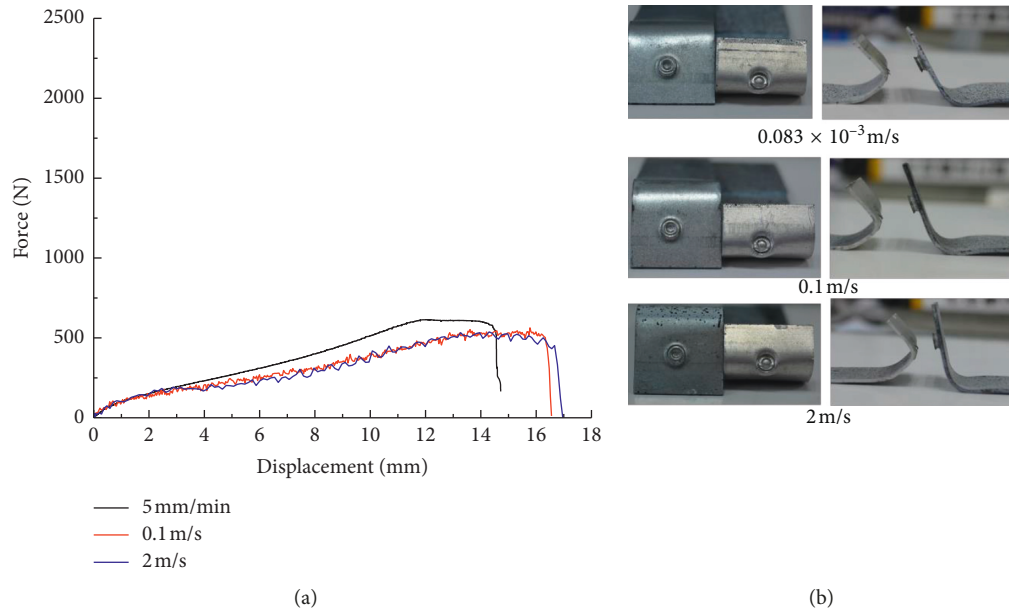


FIGURE 7: Dynamic coach-peel tests of SPR joints: (a) force-displacement curves and (b) failure modes at three speeds.

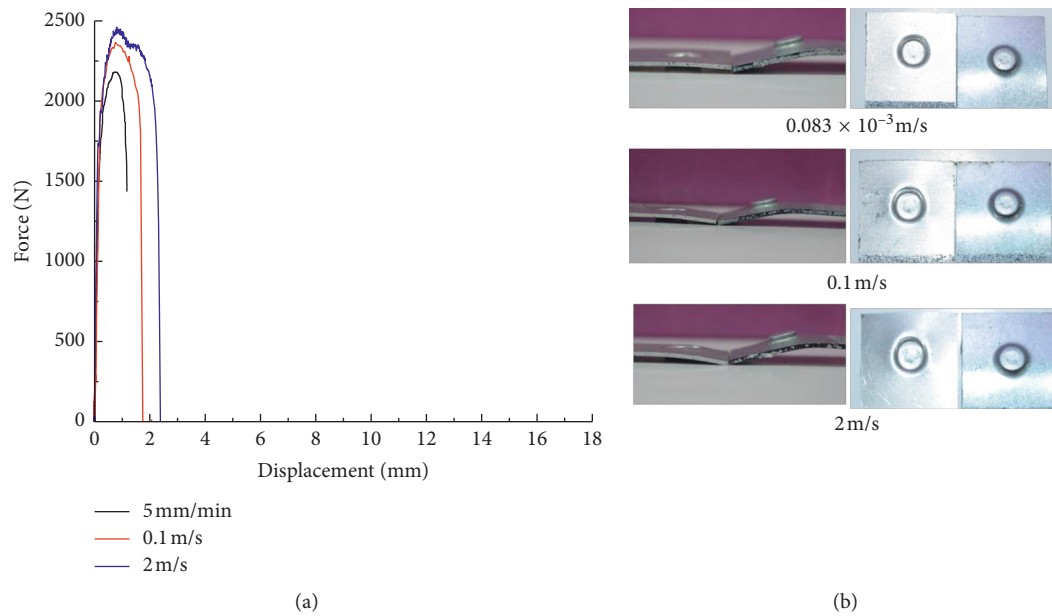


FIGURE 8: Dynamic lap-shear tests of clinched joints: (a) force-displacement curves and (b) failure modes at three speeds.

same. The steel sheet deforms little and the aluminum sheet is bent which results in the unbuttoning and pull-out failure. The curvature and distortion of the button is much less than the SPR ones. It implies that the significant dynamic effect of clinched joints under coach-peel condition could be the result of dynamic friction between the sheets.

To conclude, both joints of DX51 and AA5182-O combination under shear and normal load conditions have dynamic effects. However, the dynamic effects perform quite conflicting. The SPR joint tends to be weakened and the clinched joint tends to be strengthened by the effect due to

the different strain rate effects of substrate materials and dynamic interface contacts.

4. Results of Baked Joint Tests

AA5182-O attains its strength through work hardening and exhibits softening during the paint bake cycle, which is very likely to occur for BIW, as shown in Figure 10. Because large plastic deformation occurs in both SPR and clinching joining processes, it can lead to mechanical modification in the present material combination.

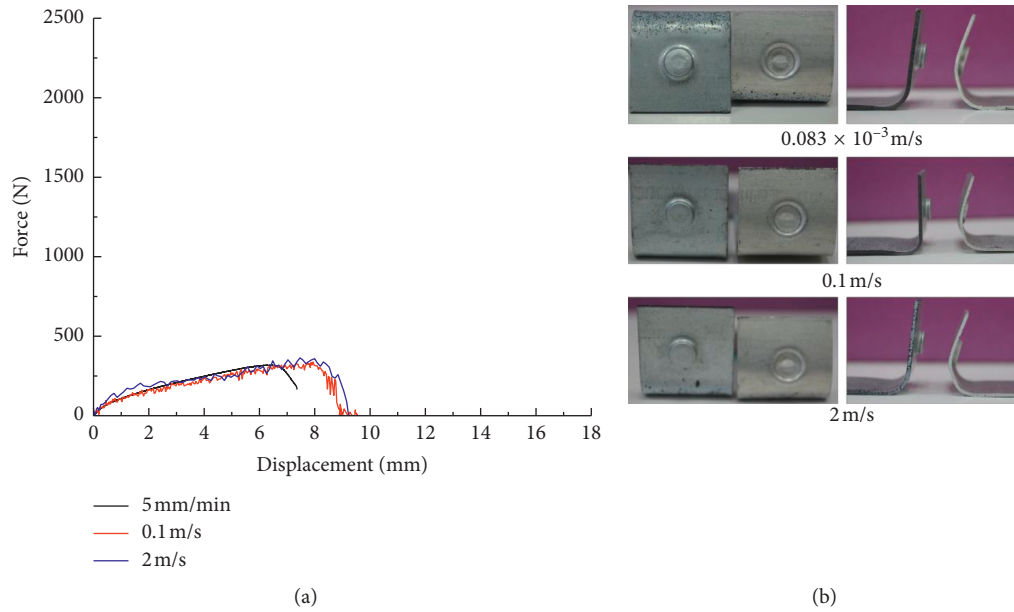


FIGURE 9: Dynamic coach-peel tests of clinched joints: (a) force-displacement curves and (b) failure modes at three speeds.

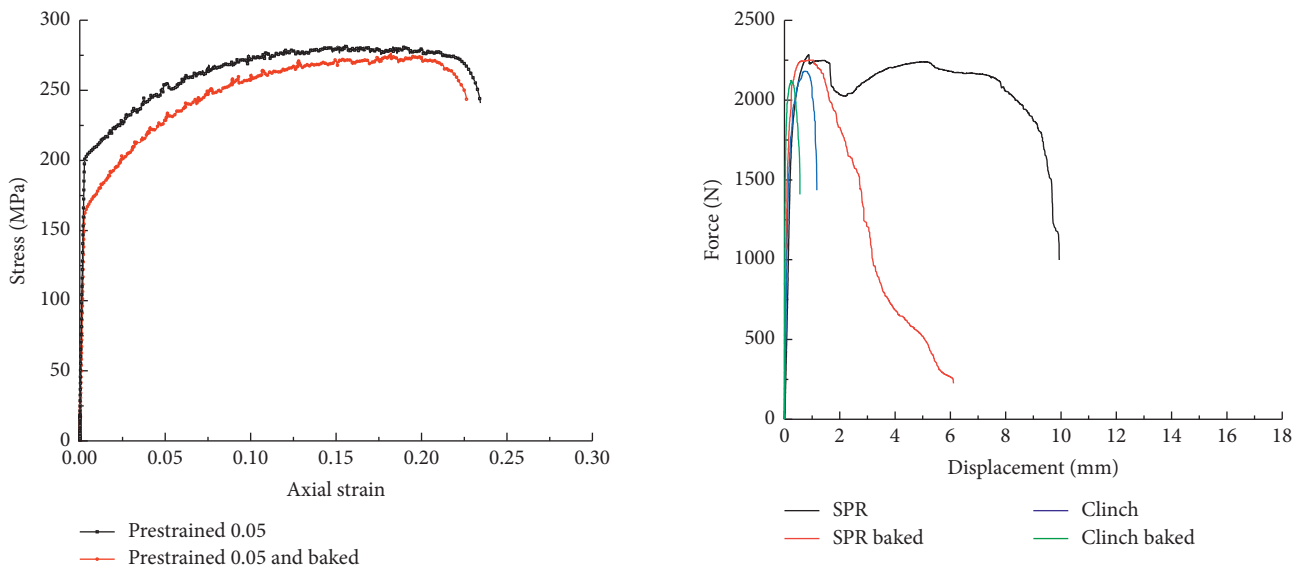


FIGURE 10: Quasistatic stress-strain curves of baked AA5182-O at 0.05 plastic deformation.

FIGURE 11: Comparison of lap-shear tests of SPR and clinched joints before and after the baking process at 0.083×10^{-3} m/s.

Figure 11 illustrates the force-displacement curves of lap-shear tests of SPR and clinched joints before and after the baking process. Both SPR and clinched joints have a higher stiffness and similar strength. Meanwhile, the ductility of the joints significantly decreases after baking, by up to 60%.

The cross-tension tests results demonstrate very different baking effect on the joints, as shown in Figure 12. The stiffness, strength, and ductility of all joints are quite similar. The joints' mechanical behavior in the normal direction is not sensitive to the baking softening of the AA5182-O bottom sheets.

In terms of coach-peel tests, completely converse responses to the baking process appear, compared with the lap-shear tests, as shown in Figure 13. The stiffness and maximum strength decrease after baking. The ductility, however, is less influenced by baking.

The test results indicate that both SPR and clinched joints of AA5182-O and DX51 suffer from the baking process. The baking effect, however, is loading condition-dependent and affects the specimens differently. Table 2 demonstrates the summary of the test results.

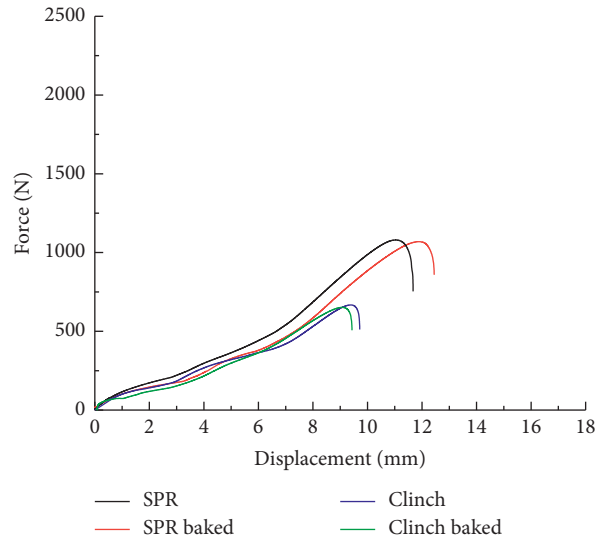


FIGURE 12: Comparison of cross-tension tests of SPR and clinched joints before and after the baking process at 0.083×10^{-3} m/s.

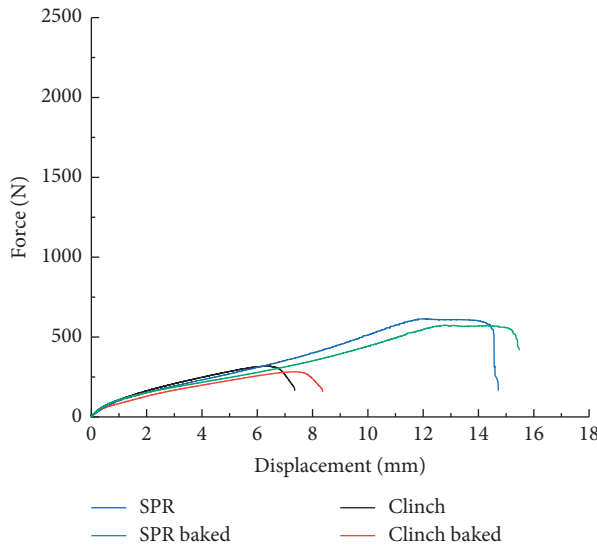


FIGURE 13: Comparison of coach-peel tests of SPR and clinched joints before and after the baking process at 0.083×10^{-3} m/s.

TABLE 2: Test result summary (units: speed m/s, force (N), and energy (J)).

Test speed	SPR		SPR baked		Clinch		Clinch baked	
	Peak force	Total energy absorption	Peak force	Total energy absorption	Peak force	Total energy absorption	Peak force	Total energy absorption
<i>Lap-shear</i>								
0.083×10^{-3}	2280	21.0	2251	7.7	2180	2.1	2123	1.5
0.1	2320	10.1	—	—	2366	3.5	—	—
2	2477	11.9	—	—	2461	5.1	—	—
<i>Coach-peel</i>								
0.083×10^{-3}	614	5.5	574	5.4	302	1.8	282	1.6
0.1	536	5.4	—	—	322	1.9	—	—
2	524	5.4	—	—	350	2.2	—	—
<i>Cross-tension</i>								
0.083×10^{-3} m	1180	5.9	1069	6.1	675	3.1	652	2.9

5. Conclusions

Experiments on SPR and mechanical clinched joints of AA5182-O and DX51 with various loading directions, speeds, and heat treatments were realized. The energy absorption of SPR joints is much higher under all conditions. The dynamic and baking effects on the mechanical behaviors of these two joining methods were compared.

- (i) The failure modes of SPR joints of dissimilar materials are direction-sensitive. Substrate material failure on aluminum is the primary mode under lap-shear conditions, and tail pulling-out dominates the cross-tension and coach-peel conditions. Clinched joints commonly fail by pulling-out, where the steel sheet separates from the bottom sheet.
- (ii) Dynamic effects on joints of dissimilar materials are loading condition-dependent. The strength of the two joints under lap-shear conditions increases with increasing loading rate. However, the dissipated energy of the SPR joint decreases because of the loss of load-bearing capability of the rivet tail, and that of the clinched joint increases. Under the coach-peel condition, the strength of the SPR joint decreases with increasing loading rate and the dissipated energy stays the same. However, both strength and the total energy absorption capability of the clinched joint increase under dynamic conditions.
- (iii) The baking process significantly affects the mechanical behavior of SPR and clinched joints and is loading direction-dependent. Both joints are weakened under lap-shear and coach-peel conditions, but the baking process has a negligible influence under cross-tension conditions.

Data Availability

The experimental data used to support the findings of this study are included within the article.

Conflicts of Interest

The authors declare that there are no conflicts of interest regarding the publication of this paper.

Acknowledgments

This was sponsored by the Key D&R Program of China under contract no. 2016YFB0101606. The author would like to acknowledge the staff at Suzhou Automotive Research Institute of Tsinghua University (TSARI) for providing technical support in conducting experiments.

References

[1] X. He, I. Pearson, and K. Young, "Self-pierce riveting for sheet materials: state of the art," *Journal of Materials Processing Technology*, vol. 199, no. 1–3, pp. 27–36, 2008.

- [2] K. Martinsen, S. J. Hu, and B. E. Carlson, "Joining of dissimilar materials," *CIRP Annals—Manufacturing Technology*, vol. 64, no. 2, pp. 679–699, 2015.
- [3] D. Li, A. Chrysanthou, I. Patel, and G. Williams, "Self-piercing riveting—a review," *The International Journal of Advanced Manufacturing Technology*, vol. 92, no. 5–8, pp. 1777–1824, 2017.
- [4] R. Haque, Y. C. Wong, A. Paradowska, S. Blacket, and Y. Durandet, "SPR characteristics curve and distribution of residual stress in self-piercing riveted joints of steel sheets," *Advances in Materials Science and Engineering*, vol. 2017, Article ID 5824171, 14 pages, 2017.
- [5] L. Kaďeřák, E. Spiřák, R. Kubík, and J. Mucha, "Finite element calculation of clinching with rigid die of three steel sheets," *Strength of Materials*, vol. 49, no. 4, pp. 488–499, 2017.
- [6] G. Meschut, V. Janzen, and T. Olfemann, "Innovative and highly productive joining technologies for multi-material lightweight car body structures," *Journal of Materials Engineering and Performance*, vol. 23, no. 5, pp. 1515–1523, 2014.
- [7] J. Mucha, "The analysis of lock forming mechanism in the clinching joint," *Materials & Design*, vol. 32, no. 10, pp. 4943–4954, 2011.
- [8] J. Mucha and W. Witkowski, "The clinching joints strength analysis in the aspects of changes in the forming technology and load conditions," *Thin-Walled Structures*, vol. 82, pp. 55–66, 2014.
- [9] J. Mucha, L. Kaďeřák, and E. Spiřák, "The experimental analysis of cold pressed joint technology for selected sheet metals used in an automotive industry," *Advanced Materials Research*, vol. 1077, pp. 33–38, 2014.
- [10] J. P. Varis, "The suitability of clinching as a joining method for high-strength structural steel," *Journal of Materials Processing Technology*, vol. 132, no. 1–3, pp. 242–249, 2003.
- [11] K. Mori, Y. Abe, and T. Kato, "Mechanism of superiority of fatigue strength for aluminium alloy sheets joined by mechanical clinching and self-pierce riveting," *Journal of Materials Processing Technology*, vol. 212, no. 9, pp. 1900–1905, 2012.
- [12] B. Xing, X. He, Y. Wang, H. Yang, and C. Deng, "Study of mechanical properties for copper alloy H62 sheets joined by self-piercing riveting and clinching," *Journal of Materials Processing Technology*, vol. 216, pp. 28–36, 2015.
- [13] R. Haque and Y. Durandet, "Strength prediction of self-pierce riveted joint in cross-tension and lap-shear," *Materials & Design*, vol. 108, pp. 666–678, 2016.
- [14] X. Sun and M. A. Khaleel, "Dynamic strength evaluations for self-piercing rivets and resistance spot welds joining similar and dissimilar metals," *International Journal of Impact Engineering*, vol. 34, no. 10, pp. 1668–1682, 2007.
- [15] R. Porcaro, M. Langseth, A. G. Hanssen, H. Zhao, S. Weyer, and H. Hooputra, "Crashworthiness of self-piercing riveted connections," *International Journal of Impact Engineering*, vol. 35, no. 11, pp. 1251–1266, 2008.
- [16] A. Chrysanthou and X. Sun, *Self-piercing Riveting: Properties, Processes and Applications*, Woodhead Publishing, Sawston, UK, 2014.
- [17] Z. Gronostajski and S. Polak, "The application of clinching techniques to join impact energy absorbing thin-walled aluminium sections," *Archives of Metallurgy and Materials*, vol. 54, no. 3, pp. 695–703, 2009.
- [18] G. B. Burger, A. K. Gupta, P. W. Jeffrey, and D. J. Lloyd, "Microstructural control of aluminum sheet used in automotive applications," *Materials Characterization*, vol. 35, no. 1, pp. 23–39, 1995.

- [19] H. Yamada, T. Kami, R. Mori, T. Kudo, and M. Okada, "Strain rate dependence of material strength in AA5xxx series aluminum alloys and evaluation of their constitutive equation," *Metals*, vol. 8, no. 8, pp. 576–591, 2018.
- [20] N. Weiß-Borkowski, J. Lian, T. Marten, T. Tröster, S. Münstermann, and W. Bleck, "Forming limit curves determined in high-speed Nakajima tests and predicted by a strain rate sensitive model," in *AIP Conference Proceedings*, vol. 1896, Dublin, Ireland, October 2017.

Research Article

Microstructural Characterization and Mechanical Properties of Ti-6Al-4V Alloy Subjected to Dynamic Plastic Deformation Achieved by Multipass Hammer Forging with Different Forging Temperatures

Xiurong Fang , Jiang Wu, Xue Ou, and Fuqiang Yang 

School of Mechanical Engineering, Xi'an University of Science and Technology, Xi'an 710054, China

Correspondence should be addressed to Xiurong Fang; fangxr098@163.com

Received 29 March 2019; Revised 1 July 2019; Accepted 8 August 2019; Published 27 August 2019

Guest Editor: Rezwanul Haque

Copyright © 2019 Xiurong Fang et al. This is an open access article distributed under the Creative Commons Attribution License, which permits unrestricted use, distribution, and reproduction in any medium, provided the original work is properly cited.

Dynamic plastic deformation (DPD) achieved by multipass hammer forging is one of the most important metal forming operations to create the excellent materials properties. By using the integrated approaches of optical microscope and scanning electron microscope, the forging temperature effects on the multipass hammer forging process and the forged properties of Ti-6Al-4V alloy were evaluated and the forging samples were controlled with a total height reduction of 50% by multipass strikes from 925°C to 1025°C. The results indicate that the forging temperature has a significant effect on morphology and the volume fraction of primary α phase, and the microstructural homogeneity is enhanced after multipass hammer forging. The alloy slip possibility and strain rates could be improved by multipass strikes, but the marginal efficiency decreases with the increased forging temperature. Besides, a forging process with an initial forging temperature a bit above β transformation and finishing the forging a little below the β transformation is suggested to balance the forging deformation resistance and forged mechanical properties.

1. Introduction

Ti-6Al-4V is one of the most widely used titanium alloys in the aeroengine fields due to its high strength, relatively low density, excellent corrosion resistance, and good creep resistance [1–4]. As a dual-phase alloy consisting of alternate layers of hexagonal close packed (HCP) α and body-centered cubic (BCC) β phases, its mechanical properties are very much dependent on the microstructure morphologies [5, 6]. The Ti-6Al-4V alloy is commonly presented as as-cast ingots with β transformed lamellar structure, and researches have shown that the microstructures of titanium alloys will change to isometric, dual-state, and lamellar structures during the dynamic plastic deformation (DPD) process, which will lead to the improvement of its mechanical properties [7–11]. So many thermo-mechanical processes, such as extrusion [12], forging [13, 14], and hot rolling [15], are carried out to modify its microstructures to the needed morphologies with equiaxed, lamellar, and bimodal.

In the past several years, many efforts have been made to understand the deformation mechanisms and the microstructure evolution of titanium alloys [16–18]. The DPD process at different strain rates were carried out to evaluate the strain rates effects on the microstructural refine and the strength improvement of the alloy [19, 20]. The deformation temperature effects were also investigated to provide the optimized deformation parameters and evaluate the different deformation mechanism of the hot extrusion and rolling technology [12, 15]. Further, the complex relationships between material properties and DPD process parameters have also been studied to improve the strength and plasticity of the titanium alloys [21–26].

Of most DPD studies, the DPD was carried out by press forging at low constant strain rates ($<10^1 \cdot s^{-1}$) in thermal simulator with the static presses powered hydraulically and focused on the deformation temperatures and height reductions effects on the microstructure and mechanical properties of titanium alloys. However, a few researchers

have mentioned that high strain rate combining with certain deformation can refine the grains better and obtain nanostructured metallic materials [19, 27]. However there are seldom studies concerning the high strain rate DPD process achieved by continuous multipass hammer forging in which the high strain rate could be imposed by the hammer blow.

Considering that the DPD achieved by multipass hammer forging with high impact velocities and forging frequency could efficiently reduction the forging time, it is assumed that the multipass hammer forging could be finished during a short term with a high strain rate, which will benefit the microstructure of the titanium alloy. So, this paper focuses on the DPD achieved by multipass hammer forging and studies the temperature effects on the multipass hammer forging process, the microstructure, and the mechanical properties of the forged Ti-6Al-4V alloy. It aims to understand the relationship between the microstructure, mechanical properties, and the multipass hammer forging parameters.

2. Materials and Experimental Procedures

2.1. Materials. Commercially available Ti-6Al-4V alloy bars were used in this study, and the chemical compositions of as-received material are listed in Table 1. The measured β transition temperature of this material is about 990°C. The as-received bars with a diameter of 355 mm and a length of 550 mm were produced by ingot metallurgy, and they were cutting to cuboid samples with the length, width, and height equal to 100 mm, 50 mm, and 80 mm, respectively, by wire electrical discharge machining (WEDM) along the diameter direction of the cylindrical ingot.

2.2. Multipass Hammer Forging Process. Considering that the ram of hammer forging machine can be accelerated by gravity and hydraulic fluid simultaneously and a short forging time and high forging frequency could be controlled, an open-die hammer forging machine [28] was used to carry out the multipass forging process.

The multipass forging process was divided into four steps for every sample, as shown in Figure 1. Firstly, the samples were placed in the preheated molds and then heated to the forging temperature in a special heating furnace with a heating rate of 6°C/min. In order to ensure the uniform temperature distribution inside and outside the samples, the samples were kept in the furnace under forging temperature for a period in the second step, and it was determined to 60 min due to the minimum width of samples. In the third step, the samples were stricken three passes in one direction, with a high-speed camera (5000 sheets/s) used to record the time of each strike. It is reported that the microstructure of alloys can be obviously refined with a more than 20% height reduction, and the crystallization rate will increase dramatically with a deformation over 12% in a single strike [29]. Therefore, a total forging deformation of 50% was controlled by the position limiter in the forging process. Finally, the forged samples were cooled to room temperature by air cooling (AC).

It is known that the titanium will crystallize to α -phase with a HCP structure in low temperature and transforms to

TABLE 1: Chemical composition of Ti-6Al-4V alloy used in this study.

Elements	Al	V	Fe	C	Impurity	Ti
(Wt.%)	6.4	4.1	0.17	0.02	≤0.30	Bal

β -phase with BCC structure in high temperature, as shown in Figure 2, thus the forging of titanium is divided into $\alpha + \beta$ forging and β forging. During the $\alpha + \beta$ forging, the alloy should be heated to a temperature 30°C to 100°C below the β transition temperature. While for β forging, the alloy is first heated above the β transition temperature, and the forging process should be finished before the β to α transformation starts. In order to study the forging temperature effects on the forging process, the microstructural and the mechanical properties of forged samples and three different forging types with five different forging temperatures were selected based on the β transition temperature T_β , as shown in Table 2. The near β forging type in Table 2 is defined to characterize the forging process with a temperature only a little below the β transition temperature due to the low α volume phase fraction in the alloy under this temperature.

2.3. Mechanical Properties and Microstructure Test. Five groups tensile specimens with five specimens in each group were cut from each forged samples, and the tensile tests were performed on an MTS mechanical machine with the tensile speed of 10 mm/min at room temperature, and the tensile strain rate is $6.67 \times 10^{-3} \text{ s}^{-1}$. The averaged mechanical properties of each specimens were calculated after the tensile tests. The dimension of each specimen is shown in Figure 3(a).

Cube specimens with the dimension of $10 \times 10 \times 10 \text{ mm}^3$ were obtained by wire cutting along the forging direction to observe the microstructure. Then, the microstructure of the specimens was observed using optical microscope (OM) after the process of grinding, polishing, and chemical etched in a solution of 13% HNO_3 , 7% HF, and 80% H_2O for 1 min. The fracture morphology of tensile specimens was observed by scanning electron microscope (SEM).

3. Results and Discussion

3.1. Initial Microstructure before Multipass Hammer Forging. Figure 4 shows the initial microstructure of the Ti-6Al-4V bar before forging. The metallographic figures show that the primary β phase as a small seam around the coarsely and lightly colored primary lamellae α phase.

3.2. Microstructural Characterization after Multipass Hammer Forging. The microstructure evolution after the multipass hammer forging process was investigated by detecting the microstructure of the five forged samples, and the microstructures are shown in Figure 5. At the temperature of 925°C, after three-pass hammer forging, the morphology with equiaxed α phase, rod-like α phase, and olivary α phase lying in the lamellar $\alpha + \beta$ matrix could be seen in Figure 5(a), and these α phases have more smaller sizes contrary to the original coarse lamellae α phases. The multipass hammer process efficiently

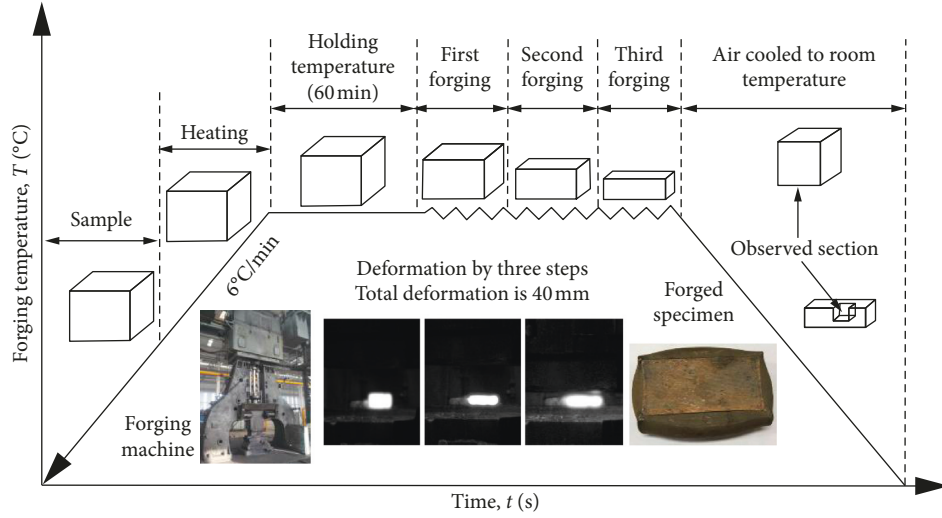


FIGURE 1: Detailed experimental design for description of forging experimental procedure.

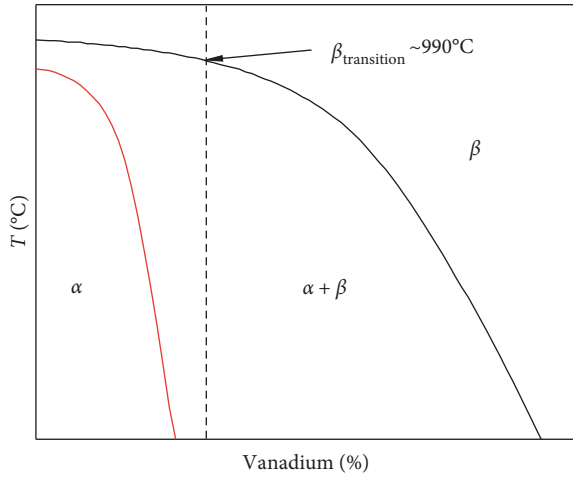

 FIGURE 2: Pseudobinary phase diagram (schematic) of α - β titanium alloy.

TABLE 2: Selected forging temperatures and corresponding alloy phases.

Sample no.	Forging temperature, T (°C)	Alloy phases	Forging types
1 [#]	$T_{\beta} - 65$ 925	$\alpha + \beta$	$\alpha + \beta$ forging
2 [#]	$T_{\beta} - 40$ 950	$\alpha + \beta$	$\alpha + \beta$ forging
3 [#]	$T_{\beta} - 15$ 975	β + insignificant α	Near β forging
4 [#]	$T_{\beta} + 10$ 1000	β	β forging
5 [#]	$T_{\beta} + 35$ 1025	β	β forging

broke down the coarse as-cast lamellar microstructure, and then the broken piece lamellae recrystallize to globular primary α phases. With the temperature increases to 950°C and 975°C, similar globularization of the lamellar microstructure also took place, as shown in Figures 5(b) and 5(c). However, the morphology is slightly different. According to the thermodynamics theory of phase transformation, the total volume fraction of α

phase is mainly associated with the forging temperature. Higher forging temperature will lead to lower volume fraction of α phase. When the forging temperature increases from 925°C to 950°C and 975°C, the volume fraction of the primary α phase decreases due to the $\alpha + \beta \rightarrow \beta$ transformation and more needlelike $\alpha + \beta$ lamellar matrix appear.

When the temperature increases above the β transformation temperature to 1000°C or 1025°C, all the phases change to β phase and the forging corresponding to β forging processes. Once the forged sample is cooled from temperatures above the β transformation temperature, the α phase nucleates at grain boundaries and then grows as lamellae into the prior β phase, and then the fine needlelike $\alpha + \beta$ lamellar phase is formed as shown in Figures 5(d) and 5(e). However, insignificant differences exist between the two figures. The forged sample morphology seems to have the equiaxed α phases scatter into the needlelike $\alpha + \beta$ matrix at 1000°C but all needlelike $\alpha + \beta$ lamellae at 1025°C. The reason for this difference maybe that the forging temperature of 1000°C is just above the β transformation, it decreases below the β transformation temperature, and a near β forging was actually carried out. By comparing Figures 5(c) and 5(d), the similar bimodal microstructures that consist partly of equiaxed primary α in a lamellar $\alpha + \beta$ matrix are found, and the more little equiaxed primary α in Figure 5(d) due to a higher temperature.

3.3. Strain Rate of the Forging Process. In the multipass hammer forging process, the strain rate of each strike was calculated by the sample deformation and deformation time in each strike:

$$\dot{\epsilon} = \frac{\Delta h}{h} \cdot \frac{1}{t}, \quad (1)$$

where $\dot{\epsilon}$ is the forging strain rate, s^{-1} ; h is the initial height of the sample before each strike, mm; Δh is the height reduction samples in the strike, mm; and t is the strike time, s. The measured forging parameters of each strike for the five different samples are listed in Table 3.

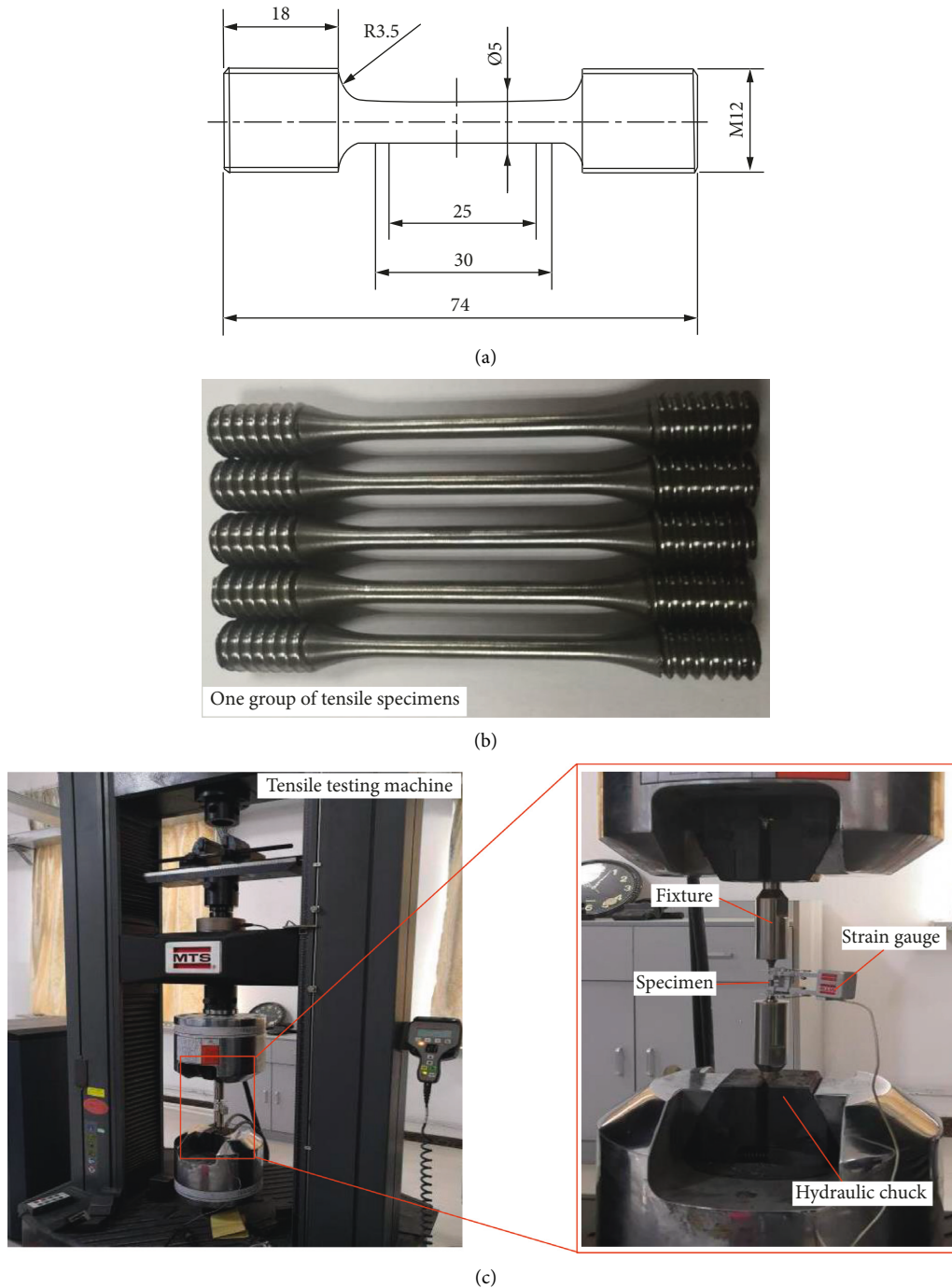


FIGURE 3: Schematic of mechanical properties test. (a) Dimensions of specimen; (b) one group of tensile specimens; (c) MTS tensile testing machine.

By substituting the parameters in Table 3 into equation (1), the strain rate of each strike could be achieved and is shown in Figure 6, which shows the variation of strain rate with temperature and forging processes. It can be seen that the strain rate of first strike increases with the forging temperature, which could be interpreted by the volume fraction increasing of β phase due to the temperature increases. Generally, the plastic deformability is associated with the number of slip systems, which is determined by the

number of slip planes multiplied by the number of slip directions. These planes and directions of highly dense packed atoms are energetically most favorable for plastic deformation. The denser slip planes are packed with atoms, the easier dislocations can glide. Therefore, a slip plane in the HCP lattice with a packing density of 91% should be superior to a slip plane in the BCC lattice with a packing density of only 83%. The α phase of titanium has a HCP lattice while the β phase has a BCC lattice, so the increased β phase

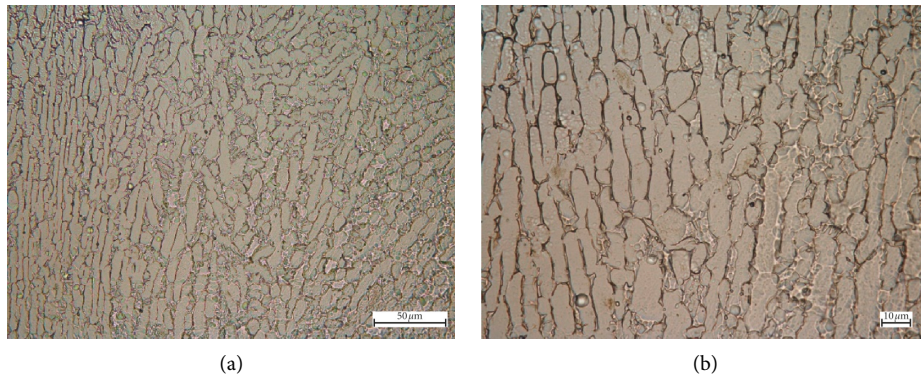


FIGURE 4: Microstructure of as-received Ti-6Al-4V alloy: (a) 50x and (b) 100x.

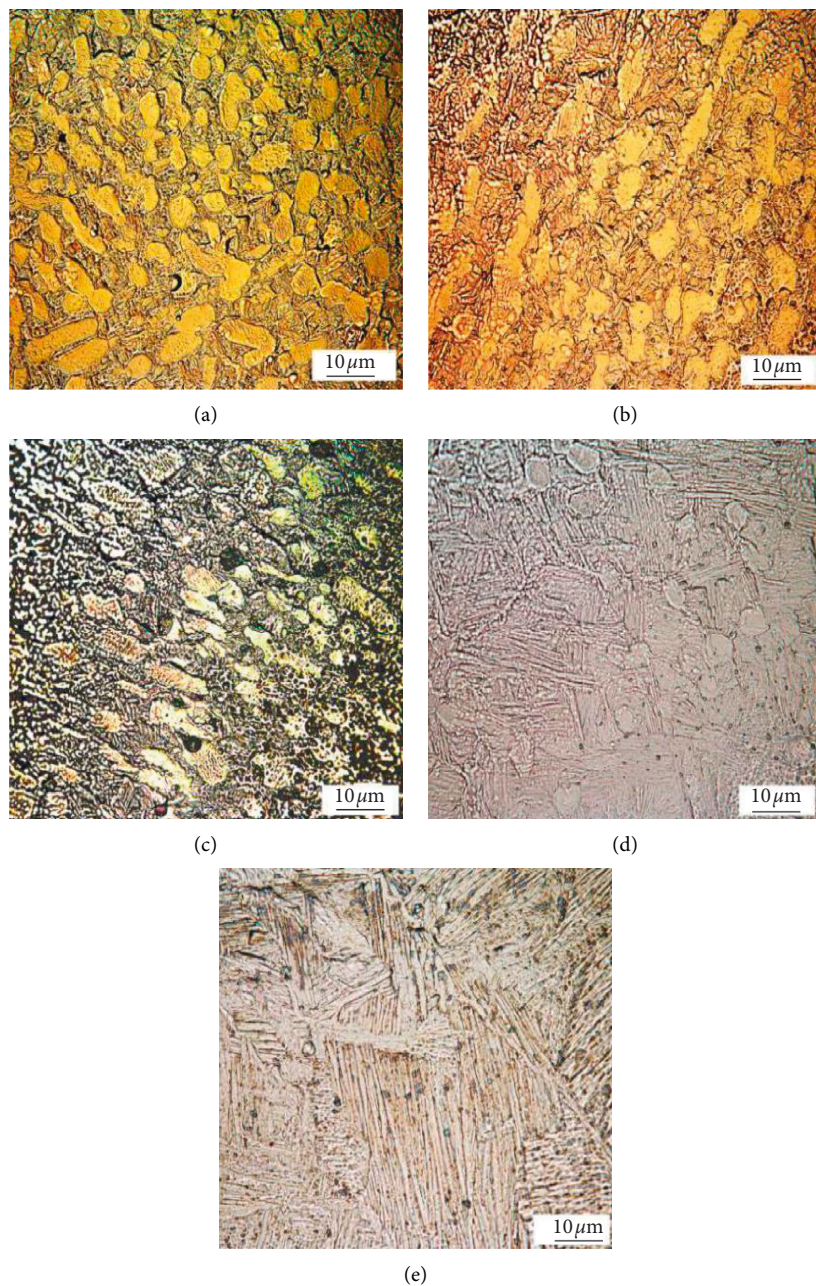


FIGURE 5: Typical metallographic images of samples prepared at different forging temperatures: (a) 925°C; (b) 950°C; (c) 975°C; (d) 1000°C; (e) 1025°C.

TABLE 3: Parameters related to the multipass hammer forging.

Sample no.	Forging temperature, T ($^{\circ}\text{C}$)	First step strike		Second step strike		Third step strike		Total deformation reduction (%)
		Δh (mm)	T (10^{-3} s)	Δh (mm)	t (10^{-3} s)	Δh (mm)	t (10^{-3} s)	
1	925	10	12.3	14	19.3	16	24.0	50
2	950	10	11.6	12	14.9	18	24.1	50
3	975	14	16.0	12	14.6	14	17.8	50
4	1000	18	19.4	12	13.9	10	11.0	50
5	1025	16	16.0	14	15.3	10	12.0	50

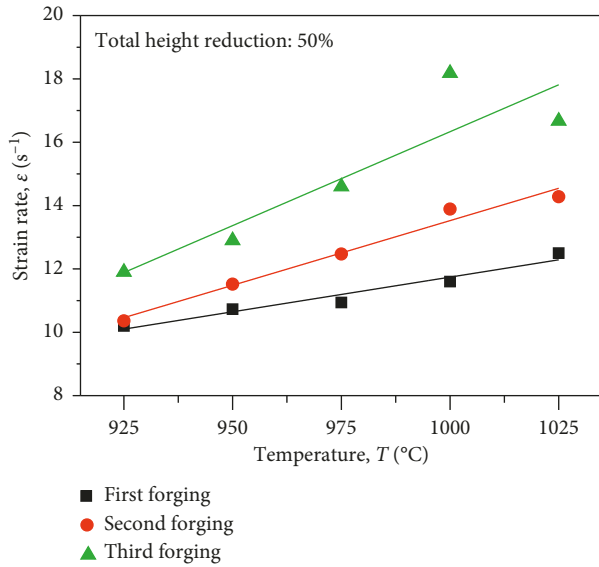


FIGURE 6: Strain rate-temperature curves for multiple forging times.

volume fraction caused by increased temperature increases the slip possibility of the alloy and lead to a larger strain rate. With the increase of temperature, the internal energy of the alloy also increases, and this could decrease the energy needed for atom movement and also lead to the decrease of deformation resistance and the improvement of mobility.

As shown in Figure 6, at temperature of 925°C , the strain rate of the first strike is 10 s^{-1} and increases insignificantly in the second strike, but it increases to about 12 s^{-1} in the third strike. The strain rate increases with the multipass strikes going on seems to occur in all evaluated forging temperature, which means a better mobility and plasticity of the material could be achieved by multipass strike than only one pass strike. Tang et al. [30] examined the microstructure and texture evolution during the multipass forging process, and they found that the volume fractions of α phase are 77.37%, 84.38%, 83.83%, and 78.20%, respectively, from the first pass forging to the fourth pass forging; there are only insignificant changes of α phase due to the small temperature difference between the different passes. Thus, the strain rate improvement is not caused by the increase of β phase. With the going on of the following forging pass, the volume fraction and grain size of primary α phase α_p increase. The size range of α_p changes from $9.88\text{--}37.21\text{ }\mu\text{m}$ after the first pass forging to $4.93\text{--}25.7\text{ }\mu\text{m}$, $5.56\text{--}31.35\text{ }\mu\text{m}$, and $7.78\text{--}40.96\text{ }\mu\text{m}$ after the following three pass forging. Meanwhile, the volume fraction of α_p raises from 30.15% to 36.07%, 39.22%, and 43.70%

during the multipass forging process. Jha et al. [31] claimed that the lamellar morphology of microstructure resists the deformation initially to a greater extent compared to equiaxed morphology and causes higher flow stress compared to equiaxed. On further deformation, the lamellar microstructure kinks, bends, and breaks resulting in higher flow softening than equiaxed morphology. Thus, the increased size and volume fraction of primary α phase may associate with the strain rate increase for multipass hammer forging at evaluated temperature. The increase of strain rates for the second and third strikes with increasing temperature are also demonstrated in Figure 5, and this could also attributed to the volume fraction improvement of β phase and the decrease of active energy needed for atom movement.

To evaluate the forging effects on the strain rate, a strain rate ratio is defined as

$$\chi = \frac{\dot{\epsilon}_{i+1}}{\dot{\epsilon}_i}, \quad (2)$$

where χ is strain rate ratio, which denotes the forging effects on the strain rate; $\dot{\epsilon}_{i+1}$ and $\dot{\epsilon}_i$ ($i = 1, 2$) are strain rates of the $i + 1$ and i pass strike, respectively, at evaluated temperature.

As shown in Figure 7, in the temperature of 925°C to 1000°C , the $\dot{\epsilon}_2/\dot{\epsilon}_1$ increases linearly from about 1.03 to 1.2 with forging temperature, which indicates that the slip possibility of the alloy has been improved by the first strike. The slip possibility of the alloy improved only 3% at 925°C ; the effect is not significant, but a 20% mobility improvement could be achieved at 1000°C . When comparing the strain rates of the third strike and the second strike by $\dot{\epsilon}_3/\dot{\epsilon}_2$, a dramatic improvement of strain rate about 15% was achieved at 925°C after the second strike; the strike effect is much higher than the first strike, the reason maybe that at a relative lower temperature, the microstructure is coarse lamellae, which has a larger broken resistant, so the first strike only breaks the lamellae to coarse segments, and leads to a slow recrystallization and globularization of lamellar structure. But, the second strike efficiently broke the coarse lamellae to small pieces and accelerated the recrystallization and globularization process, which leads to the dramatic improvement of the mobility. The alloy mobility improved by the second strike at 950°C and 975°C is also obvious with 11.3% and 11.7%, even though the second strike is more meaningful for lower temperature, as after the first and second strikes, the strain rate improvement is 3% and 15% at 925°C , while the values are 11.4% and 11.7% at 975°C , and the marginal efficiency of the second strike decreases with the increase of temperature. However, a multipass strike at high temperature still has their meaning of existence as a multipass hammer could refine the

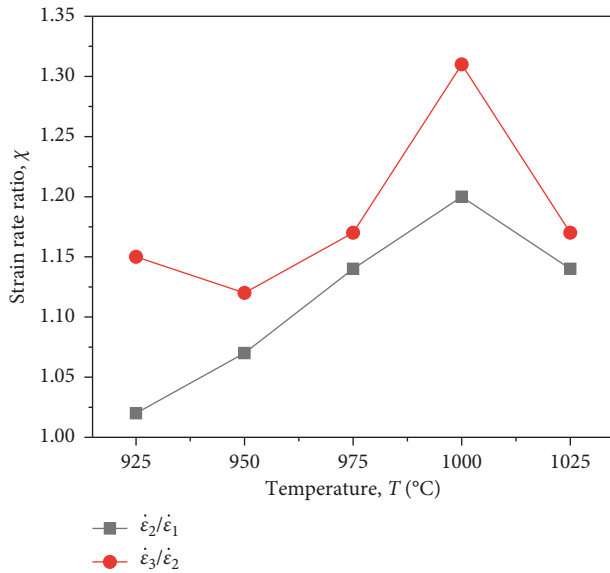


FIGURE 7: Strain rate sensitivity coefficient for forging temperature and forging number.

microstructure and improve the recrystallization and globularization of lamellar structure to α_p , which is a benefit for improving the material properties.

3.4. Effects of Multipass Hammer Forging on Mechanical Properties

3.4.1. Material Properties of Forged Sample at Different Temperatures. The stress-strain curves and the mechanical properties such as yield stress (YS), ultimate tensile strength (UTS), elongation (EL), and reduction of fracture area of the forged samples at different temperatures are shown in Figure 8. As demonstrated in Figure 8(a), with the increase of forging temperature, the fracture strain decreases from 0.217 to 0.137 and the fracture stress increases. At the temperature below β transformation, the YS decreases from 1026 MPa to 1008 MPa with the increase of forging temperature, accompanied with the UTS decrease from 1086 MPa to 1070 MPa. When the forging temperature increases to only a little above the β transformation, both the YS and the UTS have a high value of 1014 MPa and 1086 MPa, respectively, which almost reach the values at temperature of 925°C. If the forging temperature increases continuously, both the YS and UTS decrease dramatically to a low level. The elongations of different specimens have an approximate negative linear relationship with temperature until it reaches the temperature a bit above the β transformation and an insignificant decrease from 16.5% to 13.5%. The elongation will decrease sharply to about 9.5% when the forging temperature further increases. The reduction of fracture area represents only a slight decrease from 46% to 43% when the forging temperature changes from 925°C to 950°C, remains almost constant to the temperature a bit above the β transformation, and then decreases significantly to 11%.

The strength differences of the samples at different temperatures are mainly caused by the microstructures. The

microstructure of titanium alloys is primarily determined by the size and arrangement of the α and β phases, and the two extreme cases of phase arrangements are the lamellar microstructure, which is generated upon cooling from the β phase field, and the equiaxed microstructure, which is a result of a recrystallization process. Numerous investigations have been subjected to how the size of the phases and the arrangement of the phases affect the mechanical properties. With the increase in volume fraction of equiaxed α phase, the strength of the alloy will increase. As the microstructure of forged samples shown in Figure 5 depicts, the primary equiaxed α phase decreases with the increasing forging temperature below the β transformation temperature, which lead to the decrease of YS and UTS. The sample forged at 1025°C has the lowest YS and UTS, and the microstructure of this sample is all needlelike $\alpha + \beta$ lamellae, which will lead to the poor performance of strength. A special difference that should be pointed is that when forging temperature is only a little above the β transformation, the sample also shows good strength performance, which is almost the same with the sample forged at 925°C; this could be attributed to the achieved bimodal microstructure.

Similar to the strength, the ductility of the Ti-6Al-4V alloy also has a positive correlation with equiaxed α phase and a negative correlation with $\alpha + \beta$ lamellar microstructure. With an equiaxed α phase of finer grains, the strain inside and near the grain boundary of the finer grains varies insignificantly and the deformation is more uniform, so the chance of cracking due to stress concentration is much less and a larger amount of deformation could be sustained before fracture [32]. Therefore, the samples 1[#]~4[#], which contain the equiaxed α phase, demonstrate larger elongation and reduction of fracture area than sample 5[#]. The insignificant decrease of ductility may associate to the reduction of equiaxed α phase.

It is summarized according to Figure 8 that the forging temperature has a great influence on the YS and UTS. If the forging is carried out above the β transformation temperature, a lamellar microstructure with low strength will be formed, while forging below the β transformation temperature can achieve high YS and UTS. And, the lower the forging temperature, the higher strength achieved. However, the forging temperature should be in the range of $\alpha + \beta$ two-phase zone and ensures that the crack-free forging is possible at high degrees of deformation. Semiatin et al. [33] reported that the billets should be hot deformed below the β transformation temperature to get a microstructure consisting of fine equiaxed primary α phase and transformed β . Brun et al. [34] also noted that the development of a regulated structure in $\alpha + \beta$ two-phase titanium alloy was significant for the production of titanium alloy semiproducts. Although good strength could be achieved by forging under the β transformation temperature, the mobility of the metal is not good at low temperature. As the flow curves demonstrate in Figure 9 [35], the yield stress at the temperature above β transformation is very low and almost present as a constant, when the temperature drops to below the β transformation temperature, and the deformation resistance increases with the decreased temperature. So, a balance should be concerned to ensure the good mobility during the forging

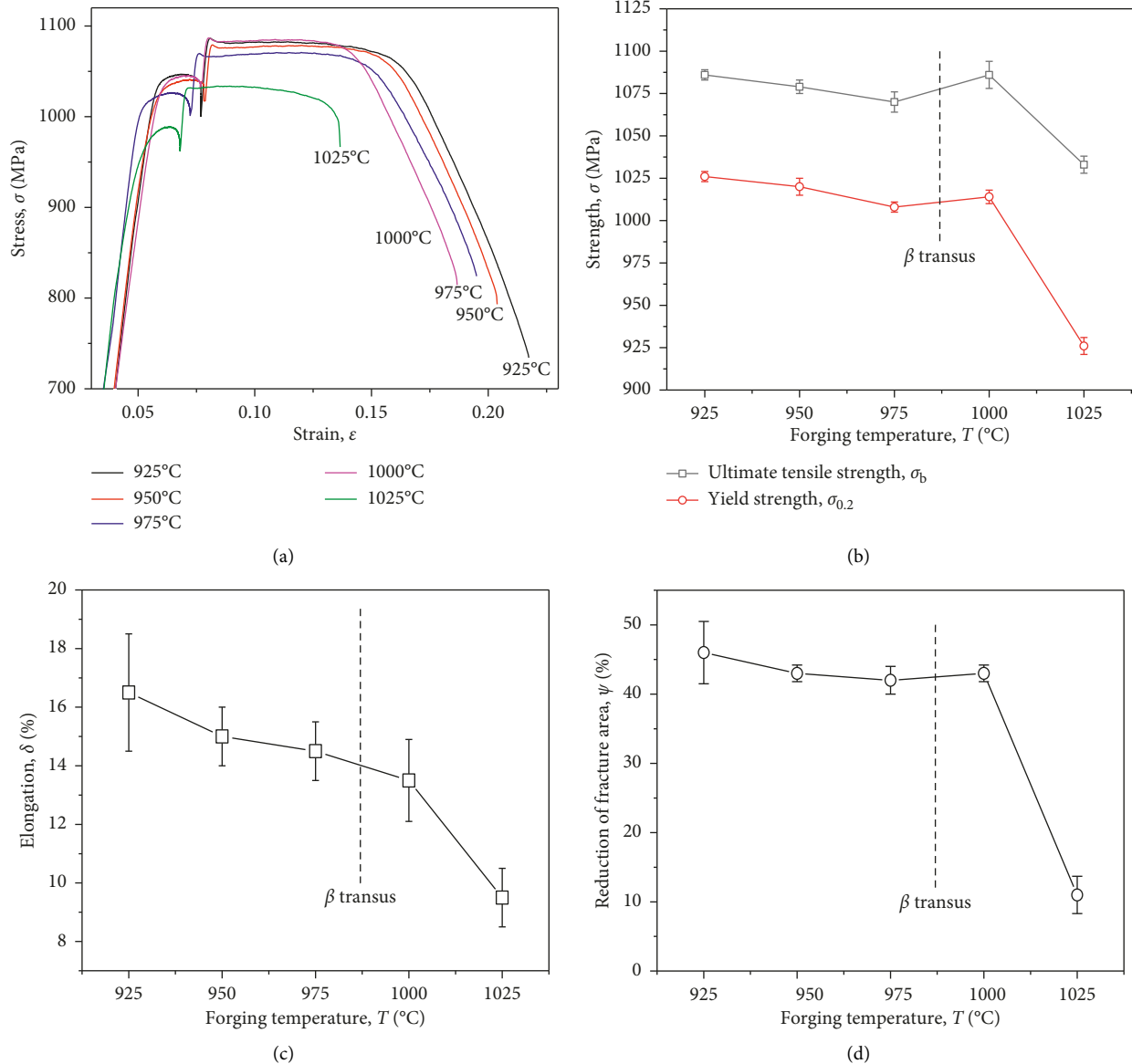


FIGURE 8: The stress-strain curves and the mechanical properties of the samples forged at different temperatures. (a) Stress-strain curves; (b) yield strength and ultimate tensile stress; (c) elongation and (d) reduction of area.

process and good mechanical properties after the forging when designing the forging process.

By considering the five forged samples, it is found that the sample forged at the temperature only a little above the β transformation has the maximum strain rate compared to the sample forged at the temperature below the β transformation. Even the sample 4[#] is forged above the β transformation temperature, its YS and UTS are almost the same with sample 1[#], which is the $\alpha + \beta$ forging, and the reduction of ductility is insignificant. The microstructure of sample 4[#] is bimodal, which is formed under β transformation temperature, thus the sample 4[#] was initially heated to the temperature above β transformation to reduce the deformation resistance; the forging was finished at the temperature a little below the β transformation to achieve a bimodal microstructure, and this process can achieve the balance. So it is suggested that during the multipass hammer forging process, the first step is isothermal forging conducted in

the β phase zone, and the following forging should be finished at the temperature a little below the β transformation.

The mechanical properties of samples with multipass hammer forging are compared in Table 4 with the press forging results reported in the literatures [36, 37]; it can be seen that the YS and UTS are all improved by multipass hammer forging; the elongation and the reduction of fracture area have little differences. Thus, it could be concluded that the mechanical properties of the Ti-6Al-4V alloy obtained by multipass hammer forging is better than that of press forging.

3.4.2. Fracture Morphology Observation. The tensile fracture morphology of different specimens was observed by scanning electron microscope (SEM), and the results are shown in Figure 10. Figure 10(a) is the fracture morphology at temperature of 925°C; an obvious fiber region was found in

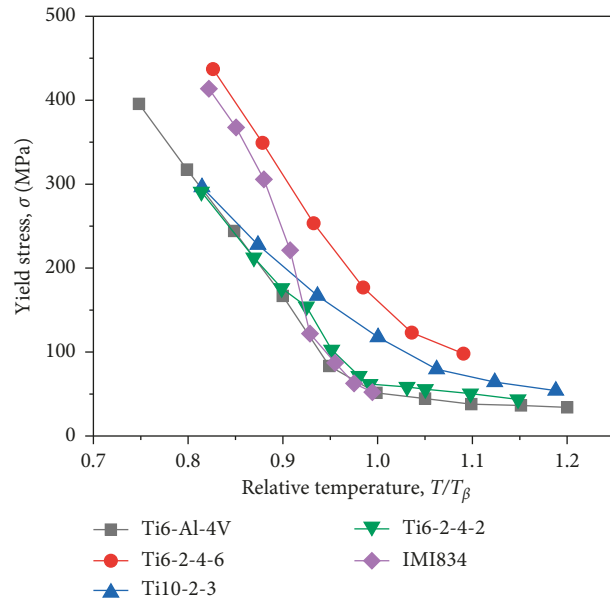


FIGURE 9: Flow curves of titanium alloys [35].

TABLE 4: Comparison of the mechanical properties of different forging processes.

Forging methods	Yield strength, $\sigma_{0.2}$ (MPa)	Ultimate tensile strength, σ_b (MPa)	Elongation, δ (%)	Reduction of fracture area, Ψ (%)
Press forging [36]	925	960	15.5	44
Press forging [37]	1015	940	12.5	39
Hammer forging	1020	1079	15.0	43

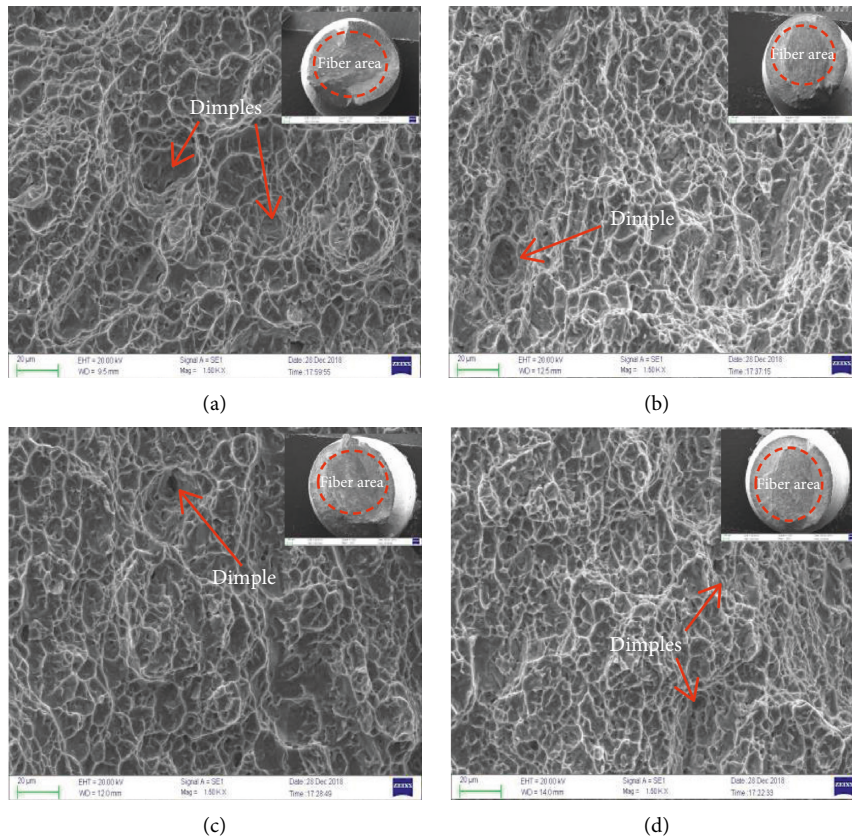
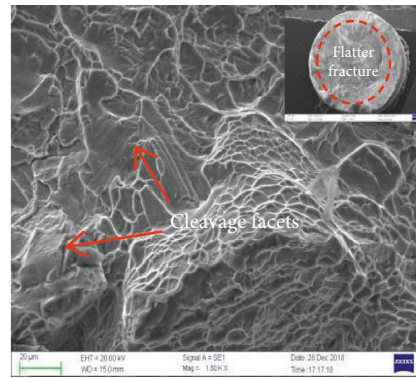


FIGURE 10: Continued.



(e)

FIGURE 10: Fracture morphology at different forging temperatures: (a) 925°C; (b) 950°C; (c) 975°C (d) 1000°C; (e) 1025°C.

fracture surface, accompanied with a large number of spherical dimples with a dimension of $20\ \mu\text{m}$. A typical shear lip region and fibrous region, almost fully covered by deeper dimples with size of $10\ \mu\text{m}$, can be clearly observed in Figure 10(b). Meanwhile, it can be observed that deeper and small number of dimples with size of $5\ \mu\text{m}$ appeared on the fracture surface. From Figure 10(c), it is concluded that the fracture surface is a typical ductile fracture. Figure 10(d) shows the obvious fibrous region, and a large number of shallow depth dimples with $3\ \mu\text{m}$ were observed in fracture surface. Figure 10(e) shows the flatter and cleavage facets, and the intergranular fracture and cleavage fracture features finally lead to the worse plasticity at 1025°C. At 925°C, the spherical dimple size of the fracture surface of the tensile specimen of Ti-6Al-4V alloy is the largest, and there is no cleavage plane; the above analysis shows that the more the number of dimples and the larger the size, the better the plasticity properties of the material.

4. Conclusions

The effects of forging temperature on microstructure and mechanical properties of the multipass hammer forging process of Ti-6Al-4V alloy were investigated based on the integrated approaches of OM and SEM. The strain rate of each strike in the multipass hammer forging process was acquired and discussed. The main results can be summarized as follows:

- (1) The coarse $\alpha + \beta$ lamellar microstructure was globularized and refined to a homogeneous equiaxed primary α phase located in the needlelike $\alpha + \beta$ lamellar phase after the three-pass hammer isothermal forging process.
- (2) The YS and UTS of forged sample decrease with the increased temperature below the β transformation, while the elongation and reduction of fracture area change insignificantly.
- (3) The strain rate in a multipass hammer forging process increases with forging temperature and strikes; the alloy mobility could be improved by multipass strikes, but the marginal efficiency of the

second strike decreases with the increased forging temperature.

- (4) By heating the alloy to an initial temperature a bit above the β transformation, the forging could be carried out with a low deformation resistance; by finishing the forging process below the β transformation temperature slightly, a bimodal microstructure could be achieved. The forged sample exhibits high YS and UTS similar to a lower temperature forging in $\alpha + \beta$ zone and an insignificant loss of ductility. The designed forging process is suggested due to the balance of deformation stress and mechanical properties.

Data Availability

The data used to support the findings of this study are included within the article.

Conflicts of Interest

The authors declare that they have no conflicts of interest.

Acknowledgments

The authors gratefully acknowledge the financial support of this study by the National Natural Science Foundation of China (Grant no. 51775427) and the research fund of the State Key Laboratory for Marine Corrosion and Protection of Luoyang Ship Material Research Institute (LSMRI) under the contract no. 61429010102.

References

- [1] S. Roy and S. Suwas, "Unique texture transition during sub β -transus annealing of warm-rolled Ti-6Al-4V alloy: role of orientation dependent spheroidization," *Scripta Materialia*, vol. 154, pp. 1–7, 2018.
- [2] N. Kherrouba, M. Bouabdallah, R. Badji, D. Carron, and M. Amir, "Beta to alpha transformation kinetics and microstructure of Ti-6Al-4V alloy during continuous cooling," *Materials Chemistry and Physics*, vol. 181, pp. 462–469, 2016.

- [3] Y. X. Liu, W. Chen, Z. Q. Li, B. Tang, X. Q. Han, and G. Yao, "The HCF behavior and life variability of a Ti-6Al-4V alloy with transverse texture," *International Journal of Fatigue*, vol. 97, pp. 79–87, 2017.
- [4] G. G. Yapici, I. Karaman, and Z.-P. Luo, "Mechanical twinning and texture evolution in severely deformed Ti-6Al-4V at high temperatures," *Acta Materialia*, vol. 54, no. 14, pp. 3755–3771, 2006.
- [5] H.-Q. Chen and C.-X. Cao, "Characterization of hot deformation microstructures of alpha-beta titanium alloy with equiaxed structure," *Transactions of Nonferrous Metals Society of China*, vol. 22, no. 3, pp. 503–509, 2012.
- [6] A. Sola, D. Bellucci, and V. Cannillo, "Functionally graded materials for orthopedic applications—an update on design and manufacturing," *Biotechnology Advances*, vol. 34, no. 5, pp. 504–531, 2016.
- [7] H. J. Liu, L. Zhou, and Q. W. Liu, "Microstructural characteristics and mechanical properties of friction stir welded joints of Ti-6Al-4V titanium alloy," *Materials & Design*, vol. 31, no. 3, pp. 1650–1655, 2010.
- [8] B. Surowska, J. Bienias, M. Walczak, K. Sangwal, and A. Stoch, "Microstructure and mechanical properties of ceramic coatings on Ti and Ti-based alloy," *Applied Surface Science*, vol. 238, no. 1–4, pp. 288–294, 2004.
- [9] C. S. Meredith and A. S. Khan, "The microstructural evolution and thermo-mechanical behavior of UFG Ti processed via equal channel angular pressing," *Journal of Materials Processing Technology*, vol. 219, pp. 257–270, 2015.
- [10] F. Jie, D. Hua, H. Yi, W. Zhang, and T. G. Langdon, "Influence of phase volume fraction on the grain refining of a Ti-6Al-4V alloy by high-pressure torsion," *Journal of Materials Research and Technology*, vol. 4, no. 1, pp. 2–7, 2015.
- [11] J. Jayakumar, B. K. Raghunath, and T. H. Rao, "Enhancing microstructure and mechanical properties of AZ31-MWCNT nanocomposites through mechanical alloying," *Advances in Materials Science and Engineering*, vol. 2013, Article ID 539027, 6 pages, 2013.
- [12] T. Seshacharyulu, S. C. Medeiros, W. G. Frazier, and Y. V. R. K. Prasad, "Microstructural mechanisms during hot working of commercial grade Ti-6Al-4V with lamellar starting structure," *Materials Science and Engineering A*, vol. 325, no. 1–2, pp. 112–125, 2002.
- [13] I. Weiss, F. H. Froes, D. Eylon, and G. E. Welsch, "Modification of alpha morphology in Ti-6Al-4V by thermo-mechanical processing," *Metallurgical Transactions A*, vol. 17, no. 11, pp. 1935–1947, 1986.
- [14] S. L. Semiatin, R. L. Goetz, V. Seetharaman, E. B. Shell, and A. K. Ghosh, "Cavitation and failure during hot forging of Ti-6Al-4V," *Metallurgical and Materials Transactions A*, vol. 30, no. 5, pp. 1411–1424, 1999.
- [15] J. L. W. Warwick, N. G. Jones, I. Bantounas, M. Preuss, and D. Dye, "In situ observation of texture and microstructure evolution during rolling and globularization of Ti-6Al-4V," *Acta Materialia*, vol. 61, no. 5, pp. 1603–1615, 2013.
- [16] D. A. S. Macdougall and J. Harding, "A constitutive relation and failure criterion for Ti-6Al-4V alloy at impact rates of strain," *Journal of the Mechanics and Physics of Solids*, vol. 47, no. 5, pp. 1157–1185, 1999.
- [17] S. M. Abbasi and A. Momeni, "Effect of hot working and post-deformation heat treatment on microstructure and tensile properties of Ti-6Al-4V alloy," *Transactions of Nonferrous Metals Society of China*, vol. 21, no. 8, pp. 1728–1734, 2011.
- [18] S. Roy and S. Suwas, "The influence of temperature and strain rate on the deformation response and microstructural evolution during hot compression of a titanium alloy Ti-6Al-4V-0.1B," *Journal of Alloys and Compounds*, vol. 548, no. 4, pp. 110–125, 2013.
- [19] T. Naizhen and K. Lu, "Preparation technology of plastic deformation of nanostructured metal materials," *Journal of Metals*, vol. 50, no. 2, pp. 141–147, 2014.
- [20] K. P. Rao and Y. V. R. K. Prasad, "Advanced techniques to evaluate hot workability of materials," *Comprehensive Materials Processing*, vol. 3, pp. 397–426, 2014.
- [21] J. Luo, S. F. Liu, and M. Q. Li, "Quantitative analysis of microstructure and deformation mechanisms during isothermal compression of Ti-5Al-5Mo-5V-1Cr-1Fe alloy," *Materials Characterization*, vol. 108, pp. 115–123, 2015.
- [22] J. Luo, M. Li, W. Yu, and H. Li, "The variation of strain rate sensitivity exponent and strain hardening exponent in isothermal compression of Ti-6Al-4V alloy," *Materials & Design*, vol. 31, no. 2, pp. 741–748, 2010.
- [23] K. Wang and M.-Q. Li, "Characterization of discontinuous yielding phenomenon in isothermal compression of TC8 titanium alloy," *Transactions of Nonferrous Metals Society of China*, vol. 26, no. 6, pp. 1583–1588, 2016.
- [24] T. Seshacharyulu, S. C. Medeiros, W. G. Frazier, and Y. V. R. K. Prasad, "Hot working of commercial Ti-6Al-4V with an equiaxed α - β microstructure: materials modeling considerations," *Materials Science and Engineering: A*, vol. 284, no. 1–2, pp. 184–194, 2000.
- [25] B. Zhao, Y. Zhao, Z. Hou et al., "Design and optimization of the processing parameters of Ti-5Al-3V-3Zr-0.7Cr titanium alloy as a candidate material for pressure hull of fusion reactor," *Fusion Engineering and Design*, vol. 137, pp. 405–413, 2018.
- [26] J. Luo and M. Q. Li, "Strain rate sensitivity and strain hardening exponent during the isothermal compression of Ti60 alloy," *Materials Science and Engineering: A*, vol. 538, no. 10, pp. 156–163, 2012.
- [27] W. Sun, Y. Zhu, R. Marceau et al., "Precipitation strengthening of aluminum alloys by room-temperature cyclic plasticity," *Science*, vol. 363, no. 6430, pp. 972–975, 2019.
- [28] F. Xiu-Rong, Y. Dan-Feng, and D. Jian-Hu, "The research of forging hammer with full hydraulic technique," *Chinese Hydraulics and Pneumatics*, vol. 34, no. 4, pp. 24–26, 2010.
- [29] China Forging Association, *Special Alloys and Their Forging*, National Defense Industry Press, Beijing, China, 2009.
- [30] B. Tang, L. Xiang, Z. Yan, H. Kou, and J. Li, "Effect of strain distribution on the evolution of α phase and texture for dual-phase titanium alloy during multi-pass forging process," *Materials Chemistry and Physics*, vol. 228, pp. 318–324, 2019.
- [31] J. S. Jha, P. T. Suraj, R. Singh, A. Tewari, and K. M. Sushil, "Flow stress constitutive relationship between lamellar and equiaxed microstructure during hot deformation of Ti-6Al-4V," *Journal of Materials Processing Technology*, vol. 270, pp. 216–227, 2019.
- [32] J. Toribio, J. C. Matos, and B. González, "Micro-and macro-approach to the fatigue crack growth in progressively drawn pearlitic steels at different R-ratios," *International Journal of Fatigue*, vol. 31, no. 11–12, pp. 2014–2021, 2009.
- [33] S. L. Semiatin, V. Seetharaman, and I. Weiss, "The thermo-mechanical processing of alpha/beta titanium alloys," *JOM*, vol. 49, no. 6, pp. 33–39, 1997.
- [34] M. Brun, N. Anoshkin, and G. Shakhanova, "Physical processes and regimes of thermomechanical processing controlling development of regulated structure in the α + β titanium alloys," *Materials Science and Engineering: A*, vol. 243, no. 1–2, pp. 77–81, 1998.

- [35] C. Leyens and M. Peters, "Titanium and titanium alloys," *China Surface Engineering*, vol. 23, no. 1, pp. 1–513, 2003.
- [36] W. Yu, M. Li, and J. Luo, "Effect of processing parameters on microstructure and mechanical properties in high temperature deformation of Ti-6Al-4V alloy," *Rare Metal Materials and Engineering*, vol. 38, no. 1, pp. 19–24, 2009.
- [37] M. Li, L. Hong, and J. Luo, *Titanium Alloy Precision Forging*, Vol. 9, Science Press, Beijing, China, 2016.